The Role of Precipitates on Fiber/Matrix Interfaces in Metal Matrix Composites

by

Jeremy R. Gregory

B.S., Montana State University - Bozeman (1998)

Submitted to the Department of Mechanical Engineering
in partial fulfillment of the requirements for the degree of

Master of Science in Mechanical Engineering

at the

MASSACHUSETTS INSTITUTE OF TECHNOLOGY

September 2000

Author .....
Department of Mechanical Engineering
August 8, 2000

Certified by ....
Ali S. Argon
Quentin Berg Professor of Mechanical Engineering
Thesis Supervisor

Accepted by .....
Ain A. Sonin
Chairman, Department Committee on Graduate Students

The Role of Precipitates on Fiber/Matrix Interfaces in Metal Matrix Composites

by

Jeremy R. Gregory

Submitted to the Department of Mechanical Engineering
on August 8, 2000, in partial fulfillment of the
requirements for the degree of
Master of Science in Mechanical Engineering

Abstract

In order to truly understand the mechanisms of deformation in metal matrix composites (MMC), one must examine the fracture process occurring at the interface between the fiber and the matrix. Work by other investigators (Argon et al., 1998) has shown that precipitates that form on the surface of the fiber during the casting process play an important role in determining the strength and behavior of the interface. This thesis studies the effect these precipitates have on the interfaces in two different alumina reinforced aluminum composite systems. Argon's tension/shear: traction/separation response model of interfaces has been applied to the deformation process of the first composite, a continuously reinforced MMC. Experiments attempting to emulate mathematical simulations of the precipitate/fiber debonding process were conducted using specimens that consisted of simulated "precipitates" (of a larger size than what is found on actual fibers to simplify manufacturing) on an alumina disk (representing the fiber) and sandwiched in between aluminum cylinders (representing the matrix). Fabrication of the specimens proved to be quite difficult, but two of the tension tests showed promising results. Nonhomogeneous separation of the interface and the surrounding Al produced results which were not effective quantitative comparisons to the simulations, but supported the general characteristics predicted by the model, particularly the load-displacement behavior and the deformation of the Al around the precipitates. Testing of the second composite system, an Al reinforced with a discontinuous Al_2O_3 preform (volume fraction 20%), described the behavior of the composite based on various heat treatments meant to coarsen the precipitates. The tests showed that overaging at 350 °C decreased the strength, fracture toughness, and hardness of the material while increasing it's strain to fracture. As expected, the infiltrated preform had a higher strength and modulus than its associated unreinforced alloy, but this came at a cost of a significant increase in embrittlement. The causes of the changes in material behavior were traced to the development of precipitate size and distribution along with the interaction of cavities that develop around precipitates during the fracture process which have an adverse effect on its strength. Ultimately, the infiltrated fiber preform may have simpler manufacturing and cost

advantages, but the random orientation of the fibers prevent it from obtaining the potential realized in aligned fiber composites at a cost of significantly reduced fracture properties (at ambient conditions).

Thesis Supervisor: Ali S. Argon
Title: Quentin Berg Professor of Mechanical Engineering

Acknowledgments

Professor Argon's guidance and wisdom challenged me to obtain my full potential. It was an honor and a privilege to work with such a wonderful advisor and I am grateful to have had the opportunity. I would not have been able to complete my experiments without the work and support of various MIT research groups, Paul Tierney of the MIT MTL, Peter Morley of the MIT Central Machine Shop, Fred Cote of the Edgerton Student Machine Shop, Bob Murphy of Lincoln Laboratory, Dr. Max Seleznev and Dr. James Cornie of Metal Matrix Cast Composites, Inc., Prof. Vijay Gupta of UCLA, Prof. Lallit Anand of MIT, Peter Madden of the MIT Newman Lab, and the United States Air Force Office of Scientific Research who funded the project. The professors, staff, and students in the Mechanics and Materials group provided me with invaluable advice and direction. Finally, my wife, family, and close friends provided me with support, love, and friendship that allowed me to achieve my goals.

Contents

List of Figures

List of Tables

Chapter 1

Introduction

Fiber reinforced metal matrix composites have shown remarkable potential for improving the mechanical properties of unreinforced metals at intermediate to high temperatures of the matrix. The fibers contribute strength, stiffness, and creep resistance while the metal matrix provides ductility and toughness. However, the interface between the fiber and the matrix in a metal matrix composite (MMC) plays a key role in governing the mechanical behavior of the material. A strong interface will lead to a composite with high transverse strength, moderate longitudinal strength, and reduced longitudinal fracture toughness and fatigue. Conversely, a weak interface will lead to a composite with high longitudinal strength, improved longitudinal fracture toughness and fatigue strength, and diminished transverse strength. In essence, when a fiber fractures in the composite, the matrix surrounding the fiber begins to undergo concentrated plastic flow locally near the fracture. If the interface debonds sufficiently, matrix plastic flow will be dispersed over the debond length, and the local unconstrained necking of the matrix ligament will contribute substantially to the work of fracture of the composite. A tough interface will prevent the plastic dissipation of the local stresses and will thus limit the composite longitudinal toughening effect. Specific material requirements can be obtained by optimizing the state of the fiber/matrix interface.

Many investigators have experimentally studied the interfacial properties of MMC's (i.e. [2], [3]) using a variety of testing methods. Although there are many means avail-

able to quantify the strength of the interface, such as flat plate and embedded single fiber tests (described in [4]), fiber pull-out and/or push-out experiments are the most common methods of testing. While these testing processes may be effective at describing the general behavior of the interface, they fail to examine the micromechanical process of fracture that determines the properties of the interface.

Seleznev et al. have studied the effect that equilibrium precipitates at the fiber/matrix interface have on the mechanical properties of an alumina reinforced aluminum MMC[5]. They concluded that the size and distribution of the precipitates at the fiber/matrix interface governed the process of composite fracture. More importantly, the investigators showed that the mechanical behavior of the composite could be controlled through heat treatments that effectively determine the size and distribution of the precipitates. This type of attention to the precipitates and their effect on the fiber/matrix interface has rarely been given much consideration by other researchers examining MMC's. Seleznev et al. illustrated how manipulation of the micromechanical modes of fracture can produce a change in the overall composite properties.

Using the work of Seleznev as an experimental foundation, Argon developed a tension/shear: traction/separation response model of interfaces in a fiber/matrix composite[1]. The micromechanical model of interface fracture has its basis in similar work done by several investigators ([6], [7], [8]), but more specifically examines the void nucleation at precipitate particles at the fiber/matrix interface and the associated growth of voids by plastic flow. Numerical simulations of Argon's model by Shih and Liu[1] described the nucleation process of the voids created by the precipitates in fracture caused by imposed tension and shear across the interface.

The first component of this thesis will focus on experimental verification of Argon's model and the associated simulations. Due to the extremely small size of the precipitates ($\approx 10^{-7}$ to 10^{-6} m), experimental investigation on the actual scale of the precipitates is quite difficult as it requires unattainable testing machine stiffness to conduct a stable experiment. Hence, a testing procedure was developed to simulate the actual debonding process of the matrix from the fiber, but on a much larger scale (precipitate size of 1 mm) to bring the separation displacements into a range that can

be furnished by a usual stiff testing machine. The specimens used in the test were subjected to applied tension, analogous to the tension response of the precipitates during debonding in the prototype sample. The results of the test are compared with the results of Shih and Liu's simulations.

MMC's reinforced with continuous fibers have several behavioral advantages over unreinforced alloys. However, the cost to manufacture the composite may outweigh any mechanical benefits. An alternative to this class of materials is a MMC manufactured from a discontinuous fiber preform. The preform consists of randomly oriented fiber segments in a block configuration that is infiltrated with the molten matrix material. The ultimate goal of the material is to provide quasi-isotropic reinforcement of an alloy using a manufacturing procedure that is less expensive and simpler than procedures used for MMC's with continuous fiber reinforcement. Although the preform based composite cannot meet the same strength and stiffness levels of the continuously reinforced MMC, the precipitates that develop on the discontinuous fiber segments during the infiltration process could create similar advantages to those observed in the continuous fiber composite. Many studies have examined the effect that particulate reinforcement can have on the mechanical behavior of a material (i.e. [9], [10]). Indeed, particulate reinforced materials are increasingly being used in automotive, electronic, and aerospace applications for their higher strength and stiffness at lower weight when compared to traditional alloys. Precipitates develop on the interface between the particulate material and the matrix in these materials, and the same is true of the preform based composite. Essentially, the particles or short fibers act as carriers of the precipitates. The discontinuously reinforced preform composite has the potential of being a compromise between the continuously reinforced and particulate reinforced composites. It could provide a stiffer and stronger reinforcement than the particulate material while possessing the lower manufacturing cost than the continuous fiber composite. The second section of this thesis will examine whether or not the preform based composite meets these expectations. This proposition is explored by using a MMC consisting of an Al-5%Cu alloy reinforced with an Al_2O_3 fiber preform (volume fraction 20%). Hardness, tension, fracture, and volumetric strain tests char-

acterize the mechanical behavior of the composite in comparison to the unreinforced Al alloy. Various heat treatments of the material show the effect that the size and distribution of the precipitates have on the mechanical behavior of the composite.

Chapter 2

Interface Separation Experiments

2.1 Mechanisms of Interface Fracture in Metal Matrix Composites

The fundamental elements of fracture in metal matrix composites revolve around the condition of the interface between the fiber and the matrix. Figure 2-1 depicts the components of the axial fracture process in a typical continuously aligned alumina fiber reinforced aluminum alloy. Prior to fracture when the composite is loaded in tension parallel to the fibers, the strain is uniform across the fibers and matrix. As the stress increases individual fibers begin to fracture, causing accentuated local plastic flow in the matrix. This local stress translates into a specific local concentration of axial stress in the surrounding fibers [11], which in turn produces "mode A" type planar terraces of fiber fractures. Once the fibers fracture, the ductile matrix in between broken fibers begins to undergo local necking due to the increased stress no longer carried by the fractured fibers. The necking generates deformation induced tractions along the fiber/matrix interfaces and this promotes debonding over a characteristic length L_D. The final debonding length is governed by the peak plastic resistance of the traction separation response of the interface before the eventual rupture of the matrix. It is this process of the matrix debonding from the fiber and ultimately rupturing that is described by the tension:shear/ traction:separation law and highly

dependent on the condition of the interface. Figure 2-1(a) depicts how "mode B" simple shear fractures act to bridge different levels of fiber fracture terraces, while (b) and (c) show the transverse separation of the matrix from the fiber and the role the interface precipitates play in this process. For the particular composite being considered, the interface debonding and fracture is initiated by the separation of the Al_2Cu precipitates that develop on the surface of the fiber during the casting process. Thus, the peak stress of the traction/separation law will be governed by the interface strength between the Al_2Cu precipitates and the fibers and their associated area fraction coverage and mean particle spacing. Once the precipitate separation occurs, the plastic resistance and strain hardening capabilities of the matrix will determine the remaining debonding behavior.

The overall specific work of fracture is a combination of the mode A matrix ligament ruptures and mode B bridging of fractures by simple shear. However, fracture in strong composites is typically characterized by a greater fraction of mode A type fractures than mode B[1]. Hence, mode A fractures are the primary subject of this examination. The mode A specific fracture work U_A can be expressed in a first order, elementary expression

$$U_A = \frac{1}{\sqrt{3}}(1 - v_f)\sigma_0 L_D \tag{2.1}$$

where v_f is the volume fraction of fibers, σ_0 the matrix tensile plastic resistance in a non-hardening model, and L_D is the debonding length[12]. Indeed, tough interfaces will have a low debonding length and hence a low specific fracture work, which translates into low energy absorption in the axial fracture of the composite. Conversely, an interface with excessive debonding will have a detrimental effect on the transverse strength of the composite. It is the size and area fraction of the precipitates on the fiber/matrix interface that determines the debonding length and the associated specific work of fracture. The control that the precipitates have on the separation toughness of the interface and the development of the fiber/matrix debonding during fracture (that behaves in accordance with the separation toughness) is the subject of the tension/shear: traction/separation micromechanical model.

Experimental investigations of a composite consisting of sol-gel derived polycrys-

talline Al_2O_3 (Nextel 610) fibers and an Al casting alloy (5.15% Cu, .12% Fe, .34% Mn) matrix verify the aforementioned mechanisms of fiber/matrix separation[1]. Earlier studies by Seleznev [5] showed that the size and area fraction of the Al_2Cu precipitates could be controlled through a specific overaging treatment. The particular coarsening kinetics of this system yielded a constant precipitate area fraction coverage on the fiber/matrix interfaces of approximately 0.2. The effect that the coarsening kinetics have on the longitudinal and transverse strengths of the composite (uniaxially aligned fibers with a volume fraction of $v_f = 0.5$) is depicted in Figure 2-2. With increased aging at 350 °C, the transverse strength remains essentially constant around the level of 40 MPa up to an aging time of thirty hours while the longitudinal (axial) strength increases monotonically to a maximum value of 975 MPa after ten hours of aging. After peak aging, the longitudinal strength plateaus to a level of approximately 750 MPa while the matrix overages. The transverse strength rises sharply to 338 MPa at 100 hours aging and remains at this level for longer aging times.

The behavior of the composite in these fracture tests can be explained by the coarsening of the precipitates during the aging process. When the composite has been aged for ten hours at 350 °C the matrix exhibits its peak plastic resistance due to precipitate coarsening in the matrix while the interface has a relatively low toughness caused by the small size of the precipitates. In between 30 and 100 hours aging the coarsening of the precipitates drastically improves toughness of the interface and hence the transverse strength of the composite. However, this effect also decreases the debond length which decreases the axial strength of the composite. Aging beyond 100 hours appears to have no change on the composite behavior.

Microscopy of the composite fracture surfaces show the key elements of separation in the fiber and the matrix. Figure 2-3(a) depicts the dimpling of the matrix that occurs during the fracture process and the adherence of the precipitates inside the cavities. The work of adhesion between the Al_2Cu precipitates and the Al_2O_3 fibers is lower than that between the precipitates and the Al matrix, causing the precipitates to preferentially debond from the fibers and remain adhered to the matrix while

the matrix is still adhered to the fibers. Dimpling ruptures of the matrix follow the separation of the precipitates from the matrix. The dimpling behavior is characterized by a mixed mode of normal and shear separation of the matrix from the fiber, as shown in the inset of Figure 2-1(a). Figure 2-3(b) depicts the fully developed rupture of the remaining ligament and the initial planar fracture of the fiber. This debonding behavior must be the result of a deformation induced mix of modes I and II type separations, with the exception being transverse composite fracture which is a direct mode I type fracture, as shown in Figure 2-1(b).

2.2 Tension/Shear: Traction/Separation Model of Fiber/Matrix Interfaces

The fundamental process that is a major contributing factor to the fracture of this Al_2O_3 fiber/Al alloy matrix composite is the ductile cavity growth of the matrix at the locations of the debonded precipitates on the fiber. This process eventually leads to the ductile rupture of the matrix ligaments that are formed, which indicates the composite has fractured. The initial cavity growth is caused by a deformation induced changing mix of tension and shear that produces a mixed mode traction along the interface of the fiber and matrix and leads to the separation of the precipitate from the fiber. Argon's tension/shear: traction/separation model has its foundation in work done by other investigators ([6], [7], [8]), but specifically describes the complexity of the precipitate separation and void nucleation and growth process in response to various imposed tension and shear situations.

The unit cell problem to be solved in the mode A planar separation is depicted in Figure 2-4. The system is treated as being two-dimensional plane strain with a fiber volume fraction of 0.5 and a precipitate area fraction of 0.2 (for this geometry the area fraction is $2R/D$). Although the precipitates form into many different shapes, they are approximated as hemi-spherical to simplify the computations of the cavity growth. The boundary value problem to be considered starts with an assumed initially

cracked Al_2O_3 fiber that is only responding elastically. In contrast, the Al alloy matrix separating from the fiber behaves according to an elastic-plastic-power-law hardening constitutive law. Under uniaxial tension, this constitutive law for the matrix is

$$\frac{\varepsilon^e}{\varepsilon_0} = \frac{\sigma}{\sigma_0} \qquad \frac{\varepsilon^p}{\varepsilon_0} = \left(\frac{\sigma}{\sigma_0}\right)^{\frac{1}{N}} - 1 \qquad (\sigma \geq \sigma_0), \tag{2.2}$$

where σ_0 is the yield strength, $\varepsilon_0 = \sigma_0/E$, $1/N$ is the reciprocal of the strain hardening exponent, and E is the Young's modulus (70 GPa for Al). The plasticity is taken to follow the J_2 flow rule.

A combined proportional displacement loading condition is prescribed at $y = L$, sufficiently far from the precipitates to ensure that the deformation is essentially uniform at this location. The loading is applied through a combination of normal and tangential displacements, δ_n and δ_t respectively, in a fixed ratio δ_t/δ_n. Each loading ratio is characterized by a total displacement δ at a specific phase angle $\varphi = \tan^{-1}(\delta_t/\delta_n)$.

Boundary conditions along the matrix/fiber interface prevent the matrix material in between the precipitates from debonding because of the strong adhesion between the Al alloy and the Al_2O_3 fiber. The prescribed conditions are

$$\begin{aligned} u_1 = u_2 = 0 \text{ at } y = 0 \text{ along } -D/2 \leq x \leq -R \\ \text{and at } y = 0 \text{ along } R \leq x \leq D/2 \end{aligned} \tag{2.3}$$

and

$$u_1 = \delta \sin\varphi, \qquad u_2 = \delta \cos\varphi \text{ at } y = L, \tag{2.4}$$

where δ is the total displacement vector imposed at $y = L$ as depicted in Figure 2-4 with normal and tangential components given by Equation 2.4. Since the precipitates are assumed to be evenly spaced along the fiber and they all have identical fields, it is only necessary to analyze the typical region *abcd*.

When a displacement is imposed, the displacements along the precipitate/matrix interface efg are zero until the normal average stress at the interface eg reaches a critical value T_{ip}, the tensile bond strength between the precipitate and the fiber. Once this condition is met, the tractions along the interface efg are considered zero,

simulating a precipitate separation from the fiber. In reality, the precipitate remains bonded to the matrix after separating from the fiber, but the fact that this assumption is reversed has little effect on the computation because the initial nucleation of the cavity is only a small portion of the entire debonding process. The cavity continues to grow plastically in the matrix after the precipitate debonds until the matrix ligaments in between adjacent cavities neck and rupture. The ligament is defined to have separated when the local ligament plastic strain reaches a terminal strain to fracture value ε_f^p. Even though the ligaments can only separate by rupture, the terminal strain to fracture defines an exact point when the ligament has fractured.

2.3 Simulation Results

The implementation of the tension/shear: traction/separation finite element model used the following matrix properties: Young's modulus $E = 70$ GPa, yield strength $\sigma_0 = 5 \times 10^{-3}E = 350$ MPa, Poisson's ratio $\nu = 0.3$, strain hardening exponent $N = 0.05$, and terminal strain to fracture $\varepsilon_f^p = 1.86$. Furthermore, a tensile bond strength between the fiber and the precipitate $T_{ip} = 1.42 \times 10^{-2}E = 1$ GPa and a precipitate diameter $D = 5 \times 10^{-6}$ m were also used in the computations. These values represent realistic material properties for this composite system. Detailed descriptions of the finite element simulations can be found in [13].

Phase angles φ of 0°, 30°, 60°, and 85° were chosen as imposed displacement conditions to show the behavior of the interface over a range of conditions from pure tension to nearly simple shear (pure simple shear is computationally demanding). Figures 2-5(a,b) show the numerical results for the debonding simulation when $\varphi = 0°$, or pure tension. The letters on the curve in Figure 2-5(a) refer to various critical stages during the debonding process. "A" locates the area where the precipitate debonds from the fiber, "B" refers to the point where complete cavity nucleation has occurred, and "C" points to the period where matrix shearing failure takes place. The circled numbers on the plot refer to the locations of the deformed configurations in Figure 2-5(b). The curves for σ and τ represent the tensile and shear resistances, respectively.

Since $\varphi = 0°$ it is obvious that $\tau = 0$ throughout the debonding process. At point 1 (circled number), yielding of the matrix occurs (while the precipitate is still attached to the fiber). Point 2 specifies the location of peak resistance, after the precipitate debonds from the fiber at "A". (The stress concentration at the precipitate causes it to debond at a stress lower than $T_{ip} = 1$ GPa.) The normal stress continues to increase slightly after precipitate decohesion because of the nucleation that occurs when the traction on the precipitate is released while the loading displacement simultaneously increases. After the peak, the cavity grows quickly under decreasing tensile resistance (i.e. point 3). Positions 4 and 5 show how the ligaments are sheared under increased interaction with neighboring cells. Finally, the matrix ligament separates at point 6 when it reaches the critical plastic strain to fracture ε_f^p.

Figures 2-6(a,b), 2-7(a,b), and 2-8(a,b) depict the simulation results for $\varphi = 30°$, $60°$, and $85°$ respectively. The letters and numbers in the figures have the same meaning as those in the figures for pure tension. It is evident from the figures that the addition of an imposed shear displacement has the effect of reducing the tensile resistance σ while increasing the overall displacement δ where precipitate decohesion occurs. Furthermore, the fact that the shear resistance τ drops off immediately after precipitate decohesion (point A), indicates that the precipitates provide the majority of the resistance to the imposed shear of the system. Indeed, the greater the applied shear displacement (which indicates a larger phase angle φ), the greater the shear resistance τ. In addition, the sequence of deformed configurations show how the cavity growth becomes more asymmetric, with a tendency toward shear distortions, with increasing shearing component of loading.

2.4 Experimental Procedures

2.4.1 Specimen Description and Fabrication

The ultimate goal in creating a test specimen for use in interface separation experiments was to ensure that the sample effectively represented the environment created

for the tension/shear: traction/separation simulations (Section 2.2 and Figure 2-4). This was accomplished through the specimen shown in Figure 2-9. Essentially, the sample consists of a single crystal sapphire substrate coated with an Fe dot pattern sandwiched in between Al cylinders. The clear substrate is 25.4 mm in diameter and 2 mm thick and is manufactured by Meller Optics, Inc. Since it is composed of Al_2O_3, it represents the fiber in the system. The coating on the substrate is a representation of the precipitates that develop during casting in between the matrix and the fiber. Fe was chosen because of its tendency to adhere well to Al during diffusion bonding and adhere poorly to Al_2O_3, in an analogous manner to the Al_2Cu precipitates found in the actual composite. Furthermore, Fe can be easily deposited on a substrate and is not likely to entirely dissolve into the Al during bonding. The intermetallic compound that develops in the bonding of the Fe and the Al ($FeAl_3$) is similar to the Al_2Cu precipitates that are created during casting of the actual composite. In the mathematical model, the distance between precipitates is 5 μm, and the associated diameters are chosen to create an area fraction of 0.2. Deposition of 5 μm "islands", however, is quite manufacturing intensive and costly and will most likely result in test specimens that are difficult to fabricate and analyze. Thus, the size of the representative precipitates was increased to 0.45 mm in diameter at a spacing of 1.00 mm. (Scaling and normalization of results will eventually allow for the comparison of simulation and experimental results.) The Fe dots were deposited using electron beam deposition to a thickness of 0.5 μm at Lincoln Laboratory. An alumina mask with the desired dot pattern was placed on the substrates during deposition to create the final configuration.

The Al cylinders on either side of the substrate represent the matrix that entirely surrounds a fiber. The sizes of the cylinders were based on the constraints of the materials testing machine. 99.999% pure Al is bonded to the side of the substrate with the dot pattern in order to take advantage of the deformation characteristics of the pure material. The unconstrained necking of the Al presents a clear image of how the matrix separates from the fiber in an actual composite. A graphite slug is inserted into the middle of the pure Al to inhibit the adherence of the two materials

in the center region of the bond. This serves to prevent high torsional stresses from developing in the center of the bond and to create a separation stress that is within the test constraints (a bond that is "too strong" cannot be separated in the tension test because the Al cylinders will begin to slip in the grips). An 1100 Al alloy is used in the remainder of the upper cylinder and in the entire lower cylinder. All surfaces of the Al cylinders were machined using a lathe with no cutting fluid.

All of the components in Figure 2-9 are individual entities prior to bonding. They become one specimen through the diffusion bonding process. Bonding took place in a Centorr vacuum chamber, shown in Figure 2-10(a). The vacuum is necessary in order to prevent an oxidized surface from developing between the Al and the substrate which would contaminate the bond. Pressure was applied by an Instron servohydraulic materials testing machine, and heating occurred via an induction generator running current through a copper coil surrounding the specimen.

Several pieces in addition to the specimen components were necessary in order to create an adequate test sample. These pieces are depicted in Figure 2-11 (detailed drawings of the components are included in Appendix A). A graphite mold holding the unbonded specimen components was used for two reasons. First, the bonded sample must be perfectly aligned in order for it to properly fit into the material testing machine and result in an accurate test. Secondly, as temperatures in the system increase and more pressure is placed on the bond, unconstrained Al will have a tendency to creep and deform into a "barrel" shape. The mold ensures that the specimen will maintain its cylindrical shape and approximately its original dimensions. Stainless steel machine screws and nuts along with copper and Belleville washers keep the two halves of the mold together throughout the process. Graphite sleeves are placed around the Al cylinders to prevent the cylinders from bonding to the mold. When the specimen is extracted from the mold, the sleeves, which have slightly bonded to the Al, are easily cracked and removed from the cylinders allowing the mold to be reused. Graphite disks are placed above the upper Al cylinder and below the lower cylinder. The lower disk prevents the Al from bonding to the platform on which it rests, while the upper disks protrudes from the top of the mold and acts as the "pis-

ton" which places pressure on the system. Both disks bond to the cylinders, but this is inconsequential because they crack immediately upon being placed in the grips of the testing machine and thus do not become a continuous part of the material. The entire setup is pushed together by a steel platform which the mold rests on (and is connected to the Instron's actuator) and a steel disk which is placed on top of the upper protruding graphite disk. The steel disk is in contact with a round tipped rod (which is connected to the Instron's load cell). Finally, a thin walled graphite tube is placed around the mold (and rests on the platform), leaving a distance of approximately a quarter of an inch between the tube and the mold. The tube is heated by the induction currents generated by the surrounding copper coil. In turn, the heated tube uniformly radiates to the mold, heating the specimen.

Prior to bonding, all components directly involved with the process underwent a thorough cleaning procedure. The specific components cleaned were the Al cylinders (pure and 1100), the graphite cylinders, the graphite slug, and the mold (but only after it was first machined). The substrate was not subjected to the cleaning treatment due to the initial cleaning of the manufacturer and the secondary cleaning performed prior to deposition of the coating. Furthermore, the chemicals used in the cleaning could have had an adverse effect on the deposited coating. After wiping the components with acetone, they were subjected to the following steps twice: rinse with deionized water, rapid dry, sonicate in methanol for ten minutes, rinse with methanol, and rapid dry. Following the cleaning, the components were baked in a vacuum at 150 °C for six hours. Immediately prior to assemblage in the mold, the components were wiped with reagent grade acetone.

Once the components are properly positioned in the mold and the machine screws and nuts are fastened, the mold is placed (inside of the graphite tube) on the platform in the chamber, which is in its lowest position (to allow for the mold to be placed on it without hitting the copper coil). The platform is then raised to a position where the graphite tube and mold are located entirely within the copper coil, as shown in Figure 2-10(b). Two thermocouples are then placed within the tube inside two different holes in the mold to measure the temperature of the mold throughout

the process. Then, the steel disk is placed on top of the upper graphite disk and the setup is positioned so that the steel disk and the upper steel rod are almost in contact. The mold is aligned in the middle of the platform by a groove in the bottom of the platform where the mold rests. Similarly, the upper graphite disk is aligned in the middle of the steel disk by a groove in the bottom of the steel disk where the graphite disk is placed. The "bowl" in the top of the steel disk ensures the round tipped rod will set in the middle of the disk and will be able to compensate for any type of instabilities that may develop.

After the mold, steel disk, thermocouples, and graphite tube are properly positioned, the chamber is evacuated. The chamber is pumped down for approximately twenty-four hours to ensure that an adequate vacuum is created. At the end of this time, an initial preload is placed on the specimen of 250 N and the mold is heated to 150 °C over a period of approximately thirty to forty-five minutes to ensure that a sufficient vacuum is maintained. The temperature remains constant for sixteen to eighteen hours to allow the vacuum to improve and any remaining impurities to bake out of the system. Once this period is over, the temperature is increased to 610 °C over a time of approximately three hours, once again ensuring that an adequate vacuum is maintained. During the temperature increase, when the mold temperature reaches 400 °C, the load is gradually ramped to its final value of 2263 N (which creates 5 MPa of pressure on the specimen). The specimen remains at its final temperature and load for 12 hours. After that time, the temperature decreases to an ambient level while the load is gradually decreased to its initial preload level of 250 N.

Upon completion of the diffusion bonding process, the mold is removed from the chamber and disassembled. The graphite sleeves are removed from the cylinders and a thin coating of SiC is added to the outside of the cylinders to improve their hold inside the testing machine's grips.

2.4.2 Tension Test Procedures

Tension tests of the diffusion bonded specimens were conducted using an Instron servohydraulic materials testing machine equipped with MTS Systems collet grips.

The Al cylinders are gripped under a collet pressure of approximately 25 MPa, leaving roughly 6 mm of each cylinder above and below the substrate ungripped. The load is applied via an imposed displacement rate of 0.152 mm/min and is measured by the machine's load cell. Displacement of the crosshead is measured by the machine's LVDT.

2.5 Experimental Results

Over thirty specimens consisting of the various configurations listed in Section 2.4.1 and Appendix B were fabricated and tested. The problems described in Appendix B prevented the majority of the specimens from providing meaningful data. The first specimen to produce a "successful" test was fabricated in the configuration described in Section 2.4.1 (pure Al at the interface with a graphite insert and Fe "dots" on the substrate). The load-displacement curve for this interface test specimen "A" is shown in Figure 2-12. The initial loading of the bond shows the expected elastic response along with slight curvature indicating plastic response of the matrix. Once the peak load is reached and the "precipitates" ($FeAl_3$ islands) debond from the "fiber" (substrate) the plastic deformation of the Al continues in an approximately perfectly plastic fashion. The test was interrupted at the final point of the plot based on the belief that the behavior shown in the graph was being caused by the cylinders "slipping" in the grips (which had occurred in prior tests). When the crosshead was manually lowered with the specimen still in the grips, the bond separated at a final displacement of over twice the value at which the test had been stopped. It is clear from the photographs of the bonding surface in Figures 2-13 to 2-17 that the interface separated in the expected manner, but that the separation was nonuniform. The circular areas are regions of intermetallic where the Al bonded to the Fe dots and then separated at the peak load. There are no signs of Fe on the substrate which indicates that the precipitate had good adherence to the Al and poor adherence to the substrate in an analogous manner to the actual composite. Micrographs of the surface in Figures 2-18 and 2-19 clearly indicate the necking of the Al in between the

precipitates that was depicted in the simulations (Section 2.3).

Overall, the physical interface separation surfaces reinforce the behavior predicted by the model. However, the discrepancy in the load-displacement plots is more difficult to explain. Indeed, the pure Al used in the experiment is expected to have a lower plastic deformation resistance and ultimate strength than the alloy modeled in the simulation, but the plateau in the plot in Figure 2-12 is probably caused by a combination of factors. First of all, a portion of the work of fracture most likely contributed to the deformation of the Al far away from the interface (i.e. the portion of the specimen not in the grips but within the 6 mm between the substrate and the grip). This hypothesis is supported by the evidence of necking on the sides of the specimen and also by the distance between the surface of the graphite insert which originally was in contact with the substrate and the fractured Al surface. Prior to the test these two surfaces were in the same plane. After the test the Al surface extended approximately 1 mm above the graphite insert in some locations. Furthermore, the Al separation surface is not flat indicating that the debonding process was nonuniform. (This is also the reason that the results are presented in terms of load rather than stress. Stress would be difficult to calculate because the actual area remaining in contact with the substrate during the separation at any one time is unknown.) Ultimately, the load measured in the test was most likely a representation of the combined strength of the bond and the pure Al far removed from the bond. Had the load purely measured the strength of the bond the load-displacement curve may have more accurately depicted the behavior of the separation.

Attempts to repeat fabrication of specimen A using the same configuration failed for various reasons. Problems were encountered during the bonding process where the loading would become unstable and the mold would shift slightly on the platform. This would result in an applied eccentric load and hence a non-uniform bond. Grooves added to the platform and the steel disk, described in Section 2.4.1, prevented the shifting from occurring in future bonds (shown in Figures 2-11, A-2, and A-14). Tension tests revealed another problem - separation of the *lower* Al cylinder from the substrate (i.e. the side with no dot pattern) at extremely low loads. The source of this

failure appeared to lie in the low creep resistance of the pure Al. Immediately above the substrate the pure Al would crack the thin walled "notch" of the graphite sleeve as it crept under the pressure and temperature of the bonding process (the notch in the sleeve was necessary in order to prevent the sleeve from resting on the portion of the mold used to center the substrate as shown in Figure 2-11). The Al would then "barrel" out and make contact with the mold directly on the ledge above the substrate. This caused a portion of the load placed on the pure Al to be transferred to the mold rather than entirely on the substrate which would in turn place pressure on the lower cylinder. In addition, there was speculation that the substrate may have been tilted at a very slight angle (caused by any slight imperfections on the surface of the Al) which would cause it to "bind" in the mold.

These issues were addressed first by adding an extra 0.13 mm clearance around the substrate to ensure that it would not become caught in the mold. Furthermore, the maximum bonding pressure was maintained while the system cooled down to 500 °C and the bonding configuration was reversed. That is, the pure Al was placed below the substrate (with the dot pattern facing down) and the 1100 Al was placed above the substrate (inside the notched sleeve). This resulted in a good bond on both sides of the substrate, but the creep of the pure Al still created problems. The material "barreled" out yet again around the substrate, but this was inconsequential because it did not come into contact with any part of the mold (such as the ledge) which would minimize the bonding pressure on the interface. However, the Al did "seep" into the area in between the substrate and the mold. This created a higher work of separation at the interface because an effective crack did not develop at the edge of the disk between the Al and the substrate. Since the Al on the radial side of the substrate did not uniformly cover the disk, the separation was nonhomogeneous which in turn caused substrate surface fractures at locations of good adherence and localized stress.

A change in substrate along with the aforementioned modifications (reversing bonding configuration, maintaining maximum load during cooling, aligning mold in upper and lower grooves) ultimately resulted in the best load-displacement results. A

thinner substrate (1 mm) with an improved surface finish produced no surface fractures on the disk. The load-displacement plot of specimen "B", which was fabricated using this configuration, is shown in Figure 2-20. Indeed, the graph generally follows the behavior predicted by the simulations. The significant yielding of the Al prior to precipitate separation is expected because of the low plastic resistance of the pure Al. In addition, the load drastically decreases after precipitate debonding and then eventually flattens once the majority of the separation has occurred. Views of the specimen in Figures 2-21 to 2-23 indicate that the separation is entirely nonhomogeneous. In fact, approximately half of the bonding surface had entirely separated from the substrate at almost half of the maximum load in the decreasing "tail" of the test. This localization of stress also caused the pure Al below the bond to drastically deform creating an entirely nonuniform separation and bonding surface. However, the figures show that the surface contains many of the same attributes seen in specimen A and predicted by the model. The surface deformation isn't quite as dramatic as that of specimen A and this may be due to a lower quality bond. In summary, specimen B does not provide an effective quantitative stress comparison because of the non-homogeneous nature of the separation, but the load-displacement plot and the fracture surface indicate that the general debonding process acts in accordance with predictions.

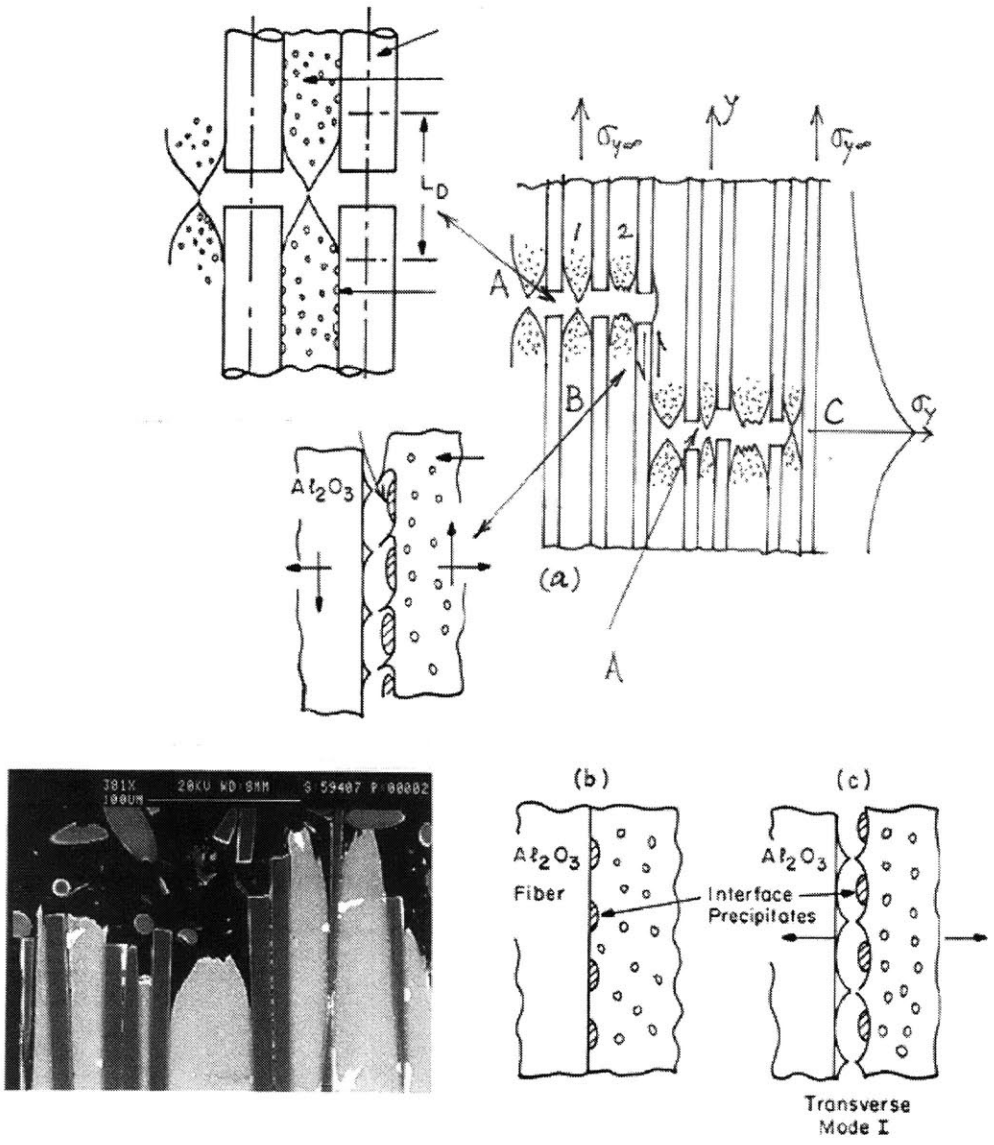

Figure 2-1: Types of interface fracture in an aligned fiber metal matrix composite: (a) mode A of tensile fracture with inset showing debonding length, mode B of simple shear fracture with inset depicting mixed mode of interface debonding fracture; (b) interface precipitates before transverse fracture; (c)transverse mode of interface fracture[1].

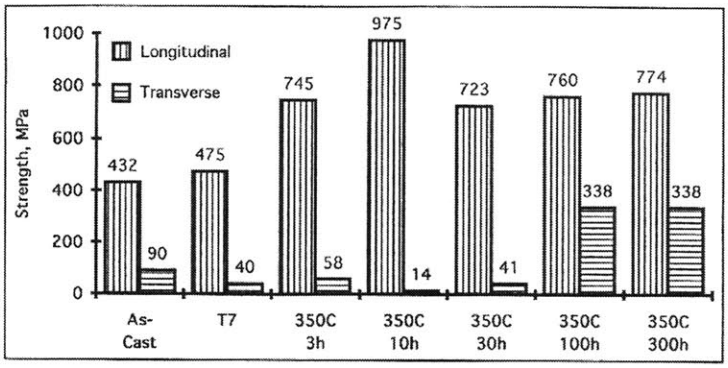

Figure 2-2: Longitudinal and transverse strengths to aging time of Nextel 610/Al-224 composite[1].

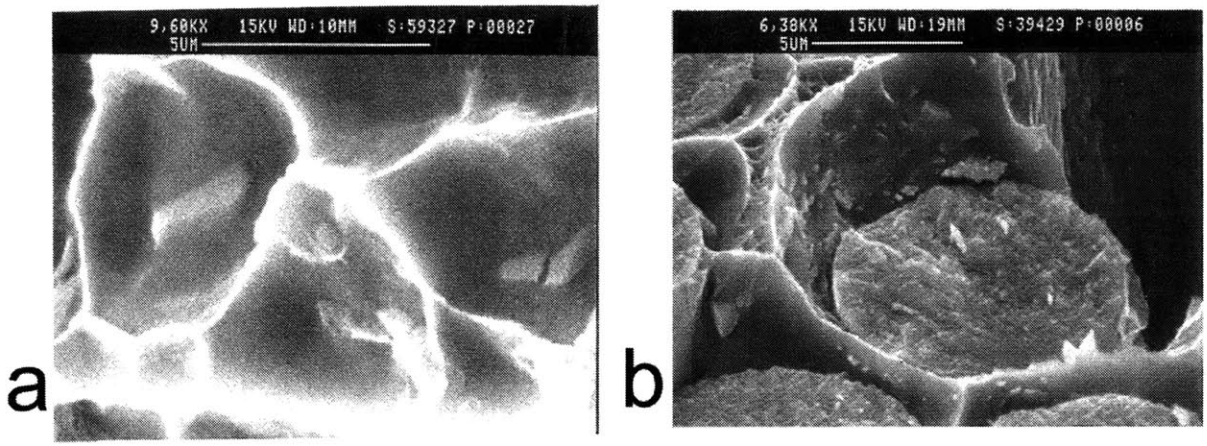

Figure 2-3: (a) Transverse fracture surface with dimples on the matrix side showing precipitate particles that continue to adhere to the Al matrix, (b) fully developed rupture in the remaining metal ligament after fiber fracture[1].

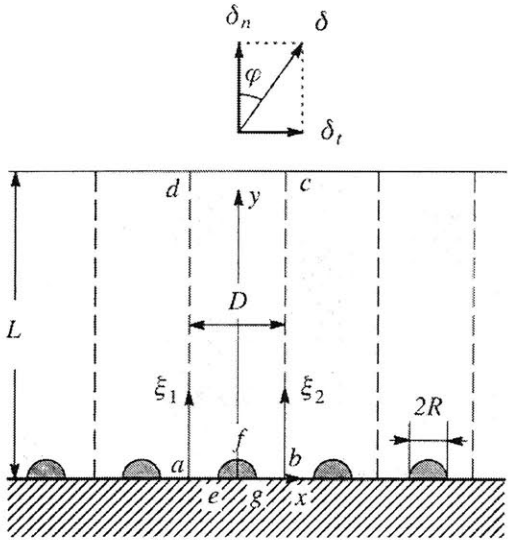

Figure 2-4: Unit cell used in tension/shear: traction/separation simulations; interface with a row of uniformly spaced precipitates[1].

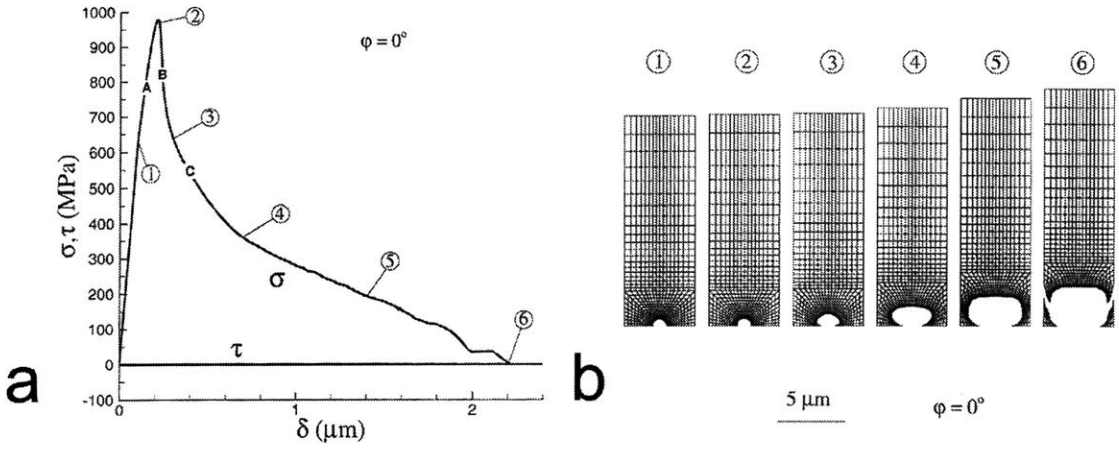

Figure 2-5: (a) Calculated normal stress and shear stress versus total loading displacement under pure tension; (b) sequence of deformed configurations under pure tension ($\varphi = 0°$)[1].

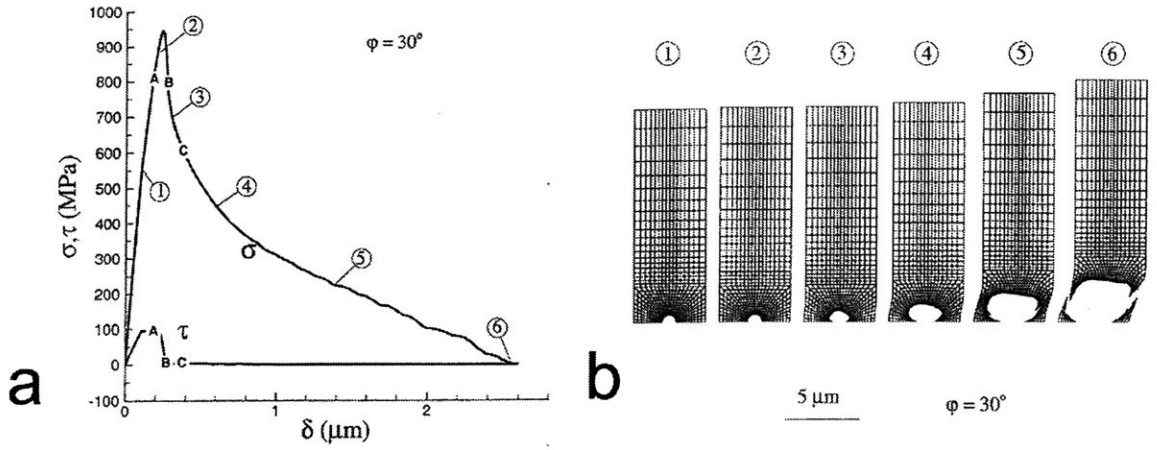

Figure 2-6: (a) Calculated normal stress and shear stress versus total loading displacement under combined tension and shear with phase angle $\varphi = 30°$; (b) sequence of deformed configurations in mixed tension and shear loading[1].

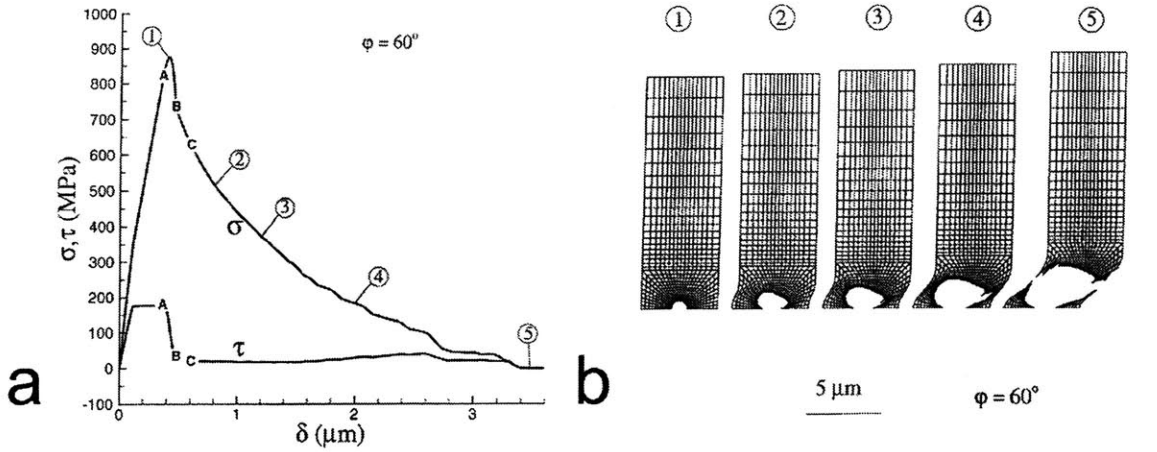

Figure 2-7: (a) Calculated normal stress and shear stress versus total loading displacement under combined tension and shear with phase angle $\varphi = 60°$; (b) sequence of deformed configurations in mixed tension and shear loading[1].

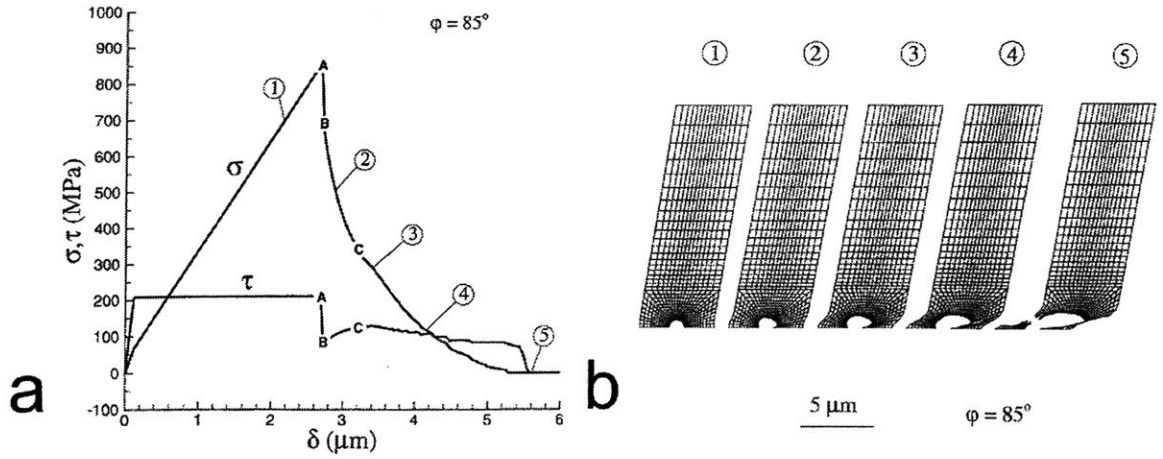

Figure 2-8: (a) Calculated normal stress and shear stress versus total loading displacement under combined tension and shear with phase angle $\varphi = 85°$; (b) sequence of deformed configurations in mixed tension and shear loading[1].

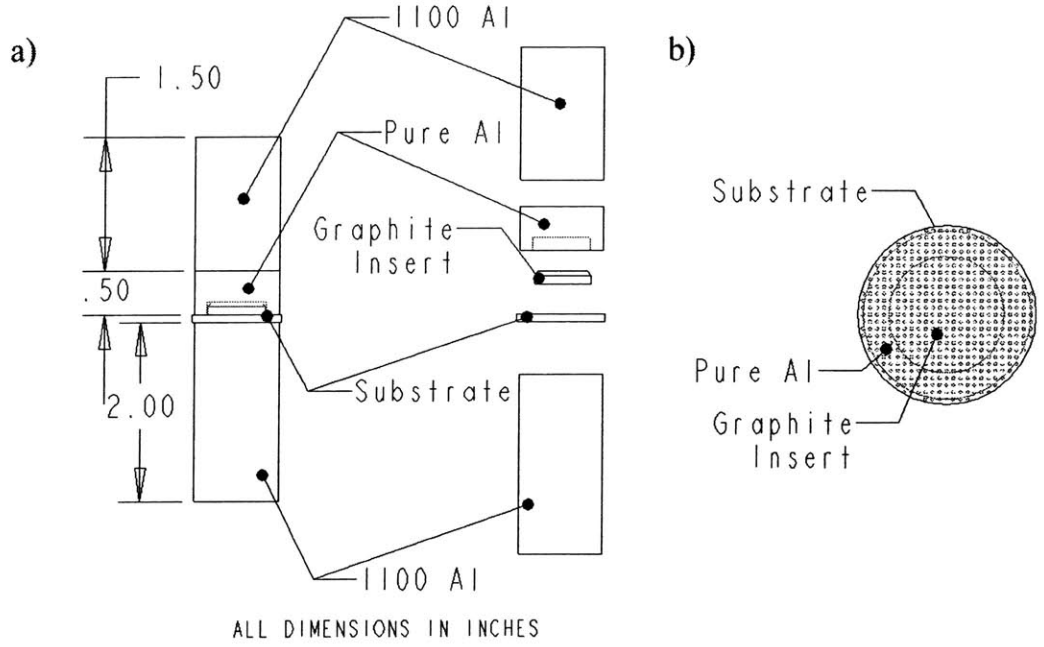

Figure 2-9: Tension/shear: traction/separation experimental specimen: (a) bonded specimen and exploded view of specimen; (b) view of interface from below substrate; dot pattern on other side of substrate, pure Al, and graphite insert seen through clear substrate.

a)

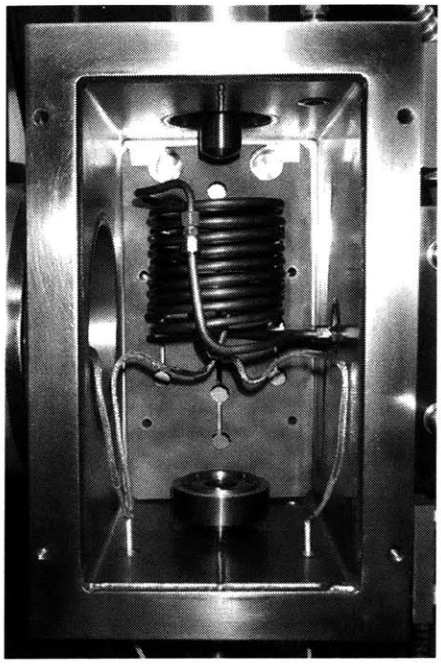

b)

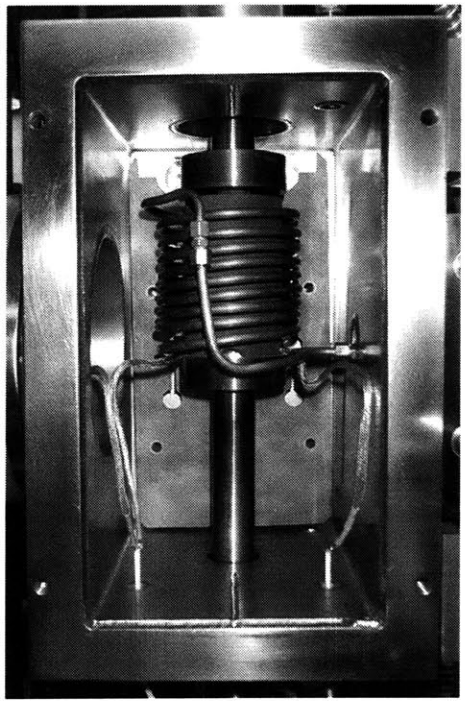

Figure 2-10: Diffusion bonding vacuum chamber with induction coil and Instron testing machine: (a) empty, with platform in lowest position; (b) with mold and graphite tube in bonding configuration.

a)

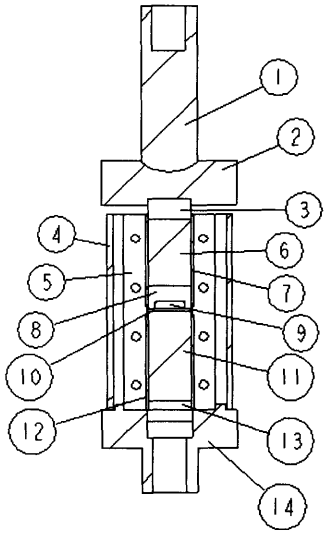

NO.	COMPONENT
1	Push Rod
2	Steel Disk
3	Graphite Disk
4	Graphite Tube
5	Mold
6	1100 Al
7	Graphite Sleeve
8	Pure Al
9	Graphite Insert
10	Substrate
11	1100 Al
12	Graphite Sleeve
13	Graphite Disk
14	Platform

b)

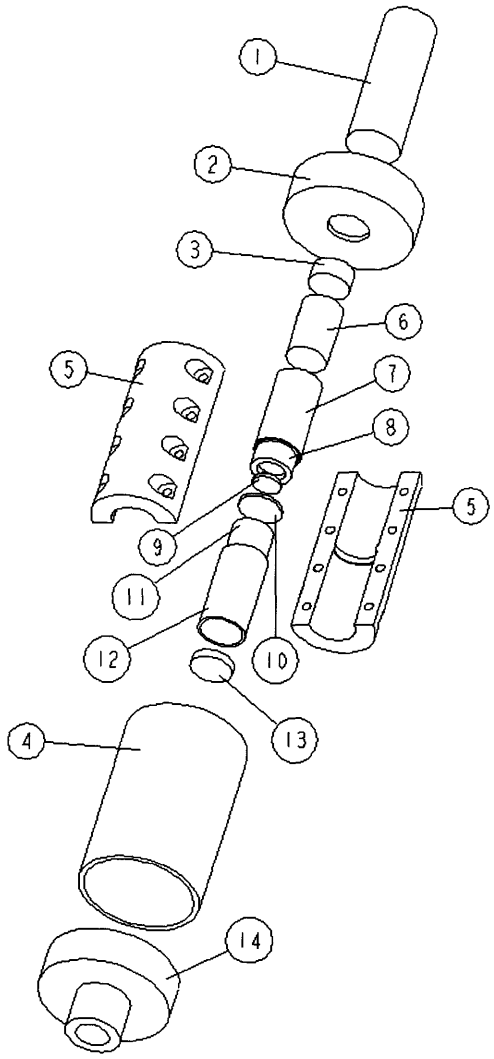

Figure 2-11: Diffusion bonding setup: (a) section view of assembly; (b) exploded view of assembly.

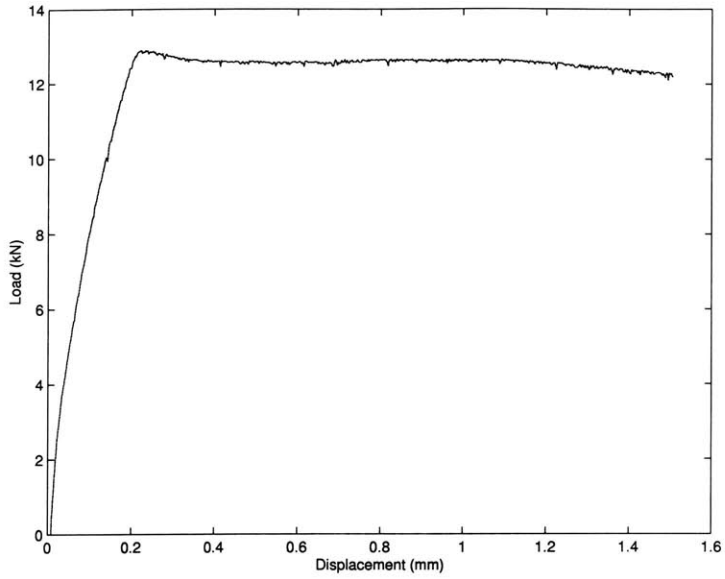

Figure 2-12: Interface test specimen A - load vs. displacement.

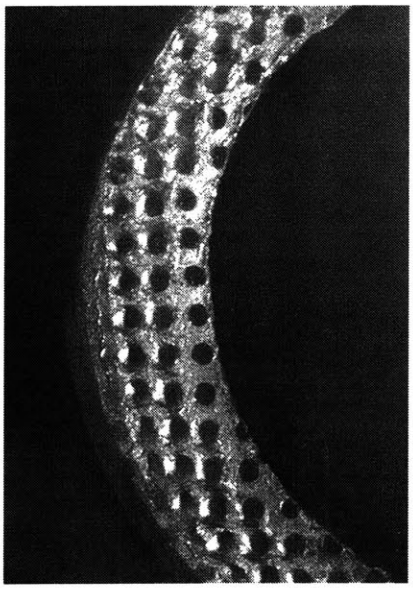

Figure 2-13: Fractured Al bonding surface of specimen A. Deformation is nonuniform across entire separation area.

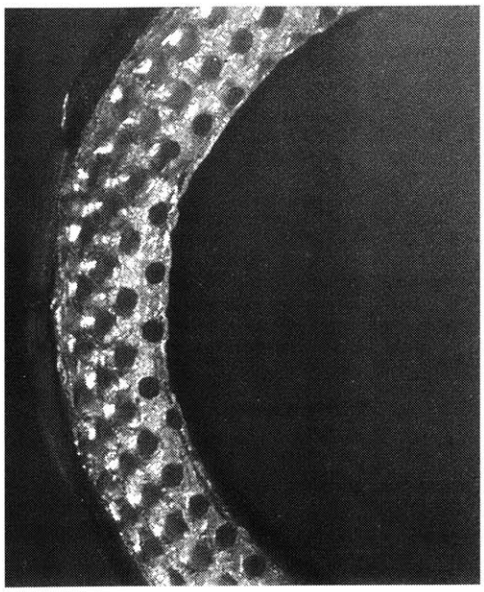

Figure 2-14: Fractured Al bonding surface of specimen A.

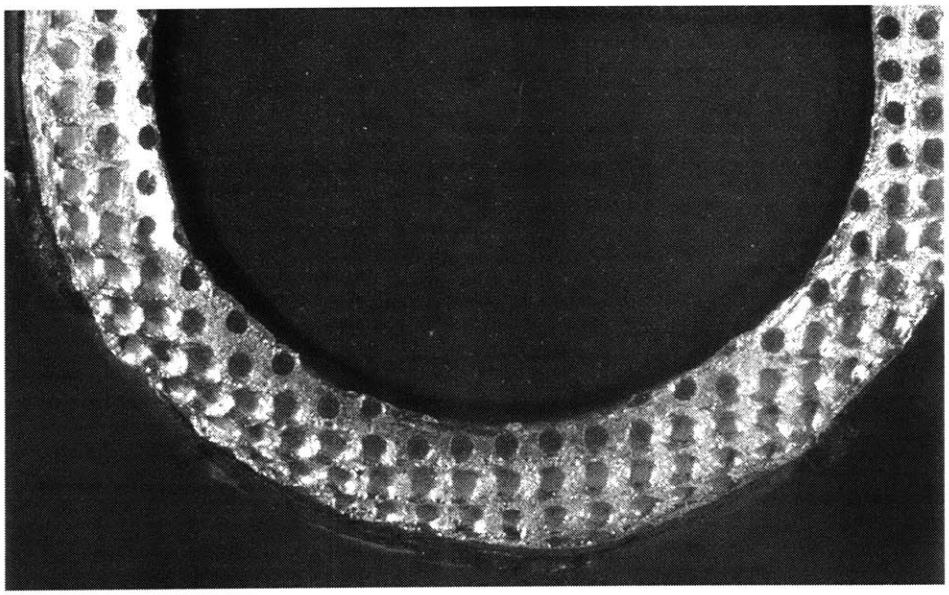

Figure 2-15: Fractured Al bonding surface of specimen A.

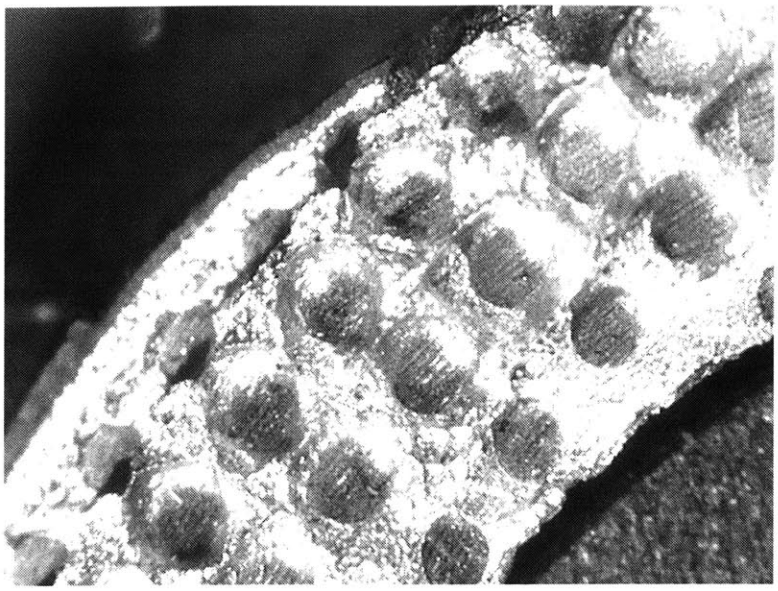

Figure 2-16: Fractured Al bonding surface of specimen A. Necking in between "precipitates" is quite evident.

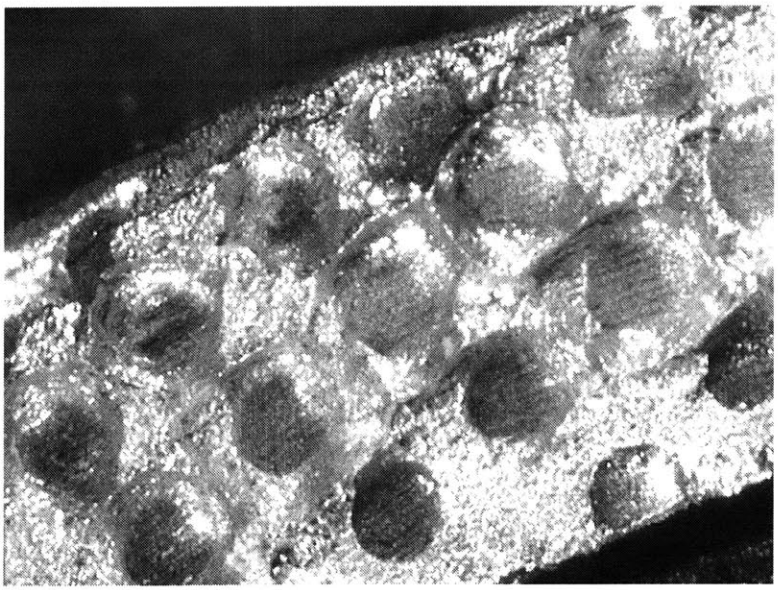

Figure 2-17: Fractured Al bonding surface of specimen A.

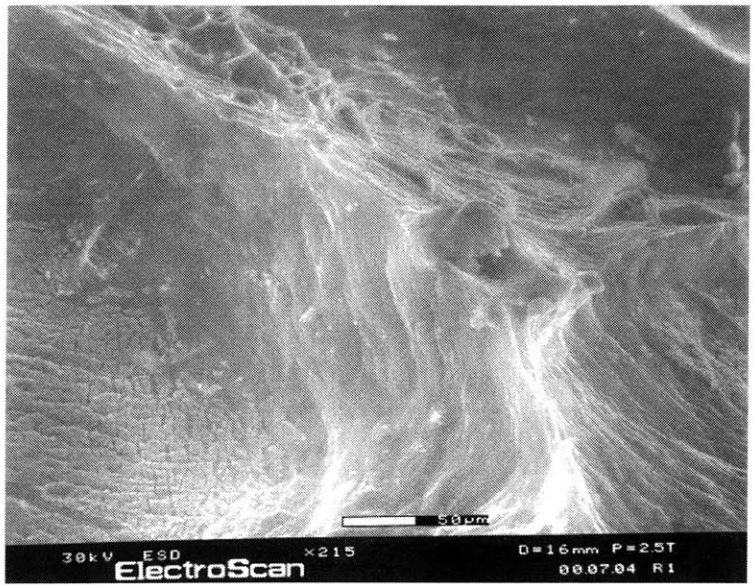

Figure 2-18: Micrograph of fractured Al bonding surface of specimen A depicting necking of the material in between "precipitates".

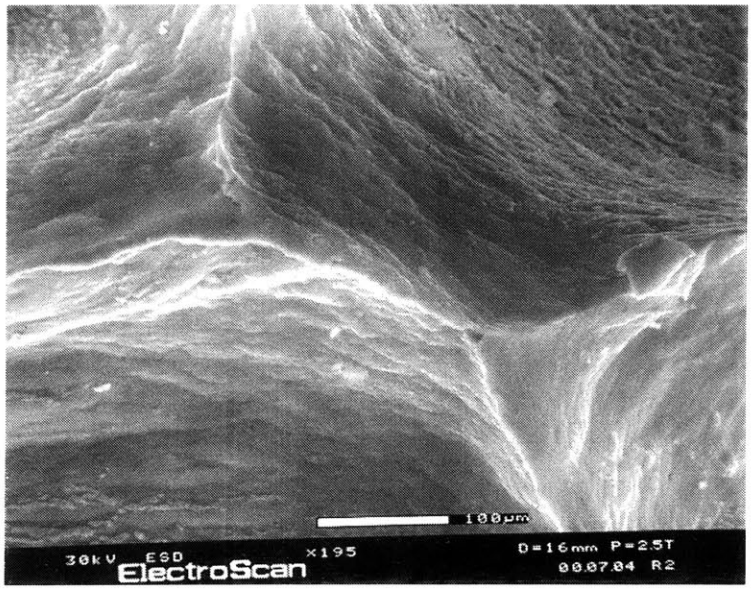

Figure 2-19: Micrograph of fractured bonding surface of specimen A.

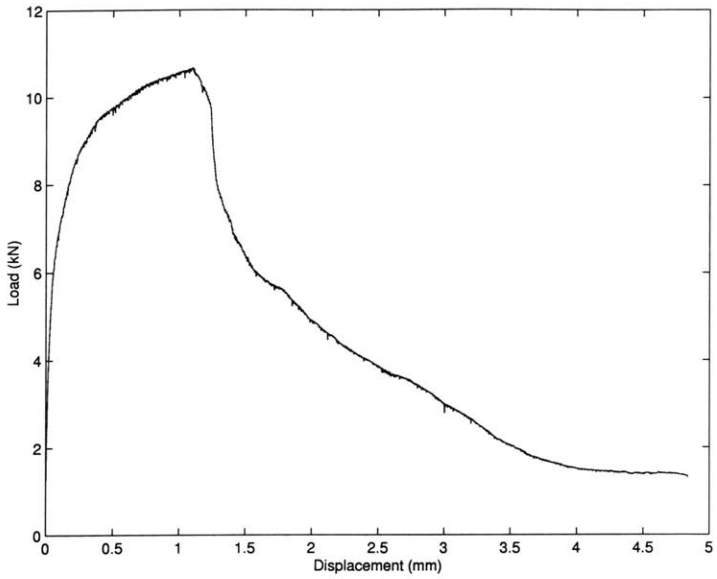

Figure 2-20: Interface test specimen B - load vs. displacement.

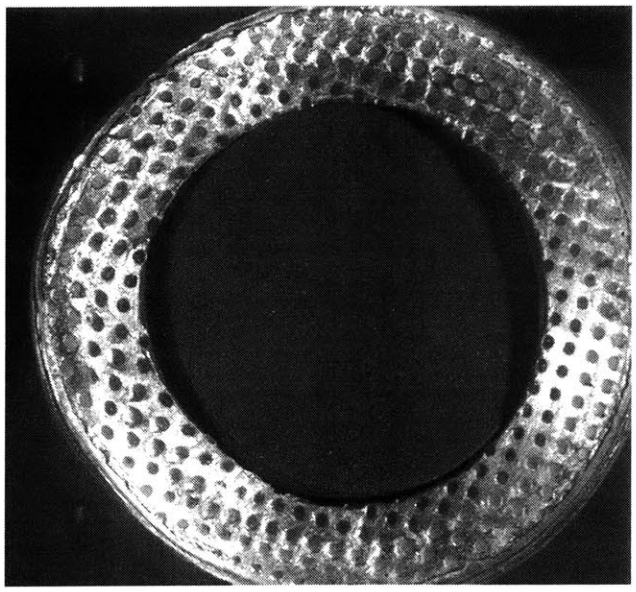

Figure 2-21: Fractured Al bonding surface of specimen B. The skewed angle of the graphite insert and the gap in between the insert and the surface are attributed to nonhomogeneous deformation of the material.

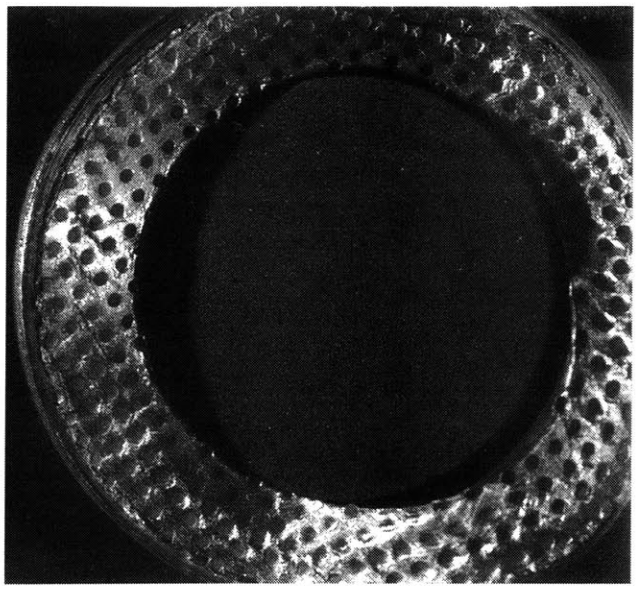

Figure 2-22: Fractured Al bonding surface of specimen B. The specimen is rotated 180° from the position shown in Figure 2-21.

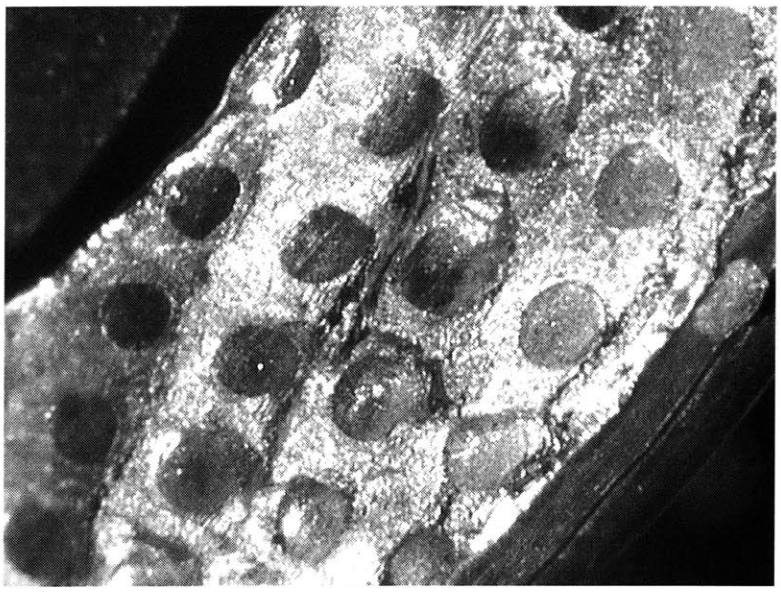

Figure 2-23: Fractured Al bonding surface of specimen B. Necking in between "precipitates is particularly evident.

Chapter 3

Experiments With Composites Containing Infiltrated Fiber Preforms

3.1 Motivation

The primary goal behind investigating MMC's reinforced with "felt-like" fiber preforms is to obtain improved mechanical and thermal performance over the unreinforced matrix while utilizing a relatively low cost manufacturing procedure. A MMC reinforced with aligned continuous fibers will have greater strength and stiffness in the direction of the fibers than the MMC reinforced with felt-like preforms, but these benefits come at the cost of a higher fabrication price. Furthermore, the MMC reinforced with preforms can be manufactured by infiltrating a fiber preform consisting of randomly oriented continuous fibers which provide the material with quasi-isotropic behavior. The precipitates that develop at the interface between the fibers and the matrix could be expected to have the potential to produce many of the same benefits as those relating to MMC's reinforced with aligned continuous fibers discussed in Chapter 2. Controlling the precipitate size and distribution on the infiltrated fiber preform in order to optimize the mechanical behavior of the material could make

this type of MMC an attractive material option in many design applications where improved mechanical properties over a typical alloy at a relatively low manufacturing cost are desired.

3.2 Testing

3.2.1 Material System

A series of tests were conducted in order to properly characterize the behavior of an infiltrated fiber preform. The specific material system examined in the tests consists of an Al-5%Cu alloy matrix and Al_2O_3 fibers. The discontinuous fibers are randomly oriented and are initially part of a preform. The preform used to manufacture the MMC, Fibralloy AL 20, is a product of Thermal Ceramics and is composed of Saffil RF grade alumina fibers along with small amounts of binder agents. The median fiber diameter is 3.0 μm and the approximate median fiber length is 50-70 μm. Casting of the composite was completed using pressure infiltration of the Al-5%Cu alloy at Metal Matrix Cast Composites, Inc. The manufacturing process resulted in a block of the material containing 20% volume fraction of fibers that could then be cut to obtain test specimens.

Once the individual test specimens were cut from the MMC blocks, the samples were subjected to various heat treatments meant to change the size and distribution of the precipitates on the fiber/matrix interface. The specific heat treatment applied to each specimen is described in the appropriate following section, but in general most of the specimens underwent a T7 heat treatment while the remaining specimens underwent a T6 heat treatment. Any overaging was conducted at 350 °C after the initial heat treatment.

3.2.2 Tension Tests

Tension test specimens were cut from a block measuring 101 mm X 101 mm X 6.4 mm to an individual size of 101 mm long, 6.4 mm wide, and 3.0 mm thick. A

total of twenty-one specimens were cut and three of them were then subjected to a T6 heat treatment, with no overaging. The remaining specimens underwent a T7 heat treatment with three specimens associated with each of the following overaging times: 0, 2, 5, 10, 96, and 288 hours. Upon completion of the heat treatment, the wide surfaces of the samples (both sides) were polished to a "mirror" finish. Al "tabs" were then adhesively bonded via an epoxy to the wide surfaces of the specimens where the grips of the material testing machine would come into contact with the samples. The tabs were applied to ensure that the area of highest stress (smallest cross-sectional area) in the middle of the samples would produce the location of material fracture. A diagram of the tension specimen is shown in Figure 3-1.

The tension tests were conducted using an Instron servo-hydraulic material testing machine. The specimens were loaded by an imposed displacement rate of 1 mm/min. Load was measured by the machine's load cell and strain was measured by an extensometer. Figure 3-2 shows the stress-strain behavior of a "representative" sample at each of the various heat treatment and overaging levels (Appendix C shows the test results of each sample). Table 3.1 lists average values of the ultimate tensile strength (UTS) and modulus of elasticity (E) of the tests for each heat treatment and overaging (HT/O).

It is evident from Figure 3-2 and Table 3.1 that UTS decreases with increased aging time. Furthermore, it is qualitatively clear that the yield strength drastically decreases and the strain to fracture drastically increases with any type of overaging at all. The data for the modulus of elasticity was determined from a linear curve fit of the linear portion of the data. However, the linear portion of some of the curves contains few data points, and an extensometer is not the most accurate means of measuring the modulus of a material. Thus, the data is merely included as a qualitative means of comparison with the unreinforced alloy. Moreover, it shows that the material maintains a fairly consistent modulus (within a range of approximately $\pm 10\%$).

Table 3.1: Infiltrated Fiber Preform Experimental Results

HT/O (hrs.)	UTS (MPa)	E (GPa)	VHN (kg/mm^2)	K_{IC} (MPa$\sqrt{\text{m}}$)	J (J/m^2)
T6/0	402.34	80.51	147.60	†	†
T7/0	352.54	73.89	158.20	12.63	0.032
T7/2	300.23	81.32	110.20	†	†
T7/5	282.59	89.44	†	†	†
T7/10	277.06	83.41	89.35	10.79	2601.75
T7/96	210.76	81.20	†	10.37	4574.54
T7/288	222.75	89.43	85.65	†	†

†No data available for this group.

3.2.3 Hardness Tests

Hardness tests were performed on the tension specimens after heat treatment and polishing and prior to tab application. Measurements were collected using a Leitz Wetzlar Hardness tester. Four readings were taken on each sample, giving an average Vickers hardness value for the specimen. The median values obtained for each specimen were averaged once again to create a representative hardness for the level of heat treatment and overaging. The average values for the Vickers Hardness Number (VHN) for each group of specimens are also listed in Table 3.1.

In a similar manner to the UTS, the hardness of the material decreased with increased overaging. Indeed, the VHN for the T7/288 specimens is almost half the value of the T7/0 specimens.

3.2.4 Fracture Tests

Compact tension specimens were fabricated for use in fracture tests. The samples were made from the same material system used in the tension tests, described in Section 3.2.1, but they were cut from a different block with a thickness of 12.7 mm.

Figure 3-3 depicts the configuration of the compact tension specimen (CTS), chosen in accordance with ASTM standard E399. The notch in the specimens were made by electrical discharge machining (EDM), which created a region at the crack tip that was highly susceptible to fracture. Three specimens underwent a T7 heat treatment and one specimen was overaged 10 hours while another specimen was overaged 100 hours. All of the specimens were tested in accordance with ASTM standard E399 using an Instron electromechanical testing machine. Loading occurred by an imposed displacement rate of 1 mm/min and the load was measured by the machine's load cell while the crack opening displacement (COD) was measured by a COD gage. Figure 3-4 shows the load displacement curve for the three tests, and Table 3.1 lists the calculated values for K_{IC}, the plane strain fracture toughness (also determined using ASTM standard E399), and J, the nonlinear energy release rate (also known as the J integral).

It is clear from Figure 3-4 that the overaging has a noticeable effect on the maximum load the CTS can tolerate, the slope at which that load is reached, and the size of the crack which causes it to critically propagate through the entire specimen. Overaging reduces the value of K_{IC} by approximately 15%, but the amount of overaging does not appear to have a great effect on the fracture behavior of the material. The largest difference between the specimens that were overaged and the one that was not overaged is the behavior of the crack after the peak load is reached. Whereas the non-overaged specimen reached fast fracture while the crack was under a load, the cracks in the overaged specimens gradually grew under a decreasing load until the crack had propagated through the entire specimen.

The length of the "tails" in the curves for the overaged specimens in Figure 3-4 indicate that plasticity plays a major role in the fracture process. While K_{IC} is a good indication of the resistance of a material to initial crack growth, it does not accurately characterize the toughness of the material after the crack has developed because it is primarily oriented towards brittle material. J is a measure of the work of fracture of a material and thus, takes into account the behavior of the material throughout the entire fracture process. The values of the J integral listed in Table 3.1

were calculated from the following relationship[14]:

$$J = \alpha\epsilon_0\sigma_0(1-\phi)ch_1\left(\frac{a}{b}, n\right)\left(\frac{P}{P_0}\right)^n \tag{3.1}$$

where

a = crack length measured from pin-line (loading line)

b = distance from pin-line to free end of specimen

$c = b - a$

ϕ = volume fraction of precipitates

h_1 = tabulated function of a/b and n [14]

P = applied load per unit specimen thickness

$P_0 = 1.455\eta c\sigma_0(1-\phi)$

$\eta = [(2a/c)^2 + 2(2a/c) + 2]^{1/2} - (2a/c + 1)$

$\epsilon = \alpha\epsilon_0(\sigma/\sigma_0)^n$

where ϵ is the power-law fit, strain hardening expression relating plastic strains (ϵ) and stresses (σ) with ϵ_0 as the yield strain, σ_0 as the yield stress, α as a fitting constant, and n as the strain hardening exponent. Table 3.2 lists the magnitudes of the quantities used to calculate the J integral. a and b are initial values (prior to testing) and P is based on the maximum load of the fracture test. ϵ_0, σ_0, α, and n are based on the unreinforced alloy tension test plots (Figure 3-9).

The order of magnitude difference between J integral values for the non-overaged material and the overaged material is much more representative of the increased work of fracture associated with the overaged material that is depicted in the "tail" of their load-displacement plots from the fracture tests. Comparison of the values in Table 3.2 shows that the variance primarily stems from the differences in ϵ_0, σ_0, and n, keeping in mind that h_1 and P_0 are derived from these parameters.

Table 3.2: Quantities used in J integral calculations of infiltrated fiber preform fracture experiments

HT/O (hrs.)	T7/0	T7/10	T7/100
a (mm)	22.1	22.0	22.0
b (mm)	39.6	39.5	39.7
ϕ	0.03	0.03	0.03
h_1	0.629	1.161	1.178
P (kN/m)	217.2	196.1	192.0
P_0 (kN/m)	838.6	156.3	118.1
η	0.139	0.140	0.140
ϵ_0 (%)	0.35	0.064	0.051
σ_0 (MPa)	245.34	45.37	33.68
α	1.14	1.63	1.56
n	8.40	3.53	3.42
J (J/m^2)	0.032	2601.75	4574.54

3.2.5 Volumetric Strain Tests

Volumetric strain tests were conducted in order to determine the role cavitation played in the form of the fracture of the material. Specimens were cut from blocks identical to those from which the CTS's were created. Figure 3-5 shows the dimensions of the volumetric strain specimens and the placement of the strain gages measuring strain in the three principal material directions. Even though the fibers are randomly oriented in the plane of the preform, the material cannot be considered isotropic because the infiltration/casting process produces different material behavior through the thickness of the block. Thus, the two gages mounted perpendicular to the direction of loading do not give identical strain readings. The dimensions of the specimens were chosen to allow adequate space for the strain gages, within the confinements of the size of the original block of material. After machining the specimens, they were then given

a T7 heat treatment and one specimen was overaged at 350 °C for 100 hours. All surfaces were polished to ensure a strong bond between the strain gages and the specimens. Tests were conducted on an Instron electromechanical materials testing machine under an imposed displacement rate of 1 mm/min. The machine's load cell measured the load applied to the specimens while the strain gages measured the resulting strain on the surface.

Figures 3-6 and 3-7 show the results of the tests for the specimens with no overaging and 100 hours overaging respectively (supporting data for each of the tests is included in Appendix D). The linear plots on each of the figures is the theoretical prediction of how volumetric strain should increase with stress for a homogeneously deforming elastic material (i.e. without cavitation). The line is determined from the following equation:

$$\epsilon = \frac{\sigma_{11}}{E_1}(1 - \nu_{12} - \nu_{13}) \tag{3.2}$$

where ϵ is the volumetric strain, σ_{11} is the stress in the loading direction, E_1 is the modulus in the loading direction, and ν_{12} and ν_{13} are the Poisson ratios on the respective faces. E_1, ν_{12}, and ν_{13} can be determined from the elastic portion of the tension test, which means the equation for ϵ is a function of σ_{11}. The experimental data is obtained from the strain gage measurements:

$$\epsilon = \varepsilon_{11} + \varepsilon_{22} + \varepsilon_{33} \tag{3.3}$$

where ε_{11}, ε_{22}, and ε_{33} are the strain values from each gage, as depicted in Figure 3-5.

The plots clearly indicate cavitation is occurring during the deformation of the material. This can be seen in the deviation of the experimental plot from the theoretical prediction. The curving upward of the experimental plot indicates an increased emphasis on ε_{11} (the only positive valued term in the experimental equation for volumetric strain) and nonhomogeneous deformation. Yielding of the material occurs at a relatively low stress (depending on the overaging) and this onset of plastic deformation would typically result in a departure of the experimental plot to the right of the theoretical plot since plastic strain increments occur without volume change. The fact that the curve continues to follow the theoretical prediction during plastic

deformation and then shifts upward is a further indication that cavitation is occurring.

3.2.6 Unreinforced Alloy Tension Tests

Tension tests were conducted on the unreinforced Al-5%Cu alloy in order to have a standard of comparison with the infiltrated fiber preform. The material was cast at Metal Matrix Cast Composites, Inc. and then cut into specimens having the configuration shown in Figure 3-8. The thirty-five specimens were then heat treated and overaged in the same manner as the infiltrated preform specimens, as described in Section 3.2.2.

The tension tests were accomplished using an Instron electromechanical material testing machine. An extensometer measured strain while the machine's load cell measured the load on the specimen. The same imposed displacement rate of 1 mm/min used in previous tests was used during the tension tests. Figure 3-9 shows the stress-strain behavior of a "representative" sample at each of the heat treatment/overaging levels (Appendix E shows the test results of each sample). Table 3.3 lists the average values of ultimate tensile strength (UTS) for each heat treatment and overaging (HT/O). The plots in Figure 3-9 span a wide range of strain values, but the individual plots are shown in Figures 3-17 to 3-23 which will be discussed in Section 3.3. In a similar manner to the infiltrated fiber preform, the UTS and yield strength decreased while the strain to fracture increased with increased overaging. Furthermore, modulus estimations showed a fairly consistent modulus of approximately 70 GPa, as expected.

3.3 Data Analysis

Examination of the infiltrated fiber preform results from the tension, hardness, and fracture tests presented in Section 3.2 indicates that any overaging at 350 °C has a significant impact on the mechanical behavior of the material. In the tension tests the yield strength and ultimate tensile strength decreased with increased overaging while the strain to fracture increased as the overaging increased. Furthermore, the hardness

Table 3.3: Unreinforced Alloy Experimental Results

HT/O (hrs.)	UTS (MPa)	Difference from Preform (%)
T6/0	324.68	23.9
T7/0	318.17	10.8
T7/2	258.70	16.1
T7/5	234.27	20.6
T7/10	170.76	62.3
T7/96	153.24	37.5
T7/288	144.55	54.1

of the material diminished along with its fracture toughness while its crack size at fracture in the fracture tests grew with more overaging. The cause of this behavior lies in the development of the precipitates in the matrix and their interaction with the fibers.

In discontinuously and continuously reinforced MMC's, the fibers act as carriers of the precipitates. In this particular alloy, all of the copper is in solution when the material is cast. During the heat treatment process, some of the copper comes out of solution as Al_2Cu precipitates. When equilibrium is reached, the area fraction of the precipitates on the fibers remains constant. However, the average size of the precipitates will increase as aging continues because the larger precipitates increase in size at the expense of the small ones that are shrinking. This has the effect of monotonically reducing the interface energy.

Micrographic evidence of the precipitate coarsening is shown in Figures 3-10 through 3-16 which depict the fracture surfaces of infiltrated fiber preform tension test specimens at each of the heat treatment/overaging levels. In Figures 3-10 and 3-11 where the specimens were not subjected to any overaging the dimples in the alloy and

on any remaining matrix that is still adhered to the fiber are quite small. The effect of the precipitate coarsening is seen in Figures 3-12 through 3-16 where the dimple size monotonically increases with the amount of aging. In particular, the nonuniformity of the alloy fracture surface in Figure 3-16 with the most overaging indicates that the shape of the precipitates not only increases but also becomes more irregular.

The fracture surfaces also give an indication that cavitation may be occurring in regions surrounding the precipitates. This is verified by the volumetric strain tests. Both Figures 3-6 and 3-7 show a significant departure of the volumetric strain from the homogeneous deformation norm. The T7/100 hours specimen particularly shows a steep increase in the volumetric strain shortly before reaching the ultimate tensile stress.

The combination of precipitate coarsening and cavitation help to explain the behavior of the infiltrated fiber preform in the tension, hardness, and fracture tests. Any overaging increases the size of the precipitates in the alloy and causes the matrix to soften, as indicated in the hardness test results in Table 3.1. This "softening", a result of the precipitates being larger than the "optimum" size at peak aging, is what causes the overaged material to yield at a much lower stress level than the T6 and T7 specimens with no overaging, shown in Figure 3-2. However, the lower stress merely means that the cavitation is delayed. In the non-overaged specimens, the cavity inception stress is relatively high when the matrix yields, resulting in a low strain to fracture. The overaged specimens, conversely, build up to the critical cavity stress over a longer strain increment.

These same principles play a significant role in the fracture tests where the peak load of the non-overaged specimen is higher than that of the overaged specimens, but the overaged specimen undergoes measurable plastic flow prior to undergoing crack extension, as seen in Figure 3-4. Once again, the matrix in the non-overaged specimen can withstand a higher load than the overaged specimens, but the cavity inception stress is high enough that the critical crack size is relatively small. However, unlike unreinforced Al, there is a very gradual downward portion to the load-displacement fracture curve. This is the portion of the curve where the matrix has already un-

dergone plastic flow and the disengaging cracked fibers are slowly separating and are being pulled out from the matrix. This effect is much more prevalent in the overaged specimens. The cavity inception stress is lower when the matrix yields which indicates that more plastic strain will be necessary to create the amount of stress required to cause critical fracture. This prolonged plastic separation demonstrates that the fiber "pullout" effect has more of an opportunity to develop. The fiber pullout and cavity stress development create the longer "tail" on the overaged specimens' plots. This indicates an explanation for the misleading K_{IC} values given in Table 3.1. Indeed, the non-overaged specimen has a higher K_{IC} because it can withstand higher loads before crack initiation and demonstrates little plastic behavior. But the overaged specimens showing larger plasticity effects have higher "toughnesses" in the sense that they posses a larger work of fracture as the material response significantly departs from linear elastic fracture behavior. This behavior is more succinctly described by the J integral which accounts for the variance of plasticity among the specimens. The large difference between the values for the non-overaged and overaged specimens is attributed to the plastic properties of the matrix. The lower yield strengths and strains of the overaged materials listed in Table 3.2 are the primary cause of the larger J integral values. This is expected because it accounts for the large precipitate size which leads to the softening of the matrix and the delay of cavity inception. The fiber pullout phenomenon that occurs during the fracture of the material is analogous to chopped fiber reinforced concrete where the fibers act to keep the concrete intact after the matrix has fractured without increasing the peak fracture stress.

There are obvious and expected differences between the behavior of the infiltrated fiber preform and that of the unreinforced alloy. It is clear from Figure 3-9 that the strain to fracture of the material was in some cases an order of magnitude larger than that of the infiltrated preform. The direct comparisons of the two materials in Figures 3-17 through 3-23 highlight the differences in greater detail. Compared to a typical Young's modulus for Aluminum (≈ 70 GPa), the modulus of the infiltrated preform is slightly higher, as listed in Table 3.1. The stiff fibers in the preform material provide it with rigidity above that of the unreinforced alloy, but their random

orientation does not produce a significant advantage because the stiffness is not necessarily in the direction of loading. The fibers also give the alloy increased strength because of their higher load carrying capabilities, which is seen in a comparison of Table 3.1 and Table 3.3. Once again, the improvement is not noteworthy because the fibers do not necessarily provide reinforcement in the proper direction. Finally, the strain to fracture and fracture toughness of the composite are less than those of the unreinforced alloy because of the brittleness of the fibers and the associated increased susceptibility to crack initiation and propagation. This effect is quite likely the most prominent; K_{IC} is reduced by a factor of two to three (compared to a typical Al value of 25-30 MPa$\sqrt{\text{m}}$) and the strain to fracture can be reduced by an order of magnitude.

The aforementioned observations are indeed quite common in composite/unreinforced material comparisons. However, the distinguishing characteristic of this particular system is that the slight gain in modulus and strength properties (at ambient conditions) come at a large price of drastically reduced fracture properties. While the change in fracture behavior is to be expected, the severity of its decrease and the small increase in the modulus and strength are somewhat surprising. As stated in Chapter 1, to truly take advantage of the interfacial properties between the fiber and the matrix, the matrix must be able to sufficiently debond from the fiber to create an increased work of fracture. The precipitates at the interface play a key role in determining the interfacial properties. Unfortunately, the interfaces in the infiltrated fiber preform are not properly oriented in the direction of loading to provide the same benefit. In fact, the various fiber orientations are detrimental to the system because the cavitation debonding of the precipitates from the fiber does not contribute to the work of fracture but rather inhibits it due to interactions of the plastically deforming cavities. While the slight improvement in stiffness, strength, and crack size at critical fracture may be beneficial in certain ambient environment conditions, it is uncertain whether these benefits are worth the increased embrittlement and manufacturing and material costs.

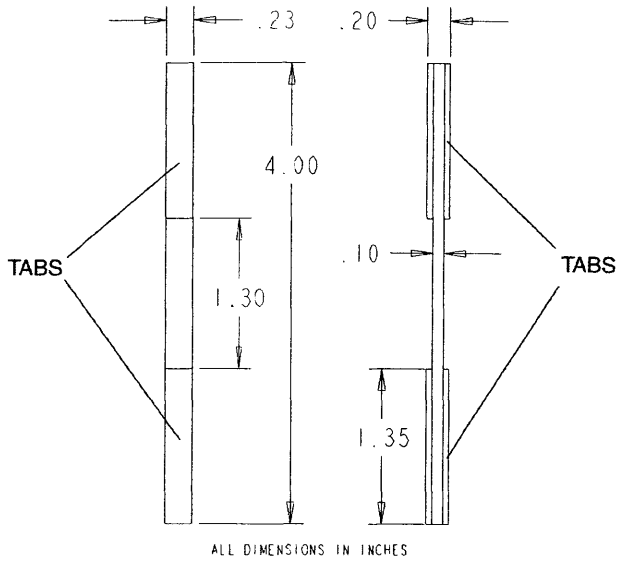

Figure 3-1: Infiltrated fiber preform tension specimen.

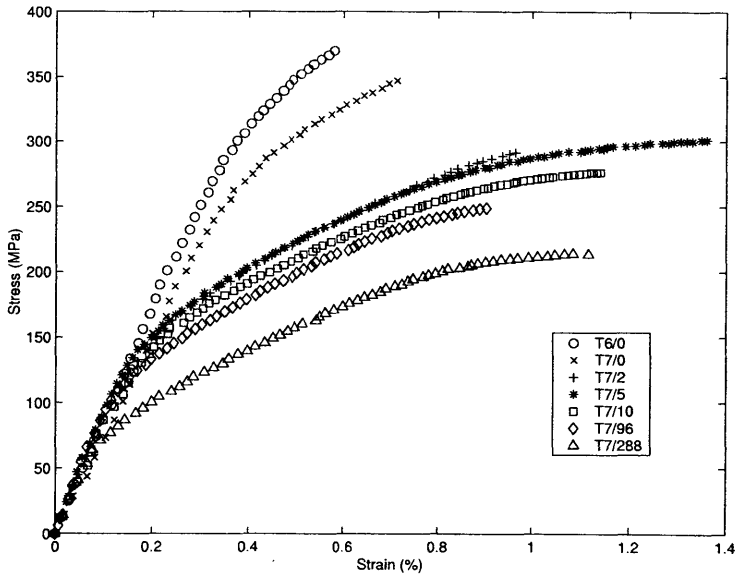

Figure 3-2: Infiltrated fiber preform tension test - stress vs. strain.

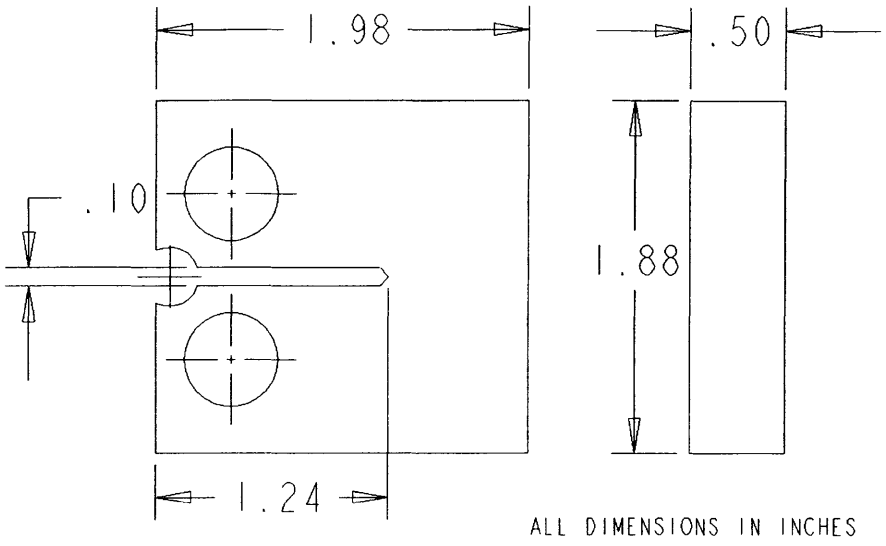

Figure 3-3: Infiltrated fiber preform CTS

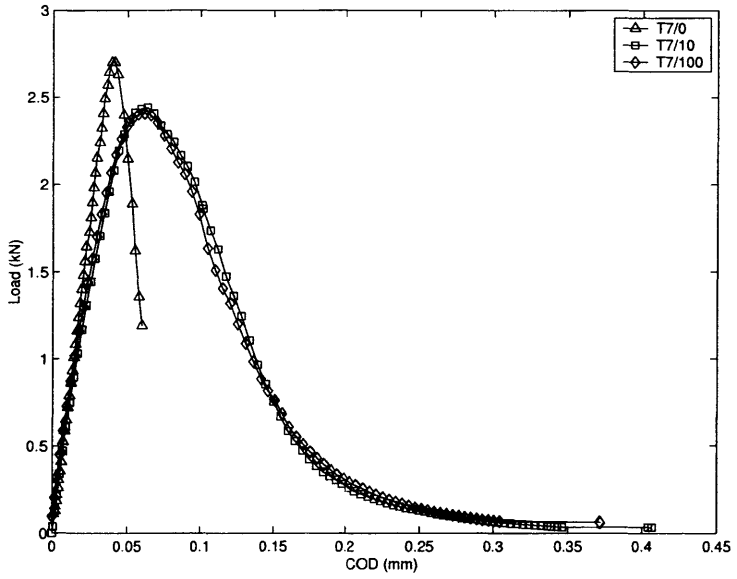

Figure 3-4: Infiltrated fiber preform fracture test - load vs. displacement.

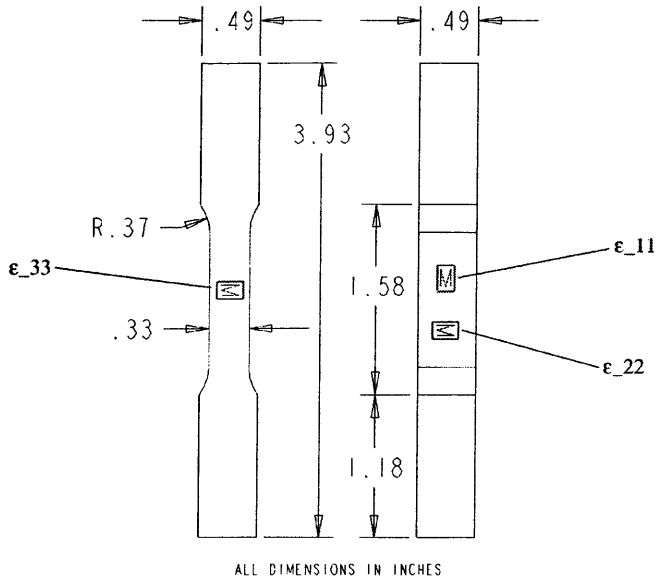

Figure 3-5: Infiltrated fiber preform volumetric strain specimen with associated gages: ε_{11}, ε_{22}, and ε_{33}.

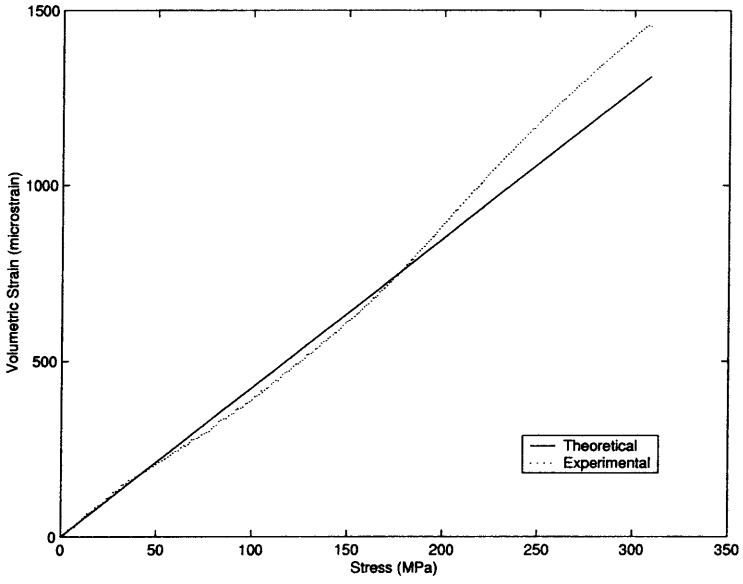

Figure 3-6: Infiltrated fiber preform volumetric strain test - stress vs. strain for T7/0 hours.

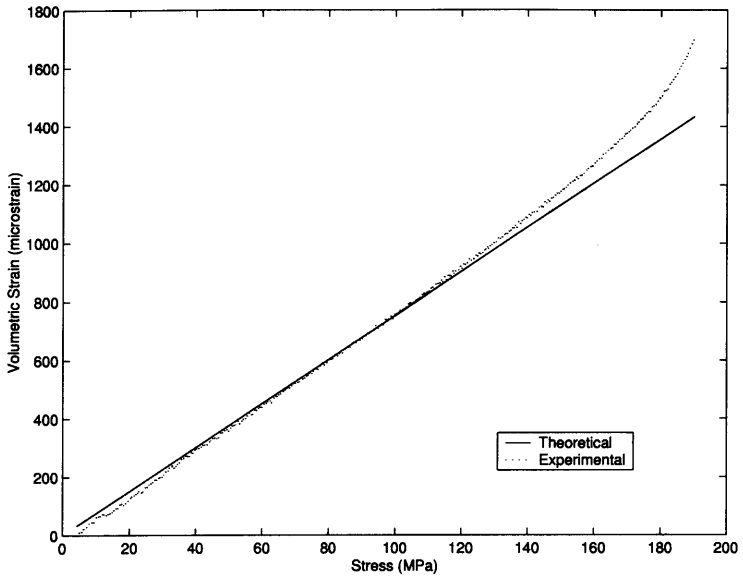

Figure 3-7: Infiltrated fiber preform volumetric strain test - stress vs. strain for T7/100 hours.

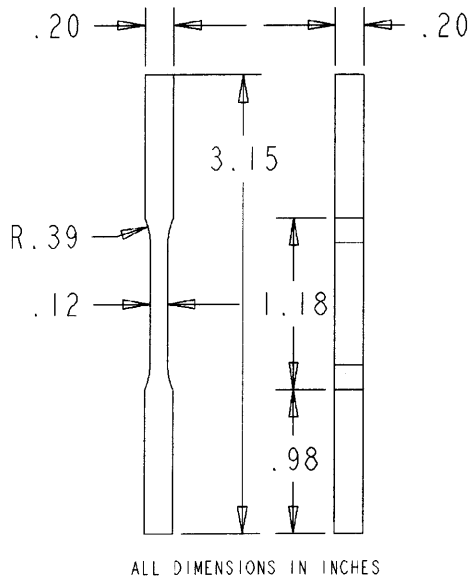

Figure 3-8: Unreinforced alloy tension specimen.

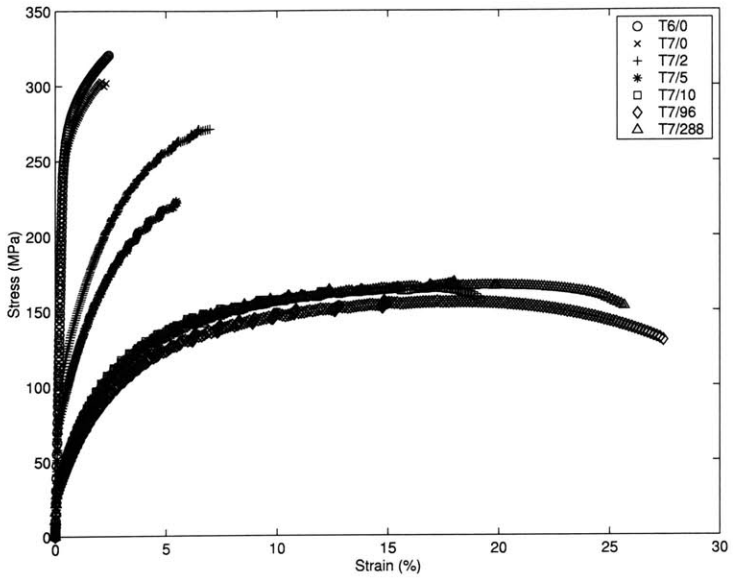

Figure 3-9: Unreinforced alloy tension test - stress vs. strain.

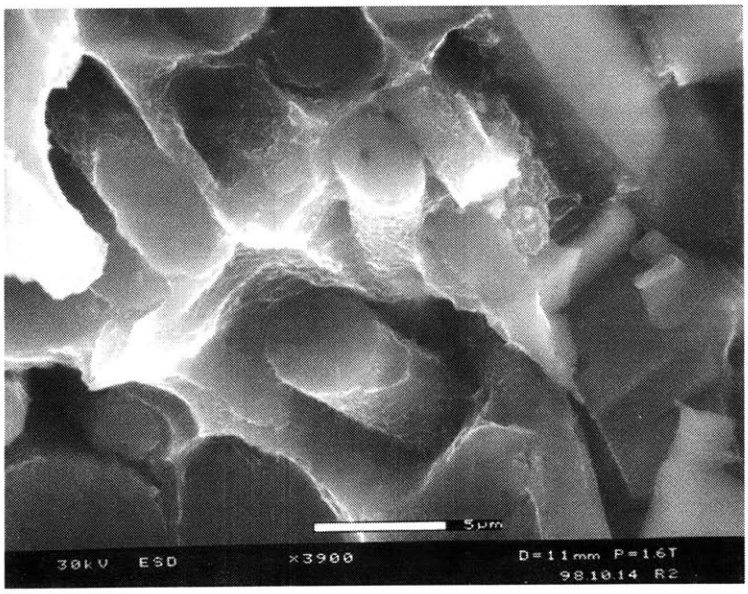

Figure 3-10: Scanning electron microscopy (SEM) micrograph of an infiltrated fiber preform tension specimen fracture surface - T6/0 hours.

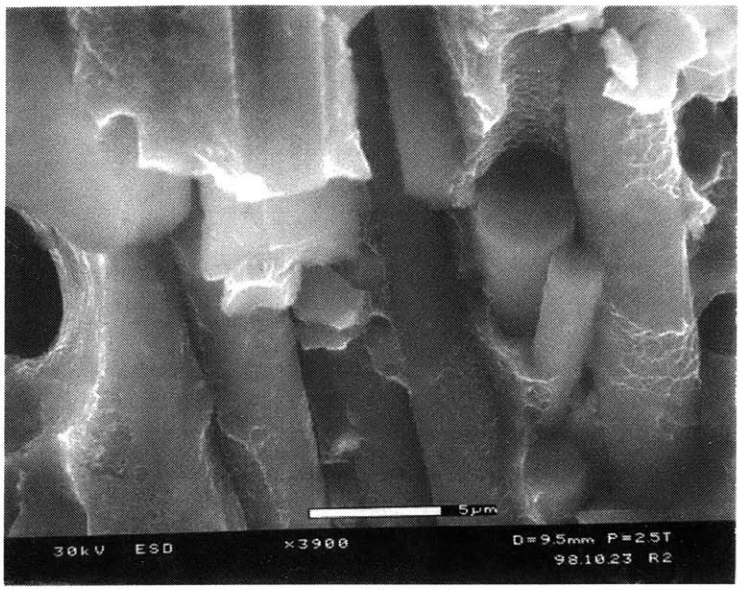

Figure 3-11: SEM micrograph of an infiltrated fiber preform tension specimen fracture surface - T7/0 hours.

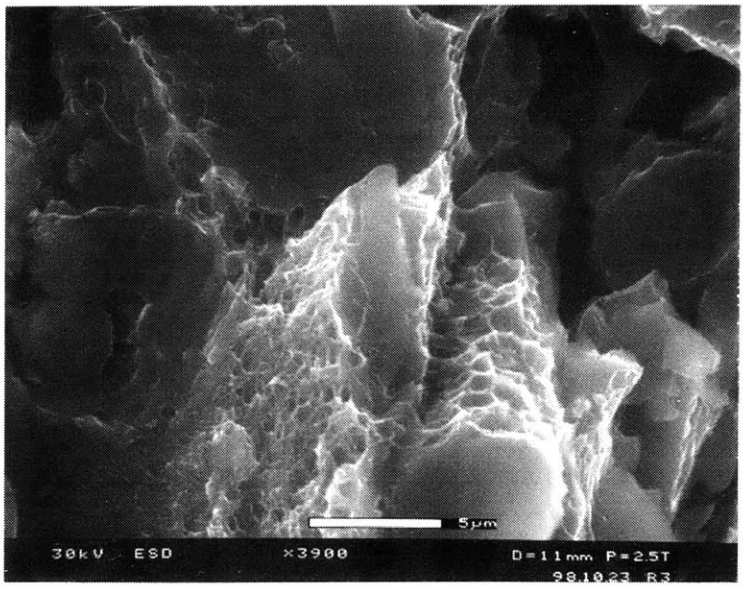

Figure 3-12: SEM micrograph of an infiltrated fiber preform tension specimen fracture surface - T7/2 hours.

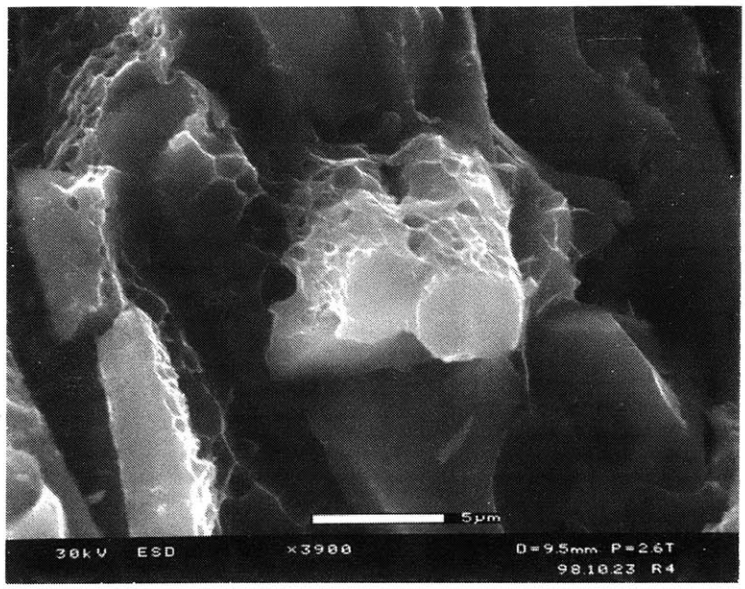

Figure 3-13: SEM micrograph of an infiltrated fiber preform tension specimen fracture surface - T7/5 hours.

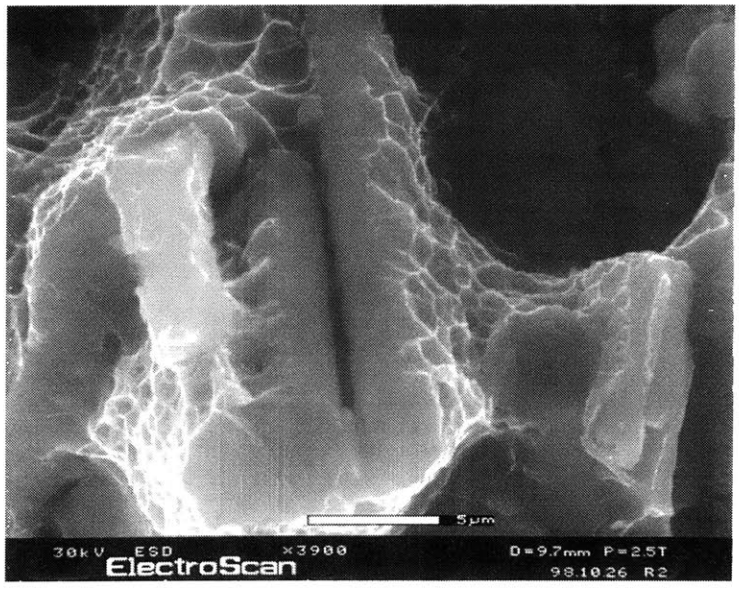

Figure 3-14: SEM micrograph of an infiltrated fiber preform tension specimen fracture surface - T7/10 hours.

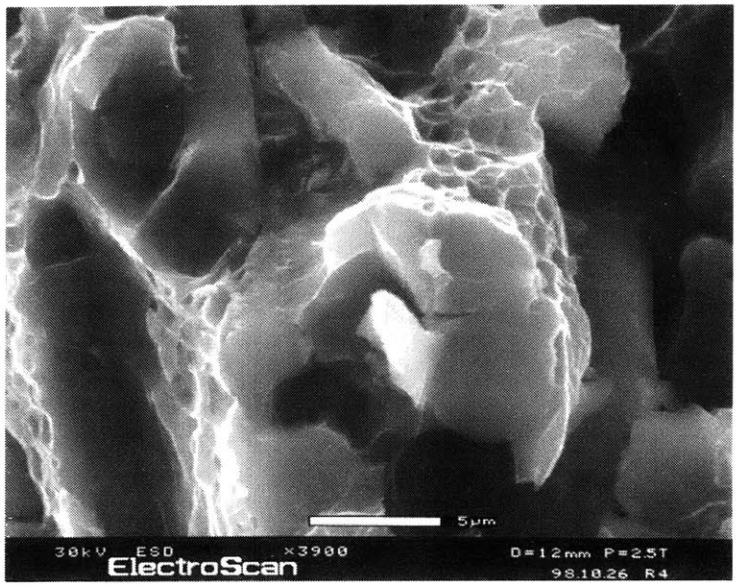

Figure 3-15: SEM micrograph of an infiltrated fiber preform tension specimen fracture surface - T7/96 hours.

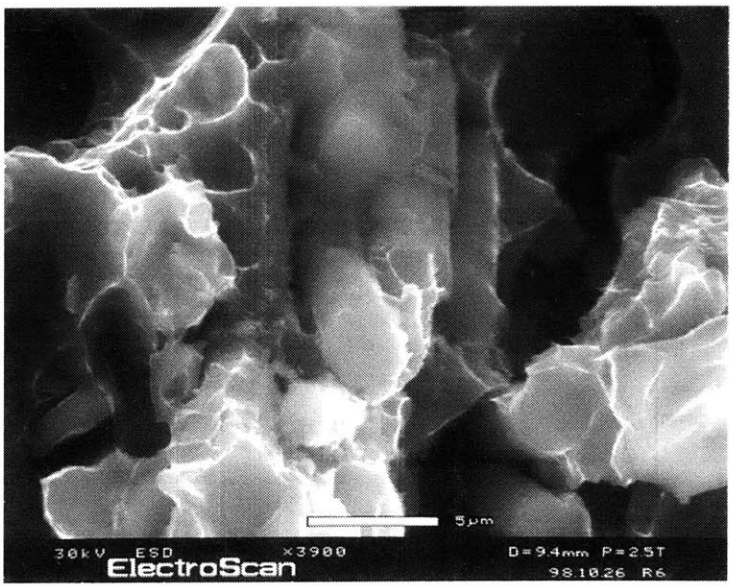

Figure 3-16: SEM micrograph of an infiltrated fiber preform tension specimen fracture surface - T7/288 hours.

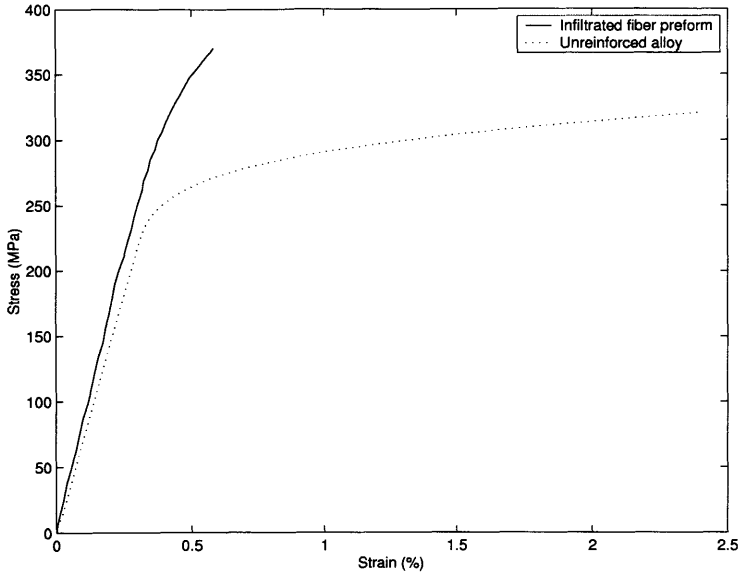

Figure 3-17: Infiltrated fiber preform and unreinforced alloy tension test - stress vs. strain, T6/0 hours.

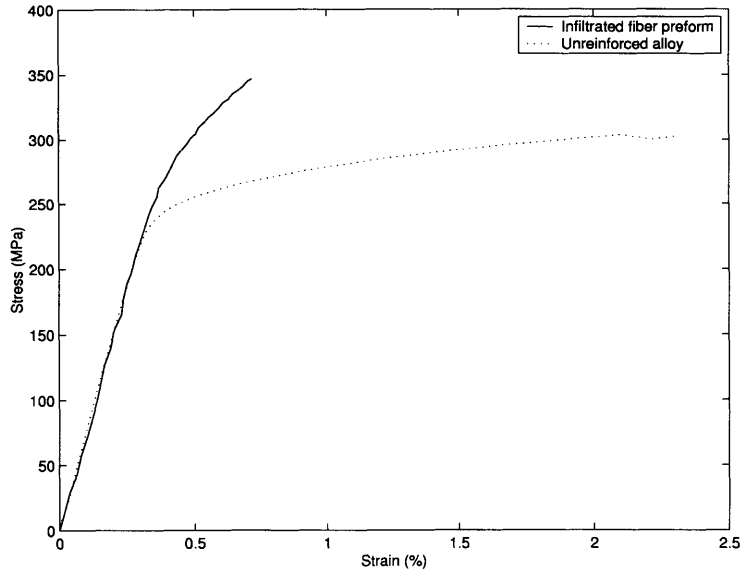

Figure 3-18: Infiltrated fiber preform and unreinforced alloy tension test - stress vs. strain, T7/0 hours.

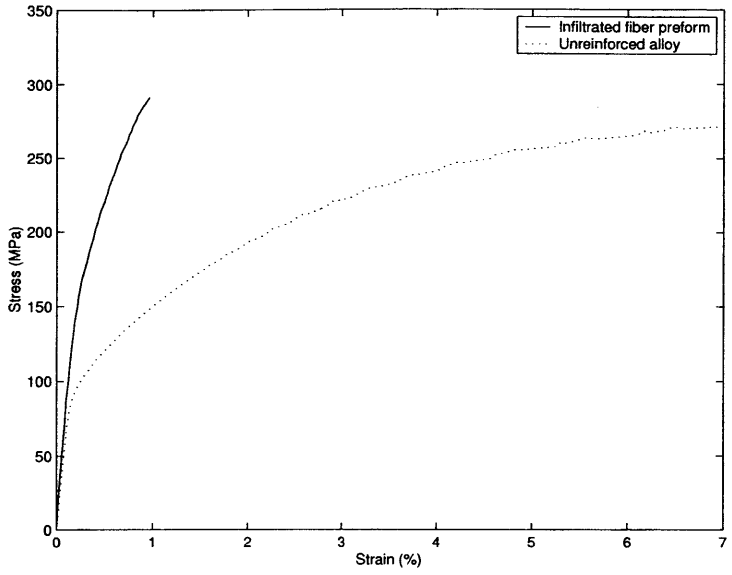

Figure 3-19: Infiltrated fiber preform and unreinforced alloy tension test - stress vs. strain, T7/2 hours.

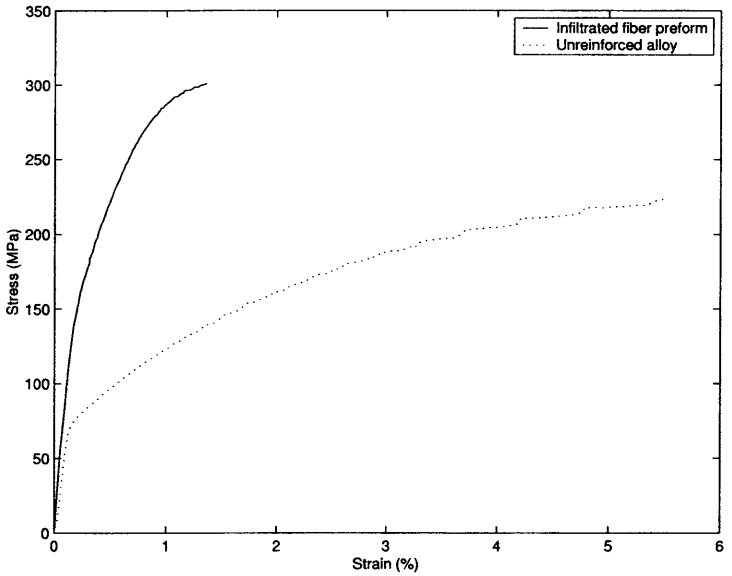

Figure 3-20: Infiltrated fiber preform and unreinforced alloy tension test - stress vs. strain, T7/5 hours.

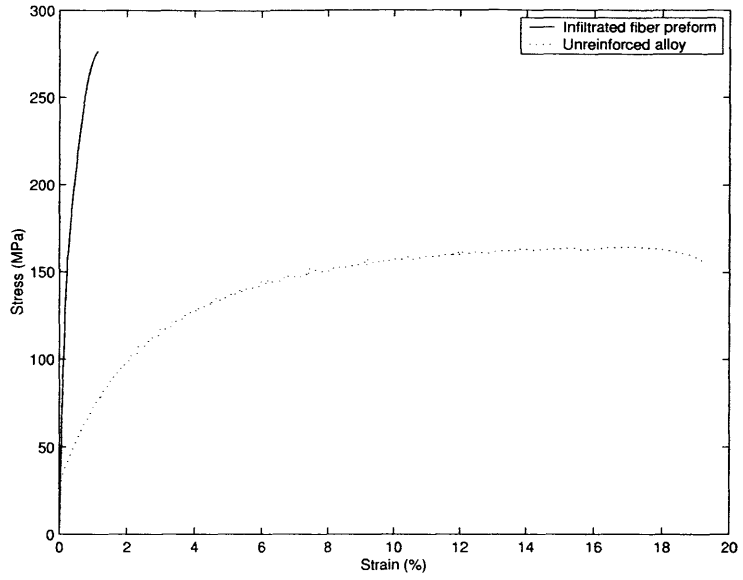

Figure 3-21: Infiltrated fiber preform and unreinforced alloy tension test - stress vs. strain, T7/10 hours.

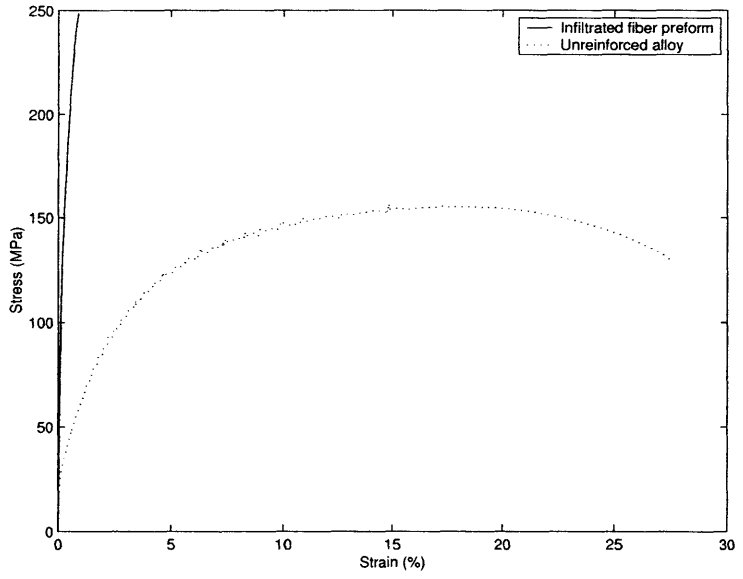

Figure 3-22: Infiltrated fiber preform and unreinforced alloy tension test - stress vs. strain, T7/96 hours.

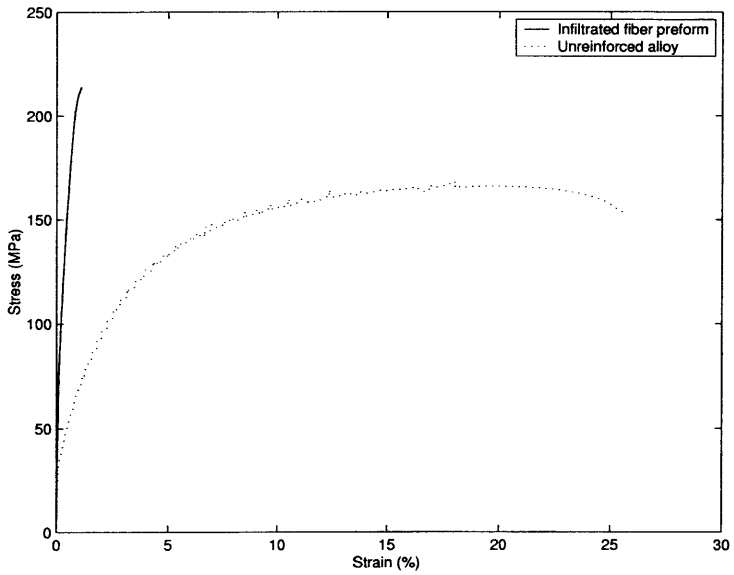

Figure 3-23: Infiltrated fiber preform and unreinforced alloy tension test - stress vs. strain, T7/288 hours.

Chapter 4

Conclusions

Several important steps have been taken to try and gain some insight into the interface separation process that occurs between the matrix and the fiber during fracture of a metal matrix composite. Seleznev's experiments [5] provided information on the characteristics and compositions of interface precipitates in metal matrix composites and the role their size and distribution plays in the strength of the composite. Argon used these results in conjunction with prior work done by himself and other investigators to develop a tension/shear: traction/separation model to describe the fracture process[1]. Liu and Shih then used the model to conduct computations and provide simulations of the interface separation[1]. One goal of this thesis was to contribute another step in the process by verifying the validity of model and simulations through experiments. Mother Nature always has the final word on the ideas of mankind.

As stated in Section 2.5, the interface separation experiments were successful at showing the general behavior and fracture characteristics predicted by the Argon's model are correct. However, the experiment does not provide an accurate means of numerical comparison. Fortunately, the foundation has been laid for the experiment to be effective qualitatively and quantitatively, but a few key points need to be emphasized and followed in future experiments.

- Cleanliness of the components used in the fabrication of the specimen is of the utmost importance for an effective bond.

- The polish on the substrate surface must be of a high quality in order to assure that virtually no surface microcracks remain which could possibly cause premature fracture of the substrate prior to Al/Al_2O_3 separation.

- All of the surfaces which are directly under pressure in the bonding process must be completely flat and perpendicular to their radial surfaces to ensure uniform loading and bonding.

- The load train and the components under pressure need to have the best alignment achievable for the system to provide a uniform and steady bond. This is particularly crucial because the assembly is relatively tall and thus is more susceptible to instabilities.

- Creep of the aluminum components, particularly pure aluminum, should be entirely contained to try to create the desired geometry.

- The temperature and pressure used in the bonding process should be at a level that creates the desired specimens without creating unnecessary problems. This may seem like an obvious point, but trial and error showed that specimens made using a pressure of 2.5 MPa did not have an effective bond, while specimens made using a pressure of 7.5 MPa showed many effects of Al creep. Likewise, specimens bonded at a temperature below 600 °C did not bond well while specimens bonded near 660 °C (the melting temperature of Al), but not above, showed signs of melting.

- Maintaining the maximum pressure while the temperature of the system is decreasing after the appropriate amount of bonding time will ensure that the bond is well formed during the critical cooling time when the bond is hardening.

- The location of the grips during the tension test plays a key role in the outcome of the test. If the grips are too close to the Al/substrate interface, the bond may prematurely separate when the grips are closed and radial pressure is placed on the Al cylinders causing them to plastically deform. If the grips are a significant

distance away from the bond, the test may be measuring the combined strength of the Al cylinder and the interface, rather than solely the interface.

- A new strategy may be necessary to prevent bonding in the center of the interface. Some of the final specimens showed indications of contamination particularly near the graphite insert which lead to speculation that the slug was the root of the problem, even though the component had been thoroughly cleaned. The most dramatic deformation occurred at locations not adjacent to the insert. However, this could also have to do with the interface between the insert and the pure Al creating a stress concentration.

Some of the problems encountered in the interface tests could have possibly been avoided by using larger substrates with the same sized cylinders. This would allow the substrate to be centered inside the mold in a notch rather than an extrusion (or ledge) as long as the substrate is of a larger diameter than the graphite sleeves. The upper sleeve could be entirely thick walled (without a thin walled notch) to prevent any cracking and associated creep of the Al. Even if the Al did creep, it would simply flow into the notch and would not transfer the applied load to the mold. Furthermore, the outer unbonded portion of the substrate would allow the initial separation to occur without any inhibition from Al bonded to the side of the substrate. Using this configuration along with adherence to the aforementioned suggestions will most likely result in tests with more consistency and better numerical results. If this can be achieved, combined tension and torsion tests would allow for more direct comparisons with the simulations.

The infiltrated fiber preform investigations were intended to determine if this class of MMC's could produce similar benefits to aligned continuous fiber MMC's based on precipitate/interface interactions while maintaining a lower manufacturing cost. Unfortunately, the material did not live up to its potential. This is mainly due to cavitation occurring at the precipitates bonded to the fibers. Since the fibers are not aligned in the direction of loading they do not contribute to the work of fracture. Rather, the interactions of the cavities decrease the work of fracture and

contribute to the onset of critical fracture. The fibers slightly improved the strength and stiffness of the unreinforced material, but these came at a cost of increased embrittlement. Indeed, the infiltrated fiber preform shows much potential for greatly improving performance at high temperatures, but the fibers offer few benefits and some hindrances at ambient conditions.

Appendix A

Diffusion Bonding System Schematics and Manufacturing Drawings

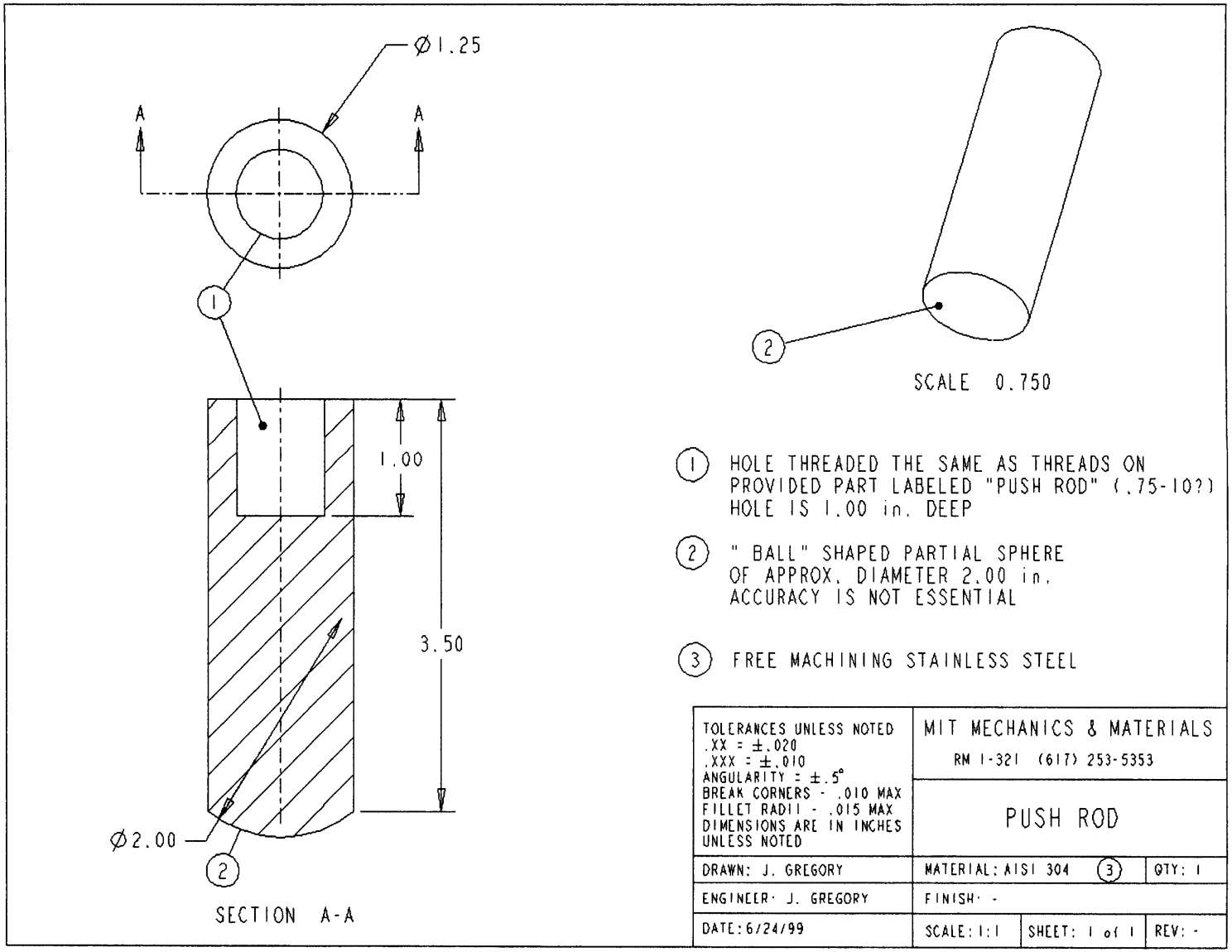

Figure A-1: Push Rod

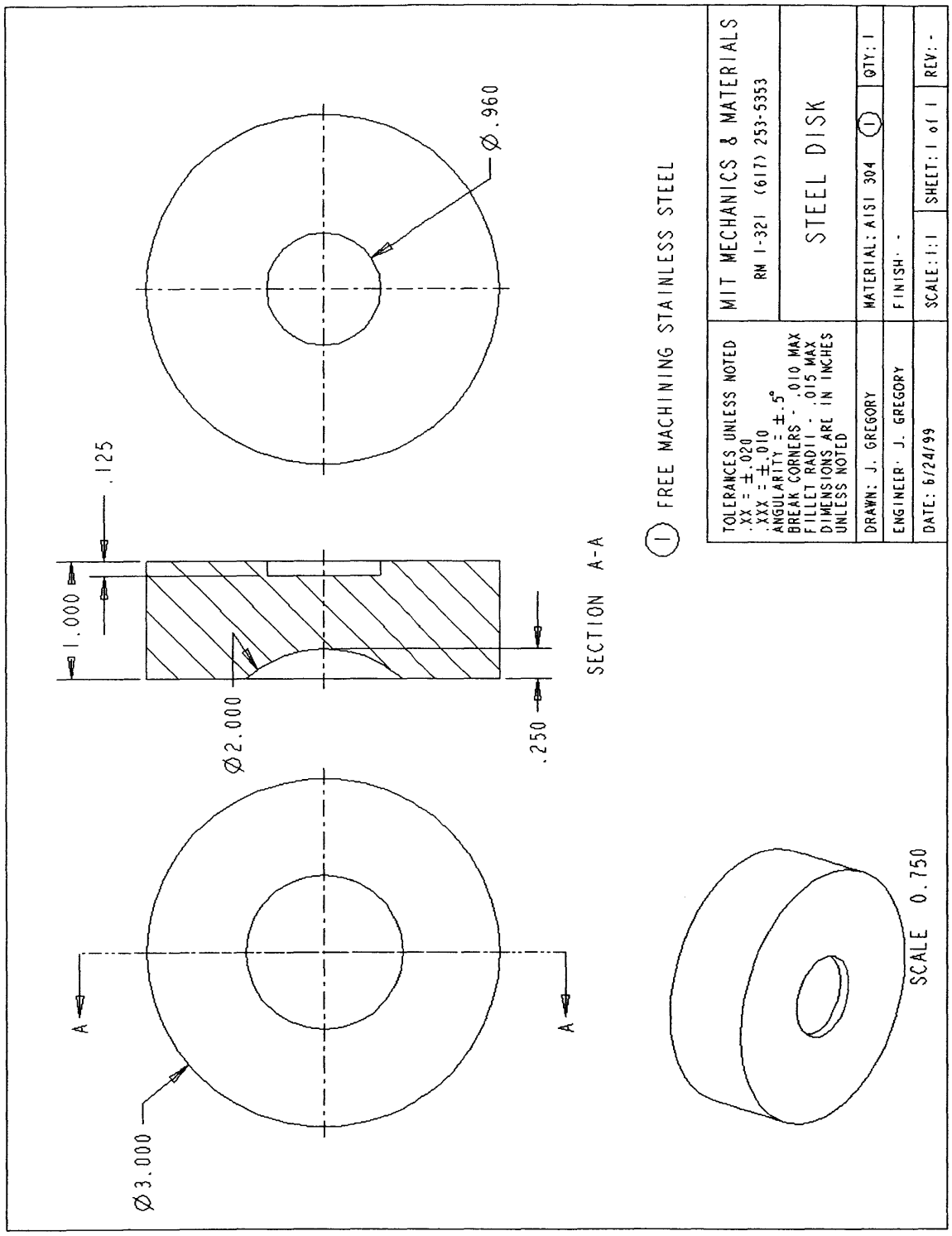

Figure A-2: Steel Disk

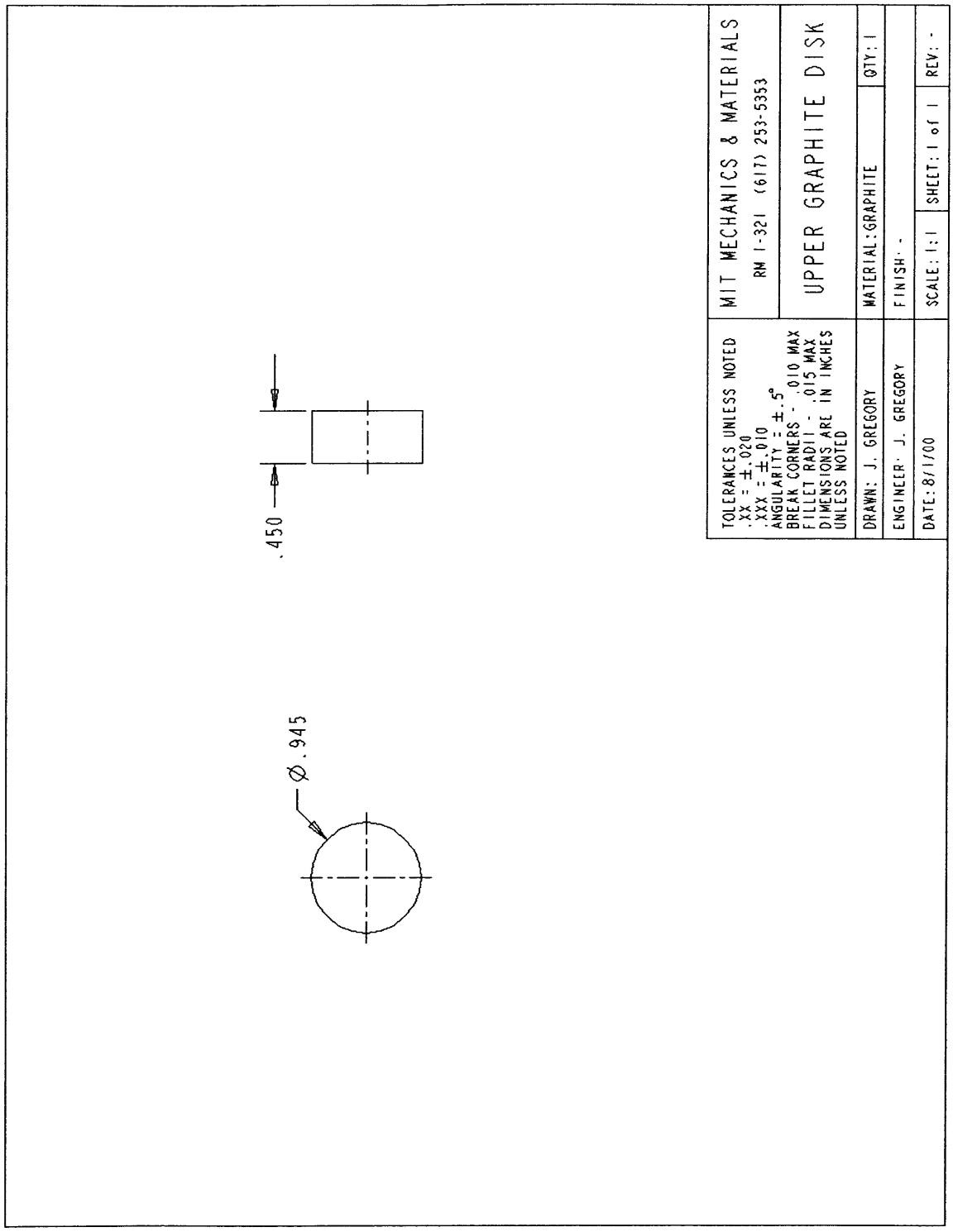

Figure A-3: Upper Graphite Disk

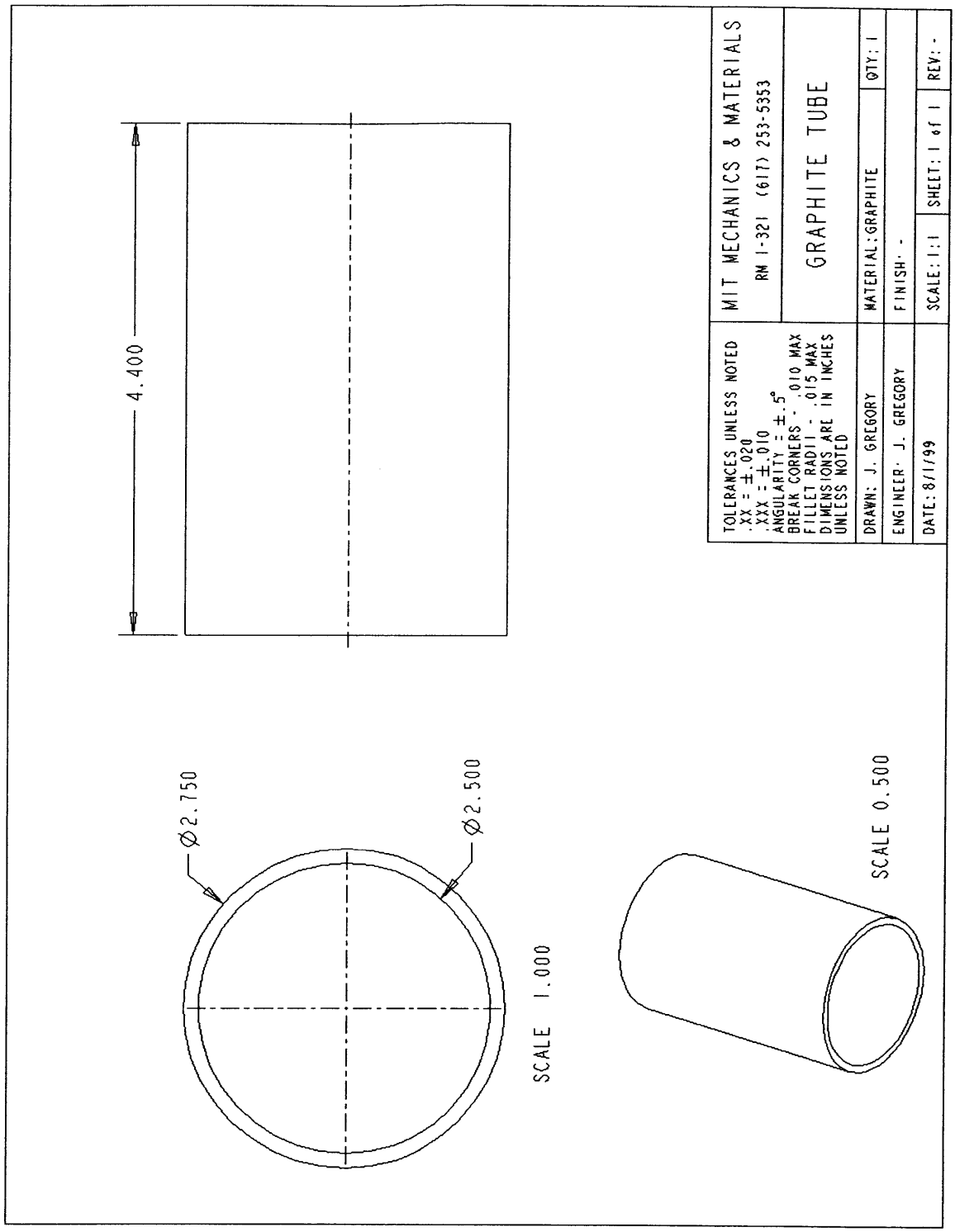

Figure A-4: Graphite Tube

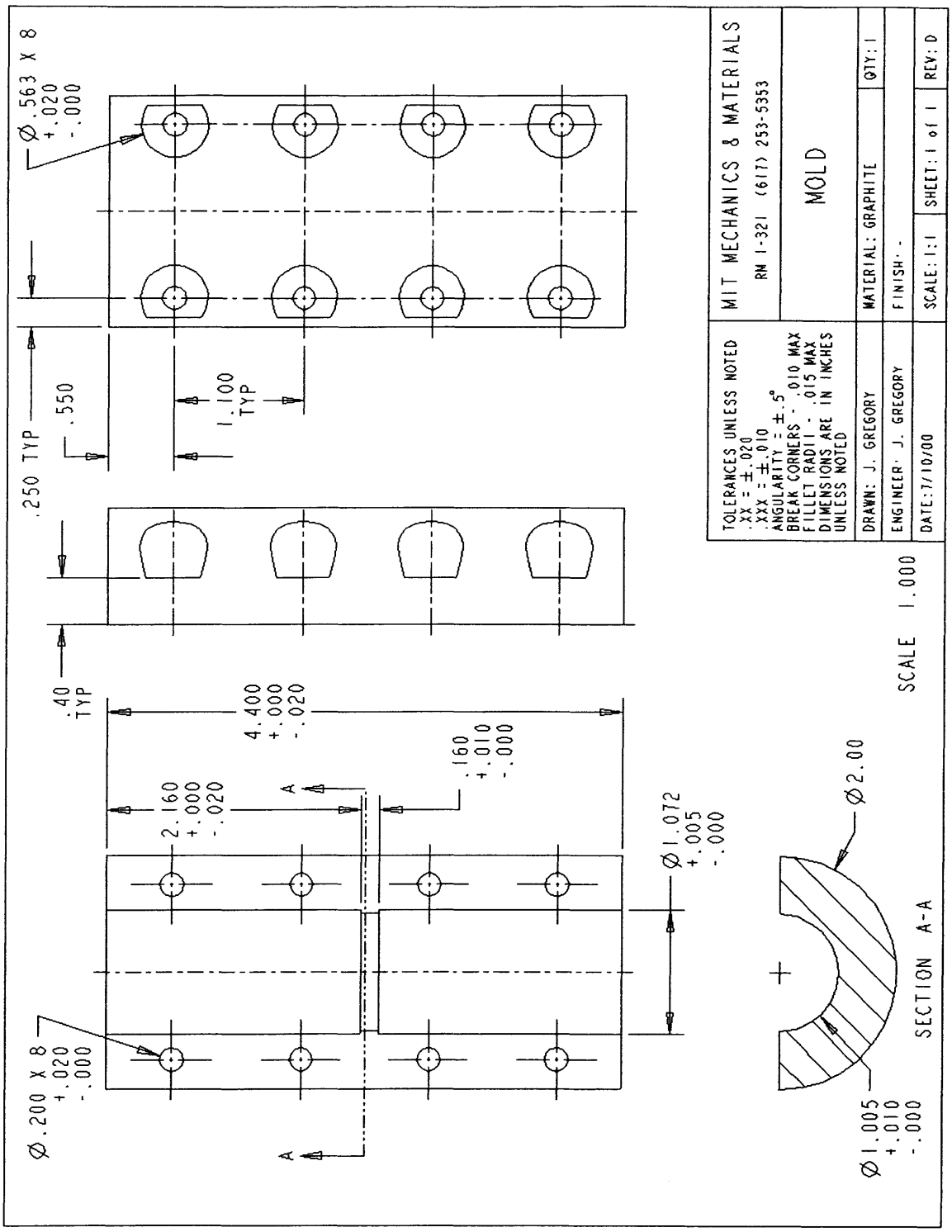

Figure A-5: Mold

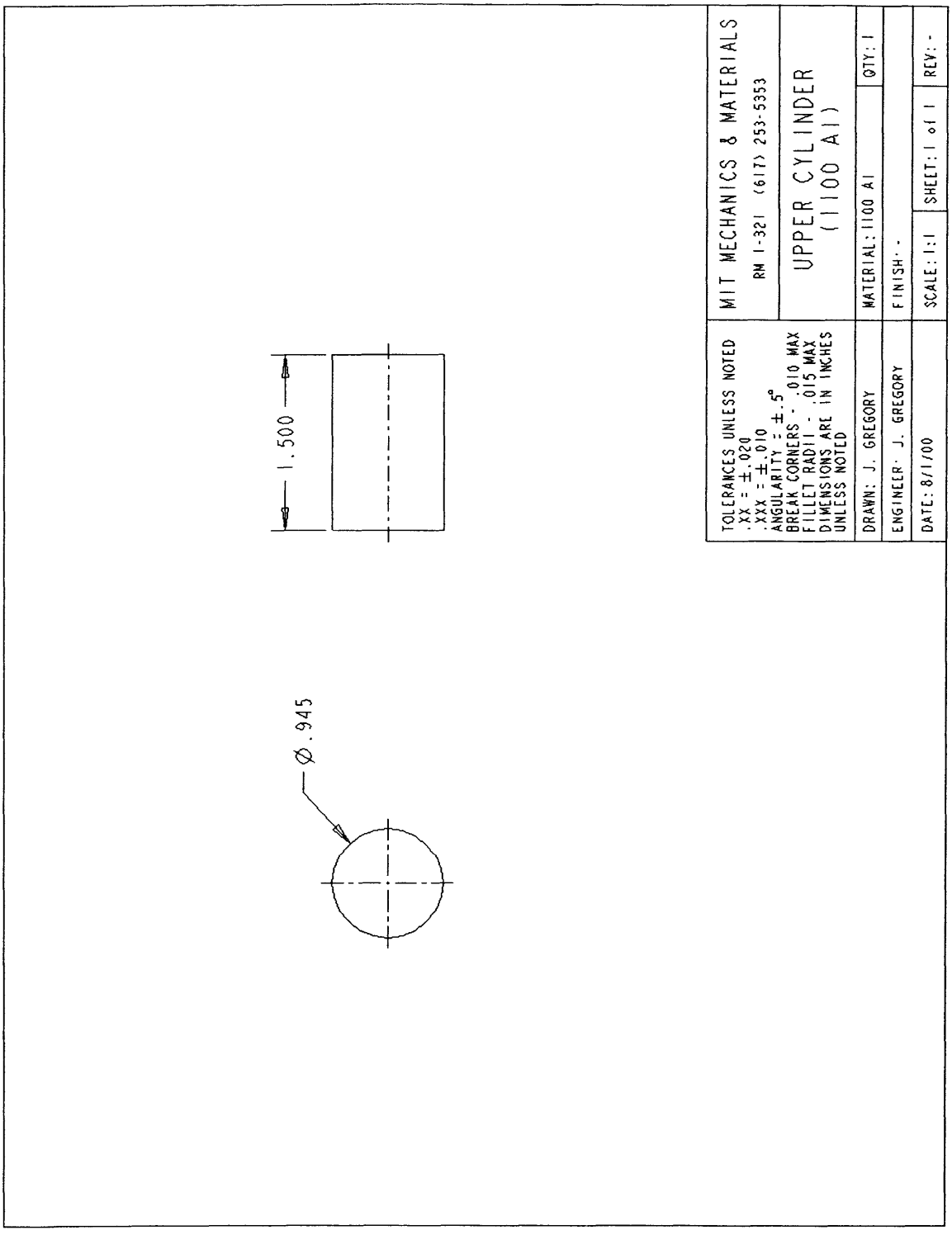

Figure A-6: Upper Cylinder (1100 Al)

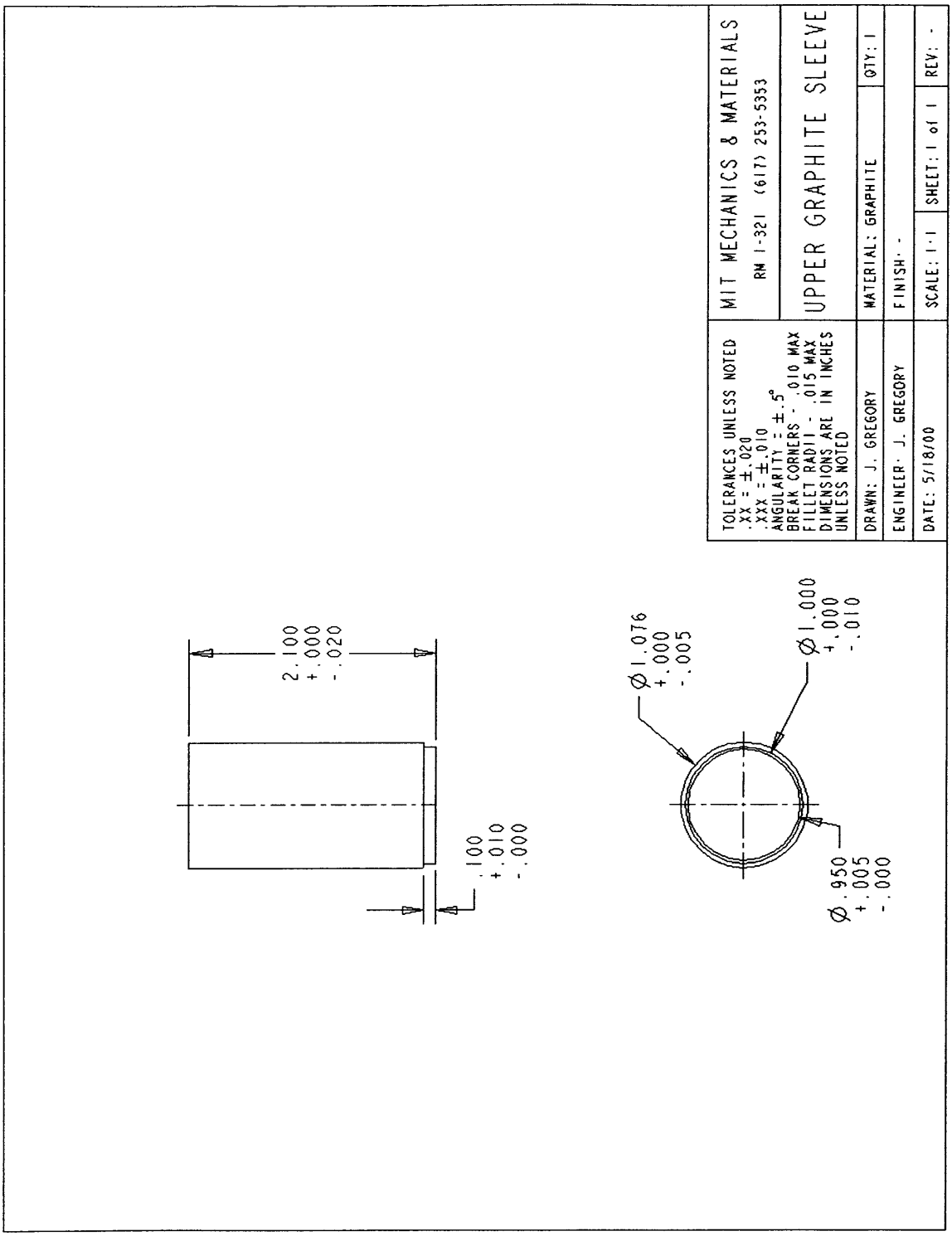

Figure A-7: Upper Graphite Sleeve

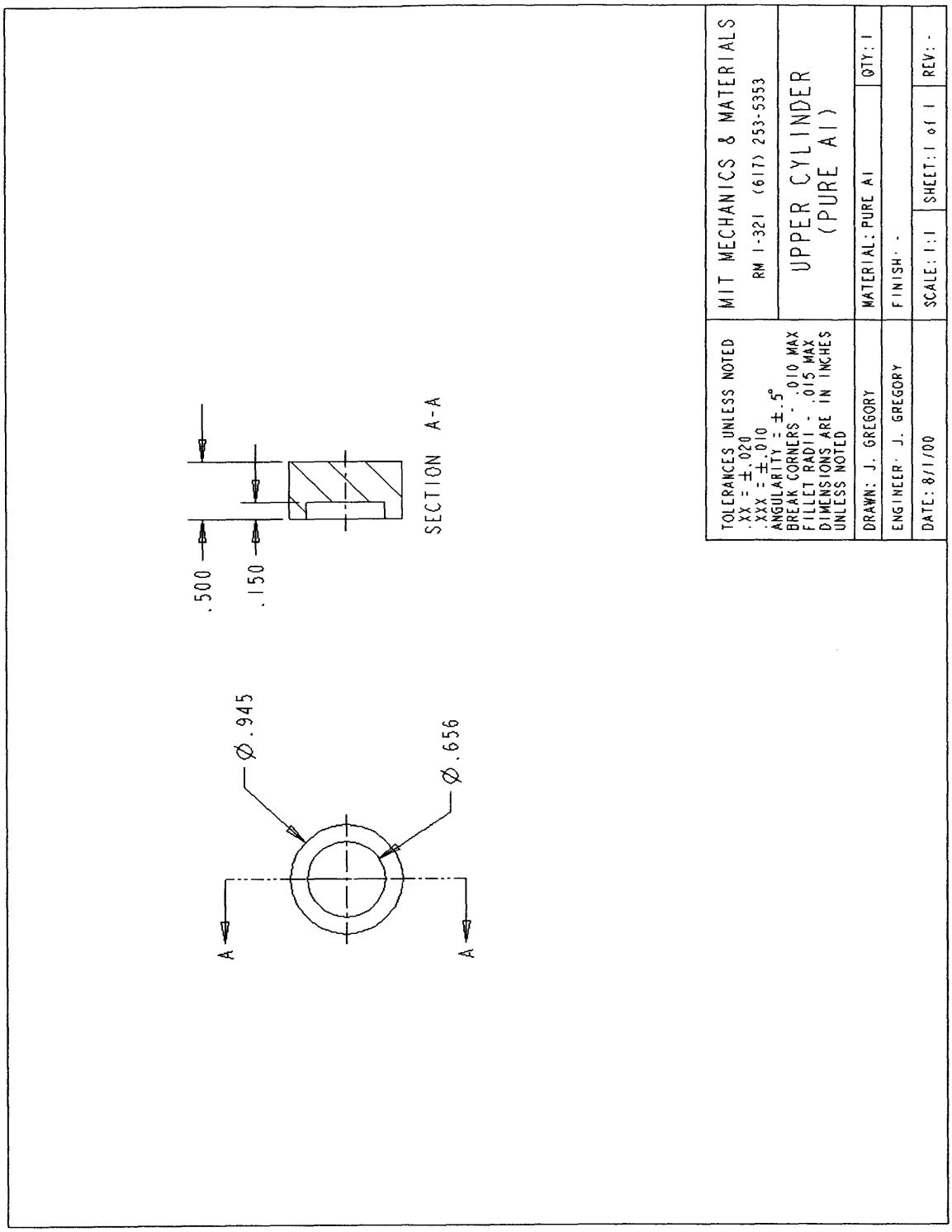

Figure A-8: Upper Cylinder (Pure Al)

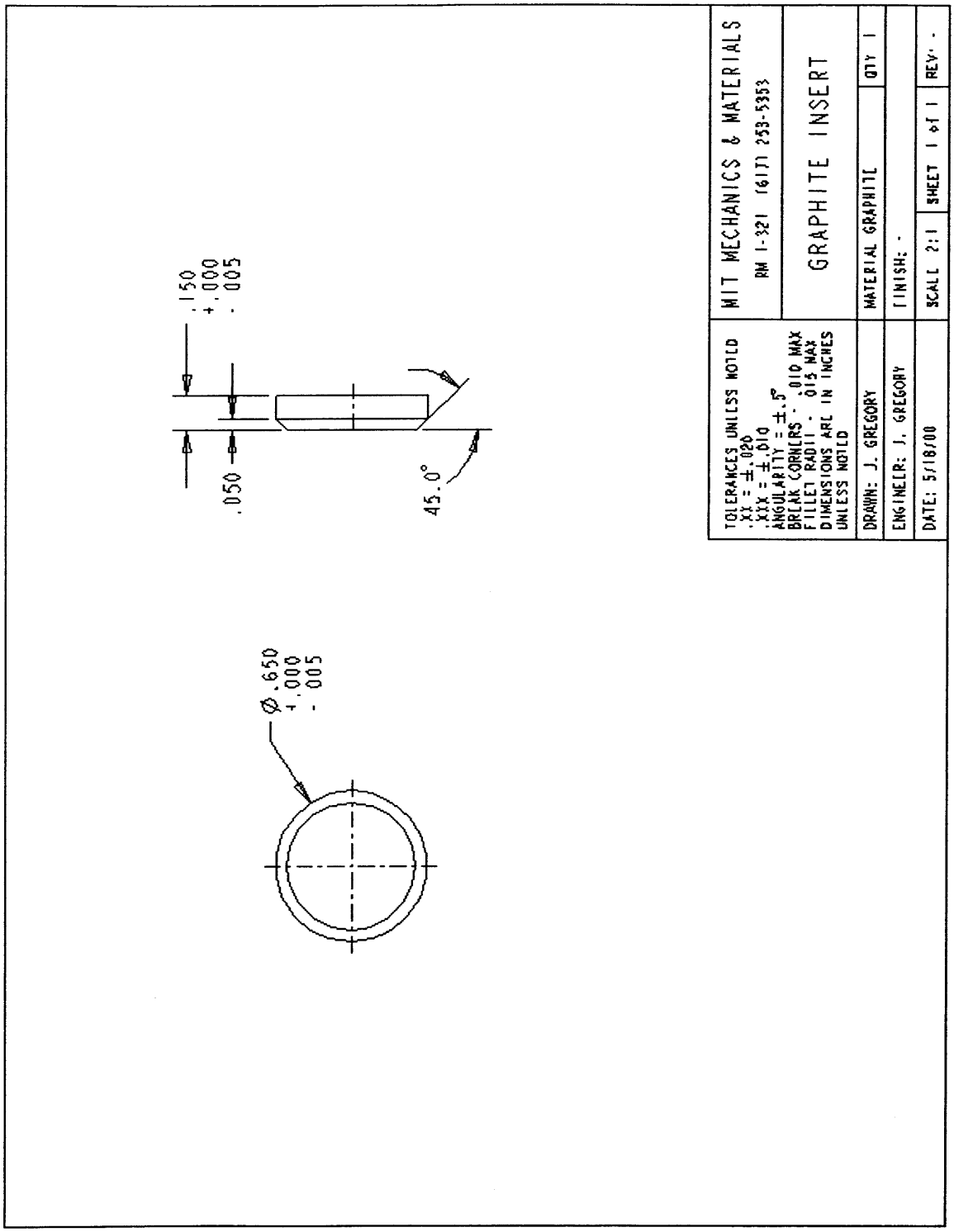

Figure A-9: Graphite Insert

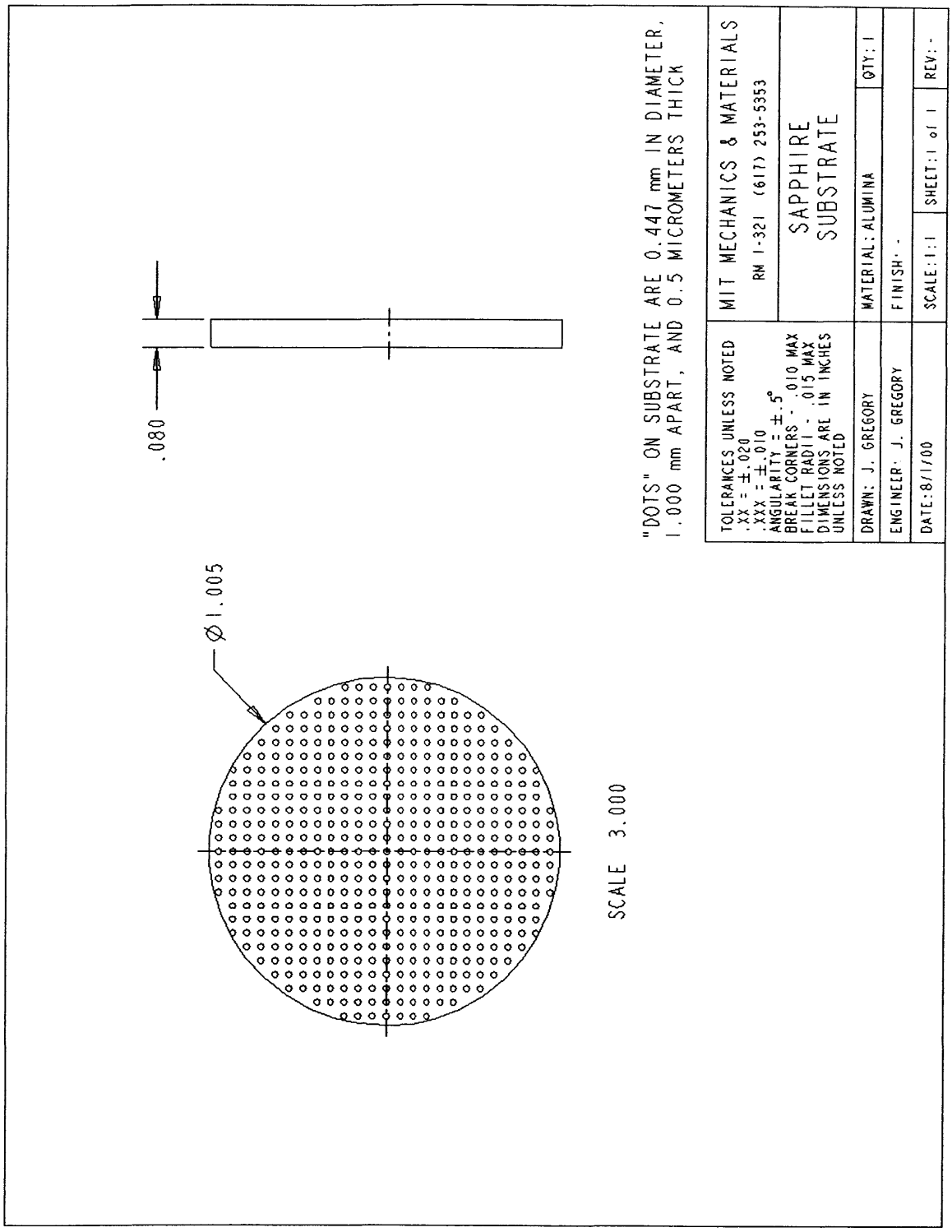

Figure A-10: Sapphire Substrate

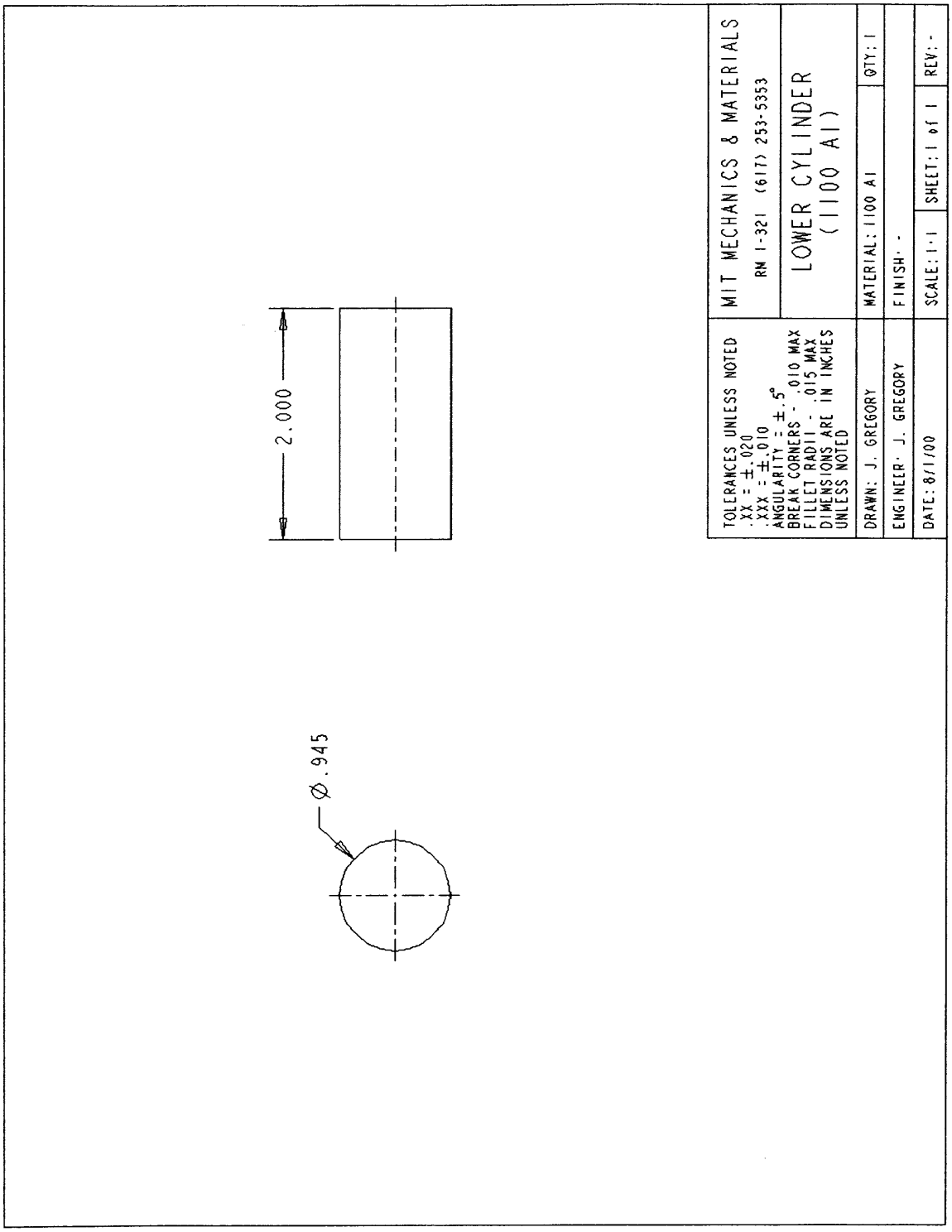

Figure A-11: Lower Cylinder (1100 Al)

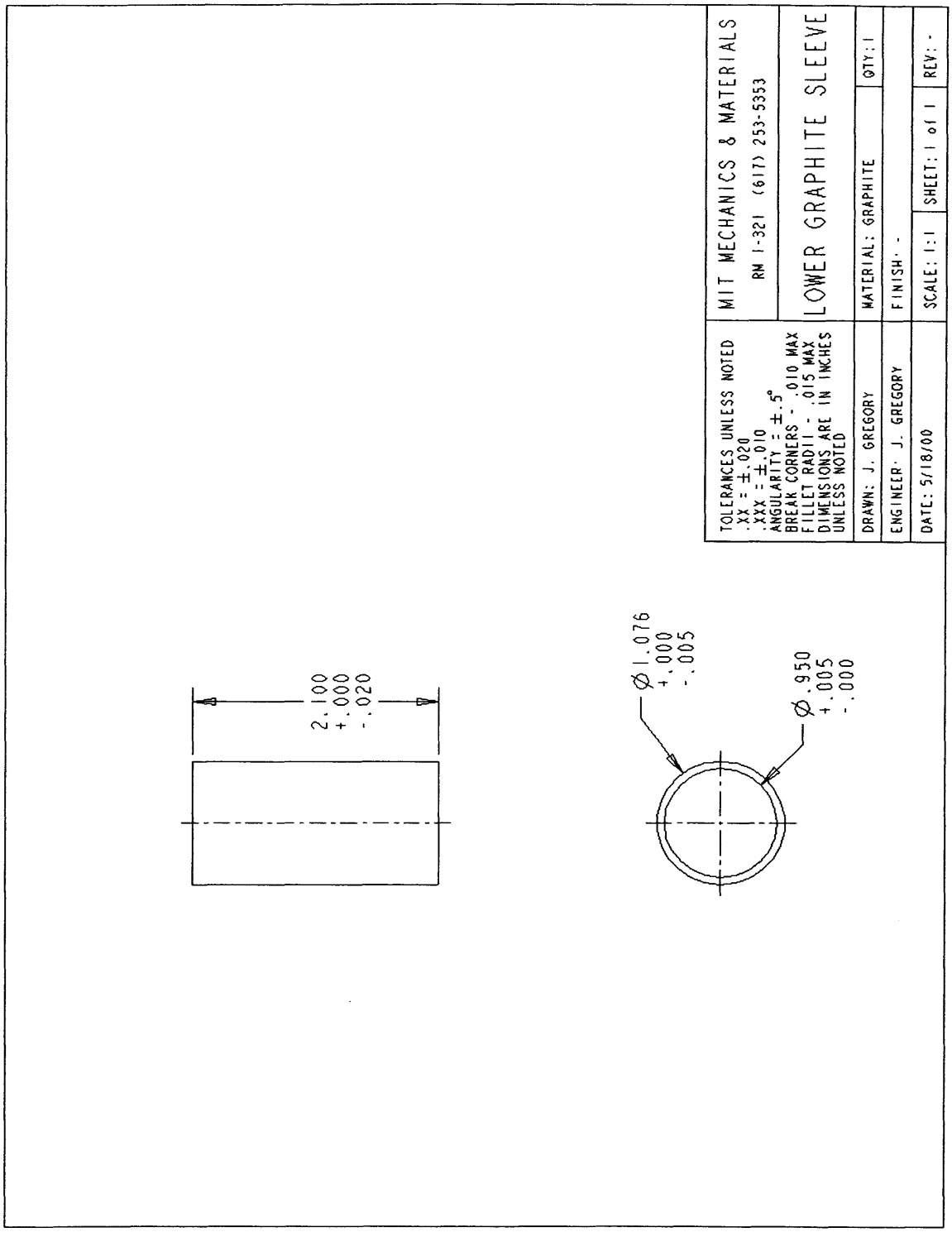

Figure A-12: Lower Graphite Sleeve

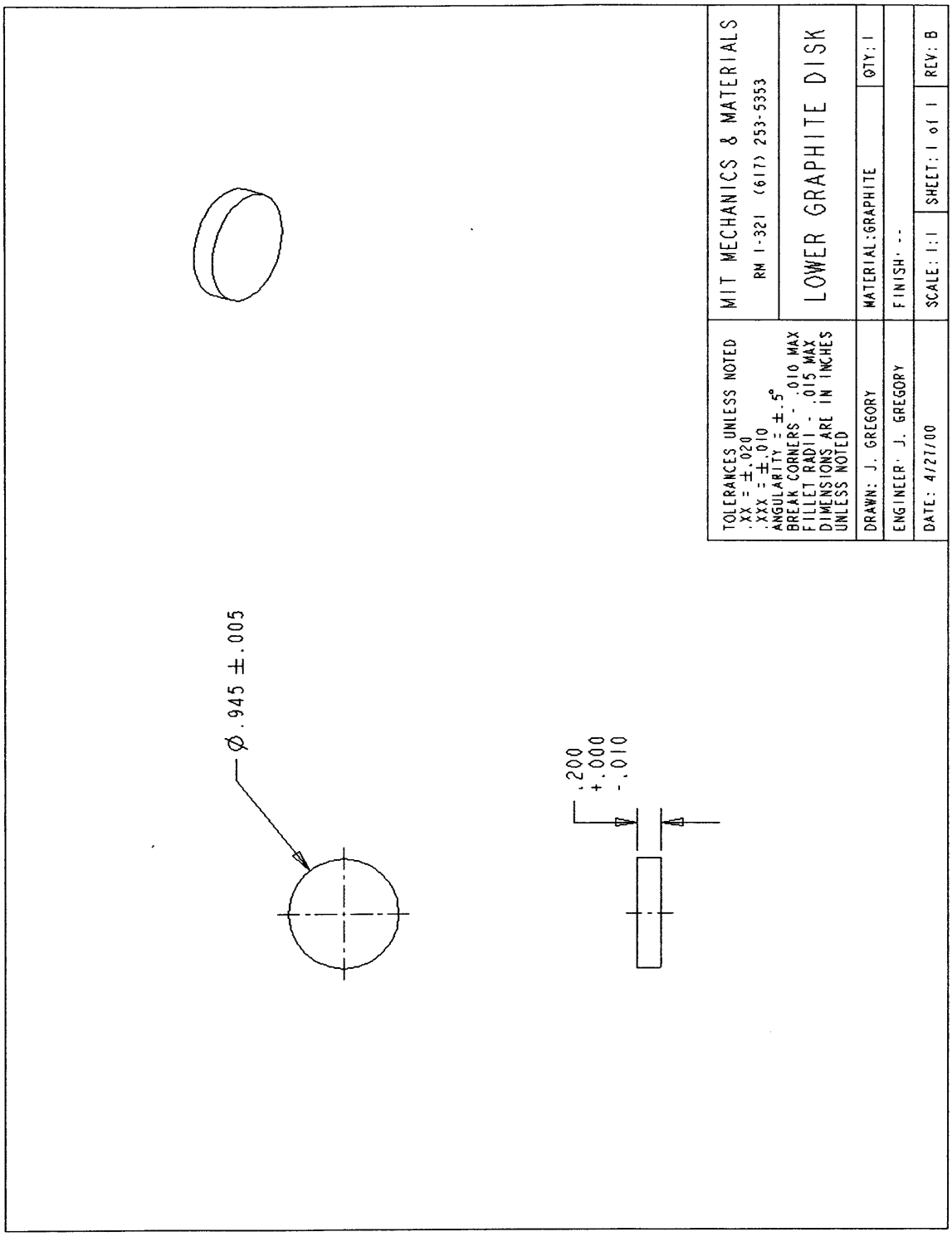

Figure A-13: Lower Graphite Disk

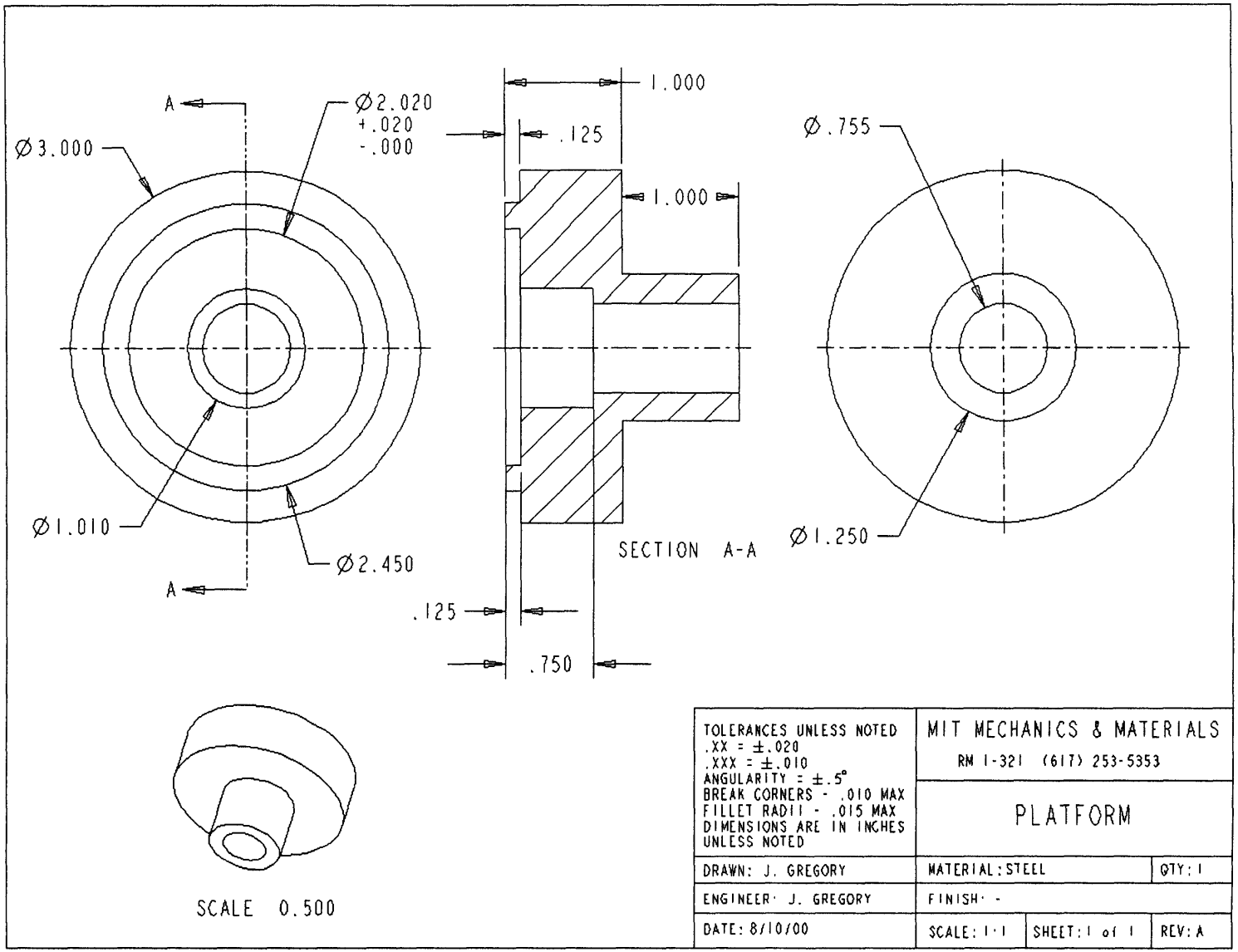

Figure A-14: Platform

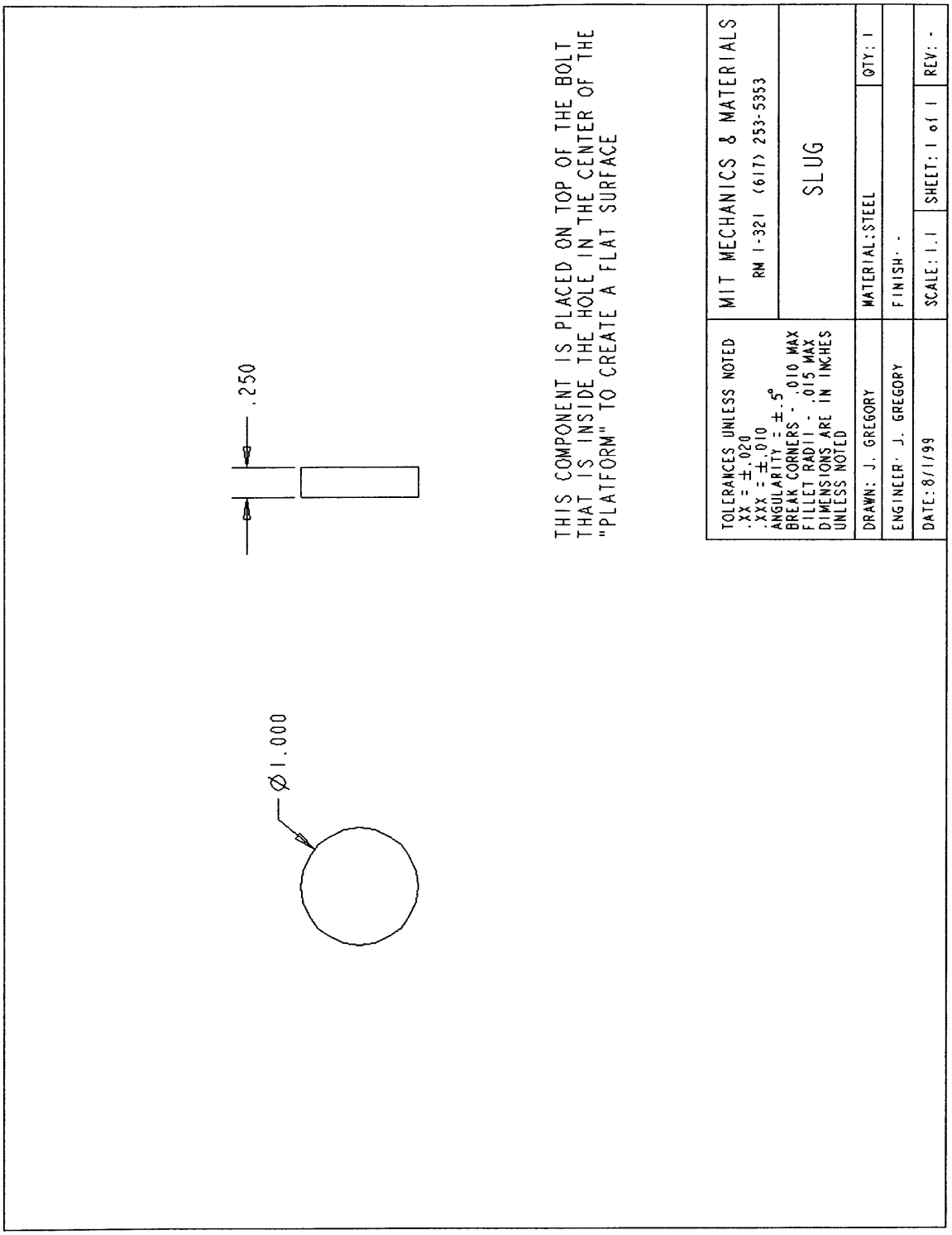

Figure A-15: Slug

Appendix B

Alternate Diffusion Bonded Specimen Fabrication Procedures

Several other alternate diffusion bonded specimen setups were tested prior to the configuration listed in Section 2.4.1 with varying degrees of success and failure. The initial bonding components consisted of two 1100 Al cylinders (entirely 1100 Al, upper and lower) with their radial surfaces anodized (*not* the flat bonding surfaces). The anodization was used in place of the graphite sleeves to prevent the cylinders from bonding to the mold. Graphite parting spray was applied to the mold and the cylinders' radial surfaces to further ensure that the cylinders would separate from the mold. The "dot pattern" on the substrate was a Cu deposition in an attempt to simulate the Al_2Cu precipitates that form in the actual composite. Finally, the bonding surfaces of the cylinders were cleaned with acetone immediately before bonding.

The problems with this configuration mainly centered on contamination of the interface. Ironically, even with the contamination some of the initial specimens contained a bond that could not be separated by the testing machine. The strength of the bond was such that it would not separate while the soft Al cylinders in the machine's collet grips slowly "slipped" because of the material's inability to resist a great deal of plastic deformation under the grip pressure. When the specimens were separated using a three point bend test, the discolored interfaces indicated that some sort of contamination was occurring during the bonding process. Furthermore,

the bonded surfaces did not show the desired separation in the regions between the "dots", specifically the necking of the aluminum.

Attempts to remedy these difficulties began by reducing the effective bonding area by half. This was accomplished by creating an anodized conical indentation on the aluminum bonding surface (sized to be half the area of the surface with a 2° angle) to ensure that adherence with the substrate would not occur in this area. In addition, some of the substrates contained a large "dot" of Cu, the same diameter as the anodized cone in the Al, in the center of the disk to further create weak adherence in this portion of the interface. The cleanliness of the interface was addressed by machining the bonding surfaces of the cylinders which may have been incidentally oxidized during the anodization process (even though they were covered and protected from the process). Angled tapers were also added at the edges of the bonding surfaces (upper and lower cylinders) in an attempt to ensure that the interfaces would properly bake out any remaining impurities from the inside of the surface outward before bonding (any taper of the surface flattened out during the bonding process).

Even though the quality of the bonds improved with the implementation of these measures, there still appeared to be contamination at the interfaces which was causing the bonds to separate at low loads with almost no plastic deformation of the aluminum at the bond (indicating poor adherence). The main source of the contamination appeared to be the anodization layer on the cylinders, particularly in the conical indentation at the interface. In addition, the tapered surfaces were causing the loading to be unstable and nonuniform during bonding. To combat these problems the cylinders were baked (in air) at 250 °C for six hours to try to remove any impurities that may be locked in the surface. Furthermore, the conical indentation was no longer anodized but was instead exposed to the air in the baking process so that an oxidized layer would develop that would inhibit adherence to the substrate in the area, but would not contain the impurities of the anodized layer. After the oxidation of the conical section was complete, the flat bonding surface was machined to remove the oxidized layer that developed during the baking. These specimens were then cleaned in accordance with the intensive procedure described in Section 2.4.1

and baked in a vacuum.

These modifications to the setup were still producing specimens with contaminated interfaces and weak bonds. Thus, some drastic changes were made to try to eliminate impurities at the interface while creating a specimen that would embody the desired behavior. The modifications to the setup were meant to maintain the benefits of the anodized surfaces (i.e. no bonding to the graphite) while eliminating what appeared to be the major source of the contamination. This led to the configuration described in Section 2.4.1. The graphite sleeves ensured the cylinders (which were no longer anodized) would not adhere to the mold and the graphite insert at the bonding surface did not produce nearly the same amount of contamination as any other of the previous alternatives. Furthermore, Fe was used on the substrate because of fears that the Cu may have been consumed by the Al during bonding. Finally, the pure Al at the interface produced much better evidence of plastic deformation during the separation than the 1100 Al. This specimen composition produced the best results out of any of the previously tested alternatives, but there are still some improvements that could be made to create the "ideal" specimen which were discussed in Section 2.5 and Chapter 4.

Appendix C

Infiltrated Fiber Preform Individual Tension Test Results

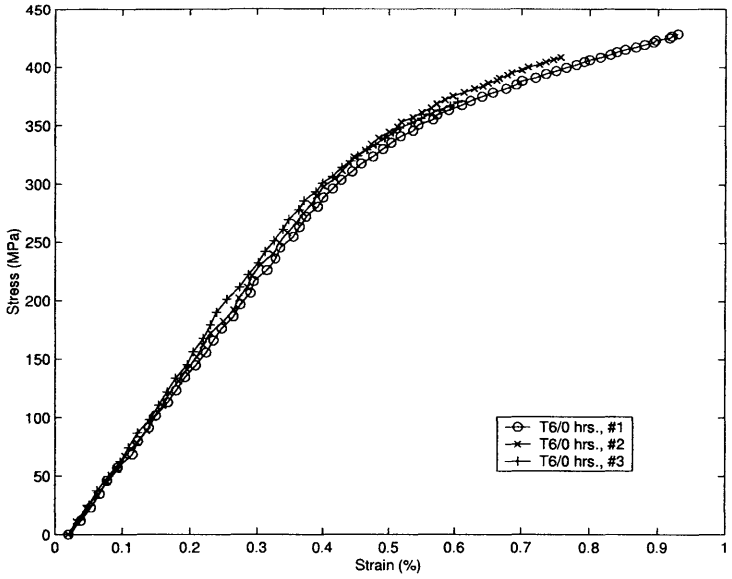

Figure C-1: Infiltrated fiber preform individual tension test results - T6/0 hours.

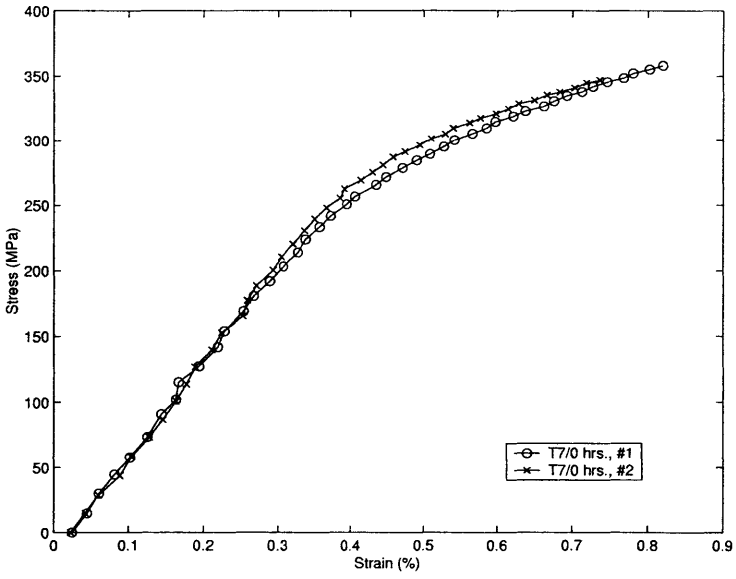

Figure C-2: Infiltrated fiber preform individual tension test results - T7/0 hours.

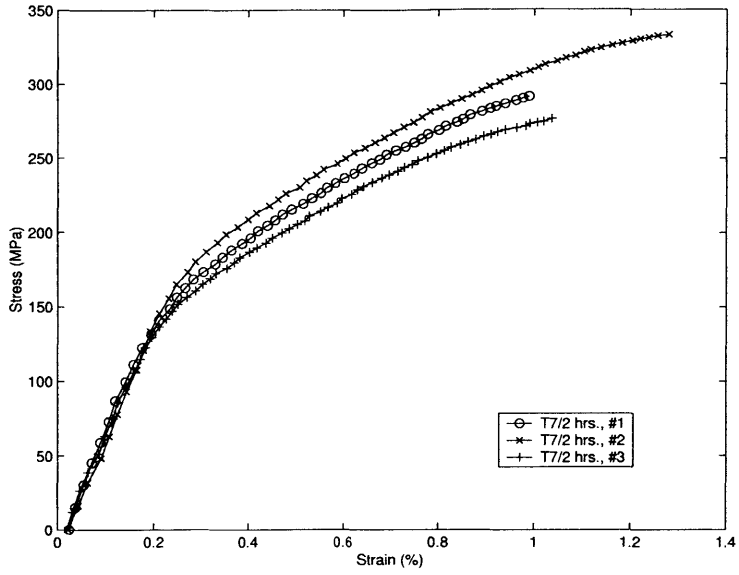

Figure C-3: Infiltrated fiber preform individual tension test results - T7/2 hours.

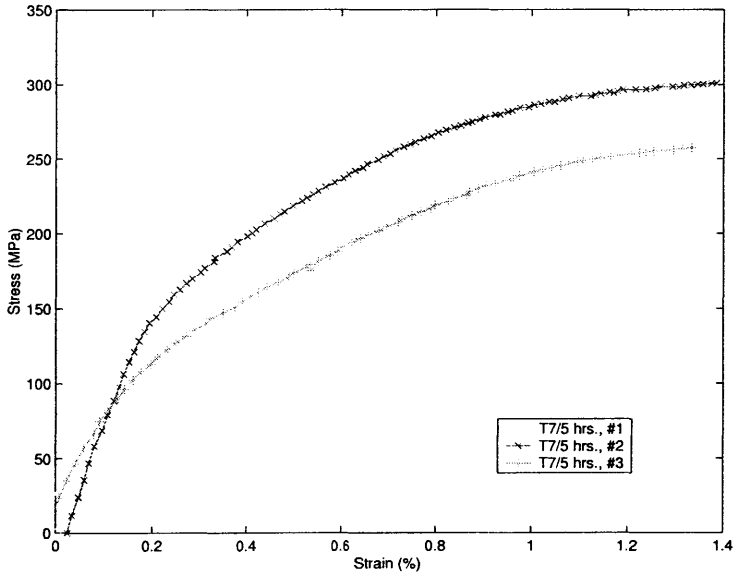

Figure C-4: Infiltrated fiber preform individual tension test results - T7/5 hours.

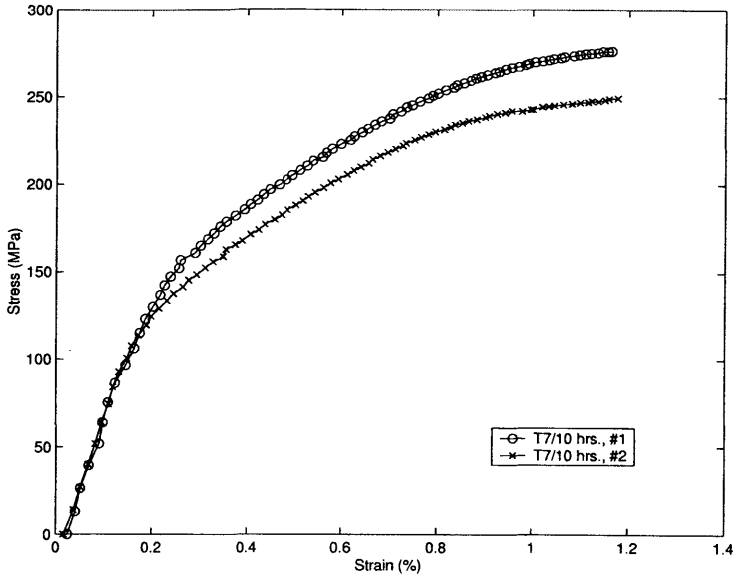

Figure C-5: Infiltrated fiber preform individual tension test results - T7/10 hours.

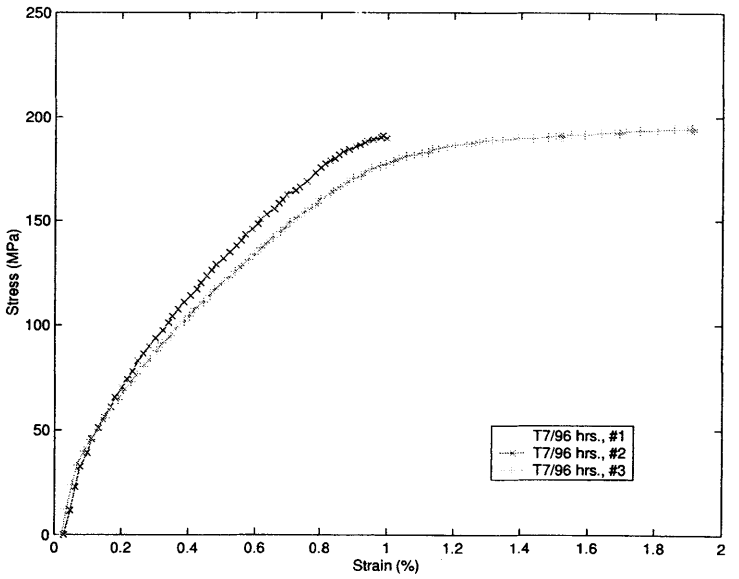

Figure C-6: Infiltrated fiber preform individual tension test results - T7/96 hours.

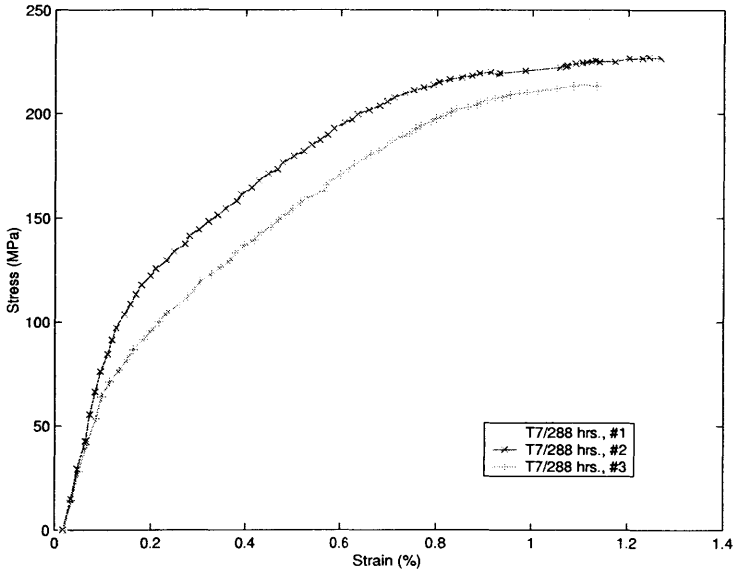

Figure C-7: Infiltrated fiber preform individual tension test results - T7/288 hours.

Appendix D

Infiltrated Fiber Preform Volumetric Strain Tests Supporting Data

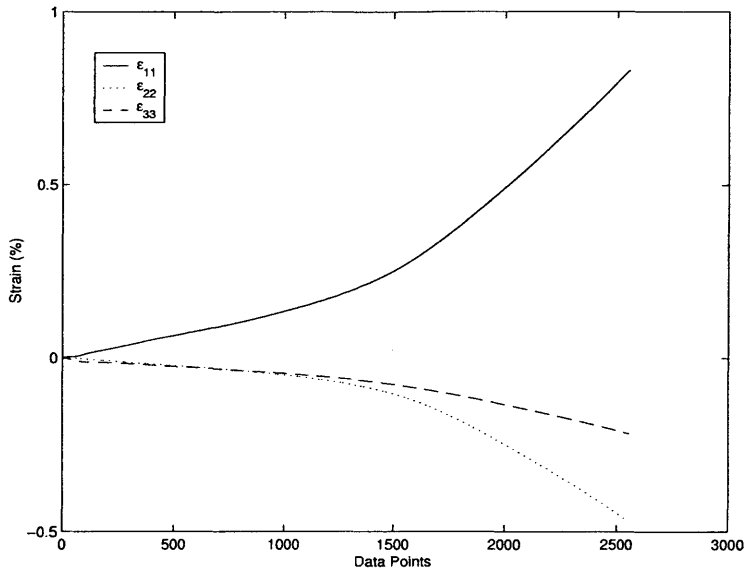

Figure D-1: Infiltrated fiber preform volumetric strain test - individual strain results, T7/0 hours.

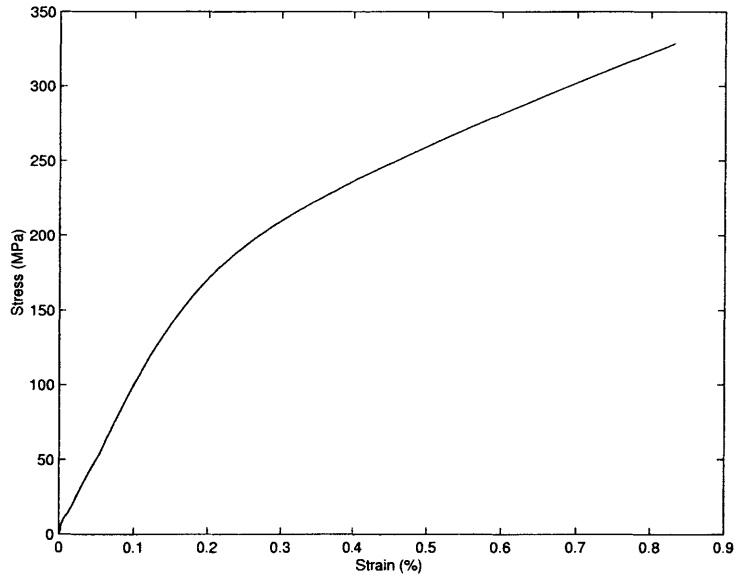

Figure D-2: Infiltrated fiber preform volumetric strain test - stress vs. strain, T7/0 hours.

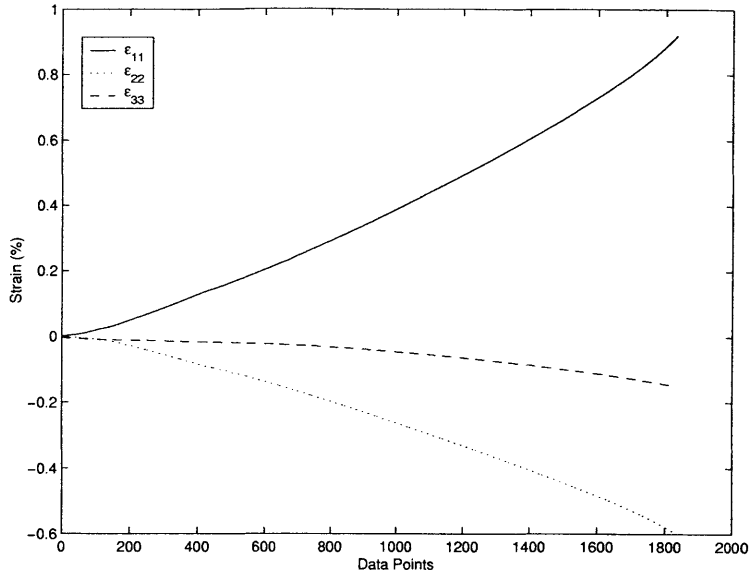

Figure D-3: Infiltrated fiber preform volumetric strain test - individual strain results, T7/100 hours.

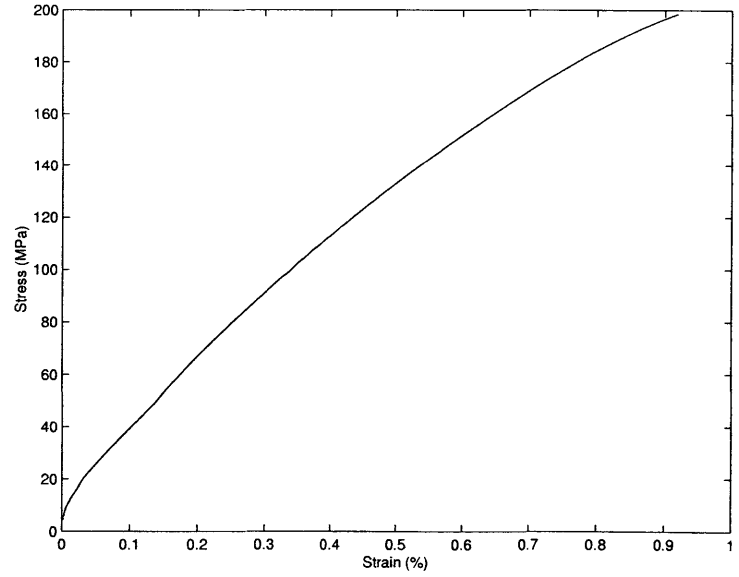

Figure D-4: Infiltrated fiber preform volumetric strain test - stress vs. strain, T7/100 hours.

Appendix E

Unreinforced Alloy Individual Tension Test Results

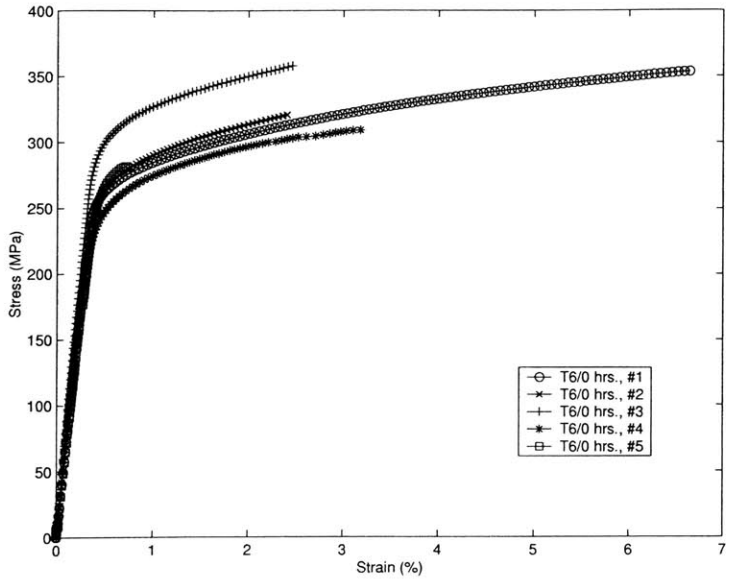

Figure E-1: Unreinforced alloy individual tension test results - T6/0 hours.

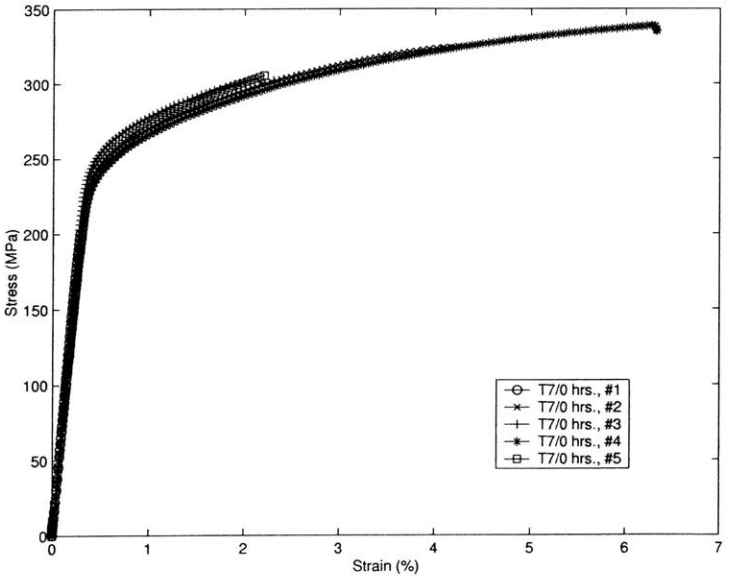

Figure E-2: Unreinforced alloy individual tension test results - T7/0 hours.

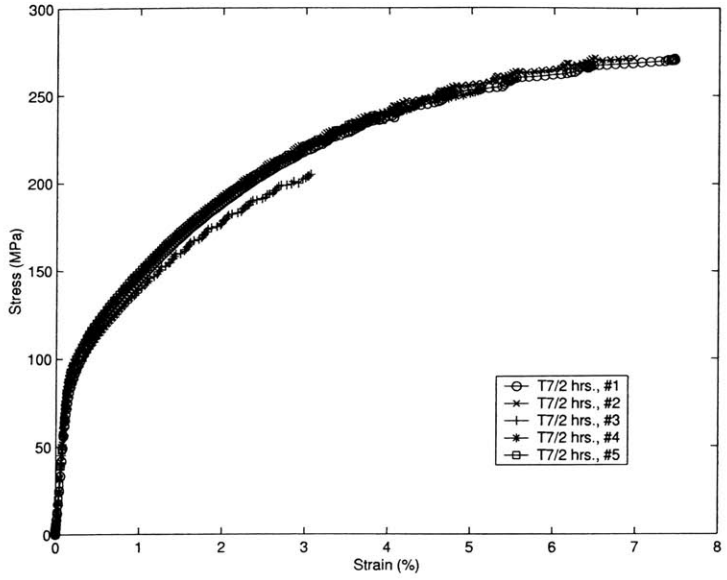

Figure E-3: Unreinforced alloy individual tension test results - T7/2 hours.

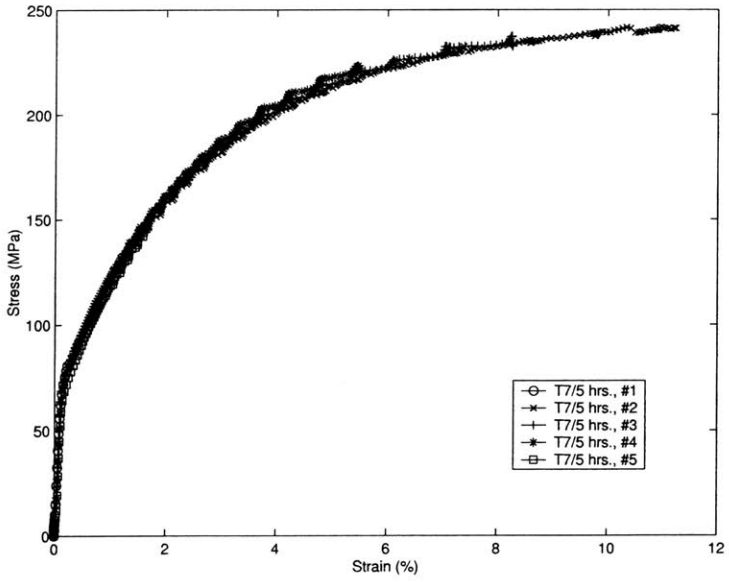

Figure E-4: Unreinforced alloy individual tension test results - T7/5 hours.

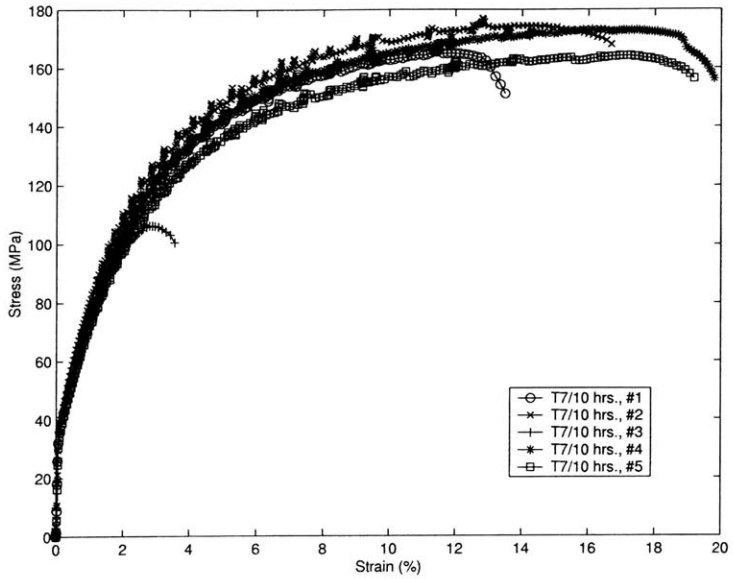

Figure E-5: Unreinforced alloy individual tension test results - T7/10 hours.

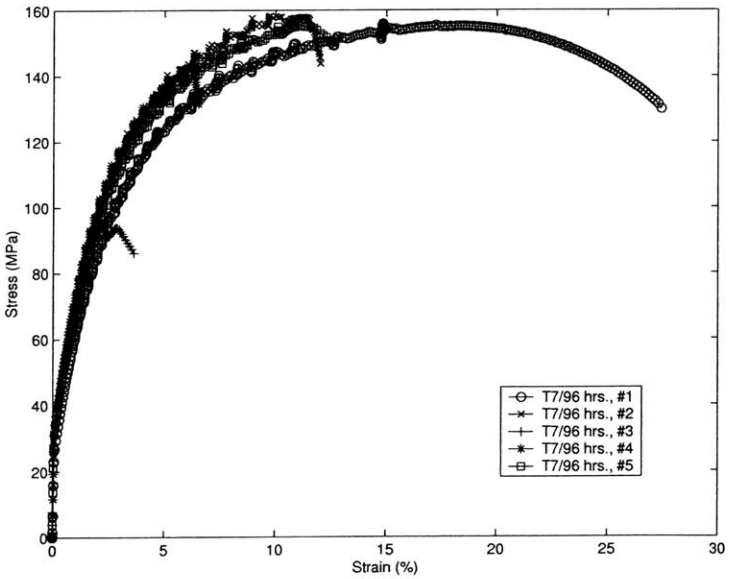

Figure E-6: Unreinforced alloy individual tension test results - T7/96 hours.

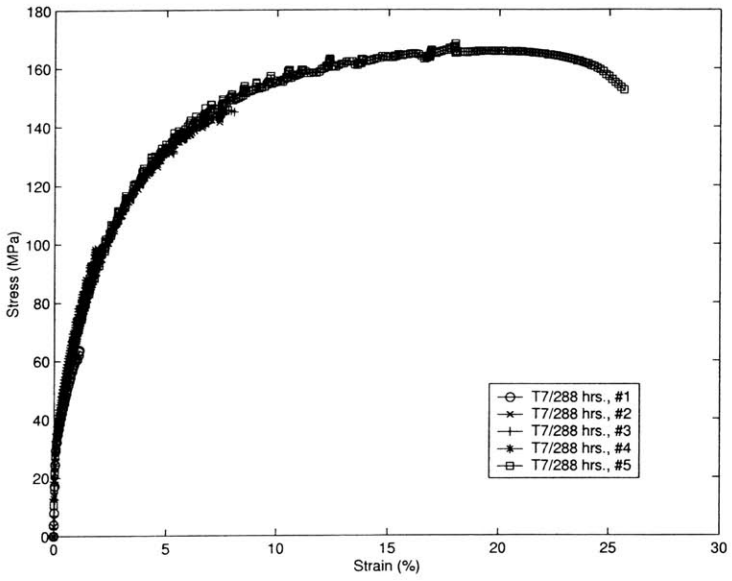

Figure E-7: Unreinforced alloy individual tension test results - T7/288 hours.

Bibliography

[1] A.S. Argon, M.L. Seleznev, C.F. Shih, and X.H. Liu. Role of controlled debonding along fiber/matrix interfaces in the strength and toughness of metal matrix composites. *International Journal of Fracture*, 93:351–371, 1998.

[2] I. Roman and P.D. Jero. Interfacial shear behavior of two titanium-based scs-6 model composites. In *Materials Research Society Symposium Proceedings*, volume 273, pages 337–342. Materials Research Society, 1992.

[3] R.J. Kerans, P.D. Jero, T.A. Parthasarathy, and A. Chatterjee. Determination of fiber/matrix interface mechanical properties in brittle-matrix composites. In *Materials Research Society Symposium Proceedings*, volume 194, pages 263–270. Materials Research Society, 1990.

[4] L.J. Ebert and P.K. Wright. *Interfaces in Metal Matrix Composites*, volume 1 of *Composite Materials*, chapter 2, pages 57–63. Academic Press, New York, NY, 1974.

[5] M.L. Seleznev, J.A. Cornie, and F.A. Armatis, Jr. Improving mechanical properties of Nextel 610-reinforced Al-224 alloy through θ phase precipitation at the fiber/matrix interface: Kinetics of the precipitation process. *Journal of Materials Engineering and Performance*, 2(3):347–352, June 1993.

[6] V. Nagpal, F.A. McClintock, C.A. Berg, and M. Subudhi. Traction-displacement boundary conditions for plastic fracture by hole growth. *Foundations of Plasticity*, pages 365–385, 1973.

[7] A. Needleman. A continuum model for void nucleation and inclusion debonding. *Journal of Applied Mechanics*, 54:523–531, 1987.

[8] V. Tvergaard and J.W. Hutchinson. The influence of plasticity on mixed-mode interface toughness. *Journal of Mechanical and Physical of Solids*, 41:1119–1135, 1993.

[9] M.L. Seleznev, A.S. Argon, I.L. Seleznev, J.A. Cornie, and R.P. Mason. Effect of composition, particle size and heat treatment on the mechanical properties of Al-4.5wt.% Cu based alumina particulate reinforced composites. In *SAE International Congress and Exposition.* Society of Automotive Engineers, February 1998.

[10] A.B. Pandey, B.S. Majumdar, and D.B. Miracle. Deformation and fracture of a particle-reinforced aluminum alloy composite. *Metallurgical Transactions*, 1999.

[11] A.S. Argon. *Statistical Aspects of Fracture in Composite Materials: Fracture and Fatigue*, volume 5, pages 153–190. Academic Press, New York, 1974.

[12] J.B. Friler, A.S. Argon, and J.A. Cornie. Strength and toughness of carbon fiber reinforced aluminum matrix composites. *Material Science Engineering*, A162:143–152, 1993.

[13] X.H. Liu. *Plastic Kinking in Polymer Matrix Composites and Interface Debonding in Metal-Matrix Composites.* PhD thesis, Brown University, Providence, RI, 1998.

[14] V. Kumar, M.D. German, and C.F. Shih. An engineering approach for elastic-plastic fracture analysis. Technical Report NP-1931, General Electric Company, Corporate Research and Development, July 1981.